Michele BIANCHI JANETTI

Hygrothermal Analysis of Building Components Inclosing Air Cavities: Comparison between Different Modeling Approaches and Experimental Results

DISSERTATION

eingereicht an der

LEOPOLD-FRANZENS-UNIVERSITÄT INNSBRUCK

FAKULTÄT FÜR TECHNISCHE WISSENSCHAFTEN
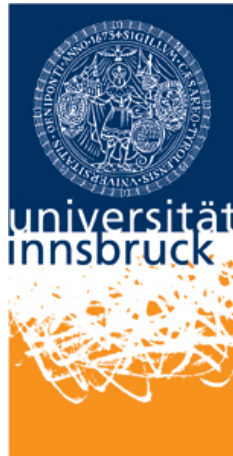
zur Erlangung des akademischen Grades

DOKTOR DER TECHNISCHEN WISSENSCHAFTEN

Innsbruck, Oktober 2015

Acknowledgments

I would like to express my gratitude to my supervisor Wolfgang Feist for his scientific support during this work, and for showing me that building physics is not just a 'profession', but can also be a way to answer human needs.

I´m very grateful to Luigi P. M. Colombo, who generously agreed to review this work and contributed to its improvement with very careful feedback and remarks.

One great thank you to Rainier Pfluger, for the many new ideas he gave to me in order to improve the quality of this work, and for introducing me to the Tanzhaus Tirol.
I would like to sincerely thank Fabian Ochs, for the trust and the friendly support he gave me during this time. My arrival in Innsbruck is also due to him.

Andreas Saxer is gratefully acknowledged for his help and for his advice concerning the experimental part of this work.

Thank to Edward Lowes for improving the language quality of some parts of this thesis.
Without the support and the engagement of Lorenzo Nespoli, Renato Passaniti, Tecla Carrubba and Dominik Granig this work would have never come to an end. Their collaboration has been much appreciated.

Part of this work has been funded by the European project "3ENCULT" (efficient energy for EU cultural heritage) within the 7th framework program and by the Project "IPAD" (FFG). This financial support is gratefully acknowledged.

I would like to thank all colleagues and friends at the "Unit for Energy Efficient Buildings", in particular Matthias Werner, Georgios Dermentzis, Kai Längle and Pavel Sevela, who have shared an office with me during this time - thanks for the good times together and for all your help during this work.
Thanks to all friends at the Passivhaus Institute, in particular to Oliver Ottinger, who gave me precious advice on improving the quality of this work, and to the family of Harald Malzer.

Sincere gratitute also to all the other friends and to my family that have accompanied me during this time.

Kurzfassung

In den letzten Jahren wurde die Verbesserung der Energieeffizienz von Gebäuden eine prioritäre Zielsetzung für die europäische Energiepolitik.

Diese Zielsetzung spielt eine wichtige Rolle in den sogenannten "20-20-20-Zielen" (20 % Reduktion der Emission von Treibhausgasen, Steigerung der Produktion erneuerbarer Energien bis 20 % und einer Verbesserung der Gesamtenergieeffizienz um 20 %).

Eine große Herausforderung liegt nicht nur im Neubau, sondern auch in der Sanierung von bestehenden Objekten, die in Zukunft einen höheren Energieeffizienz-Standard erreichen müssen. Bezogen auf die Gebäudehülle ist vor allem richtige Planung und der Einsatz geeigneter Materialien entscheidend, um eine hohe Qualität und bauschadensfreie Konstruktionen gewährleisten zu können.

Während Standardlösungen (z.B. außengedämmte Wände) bauphysikalisch als weitgehend unproblematisch betrachtet werden können, stellt insbesondere die Planung und Ausführung von Innendämmsystemen noch eine Herausforderung dar. Diese Problemstellung ist die Hauptmotivation dieser Arbeit.

Bei innenseitiger Wärmedämmung können nur dann kritische Feuchtigkeitszustände ausgeschlossen werden, wenn eine sorgfältige Planung vorab durchgeführt worden ist.

Langfristig kann Dampfdiffusion aus dem Inneren des Gebäudes zu hoher Feuchtigkeit hinter der Dämmung führen, was unter Umständen einer Schädigung organischer Stoffe (z.B. Holzbalken) mit sich zieht. Die Voraussetzung für eine korrekte Planung eines Dämmsystems ist ein fundiertes Wissen der Wärme- und Feuchtetransportmechanismen in den eingesetzten Materialien und Systemen (Schichtaufbauten und Anschlussdetails).

Zu diesem Thema wurden bereits zahlreiche numerische und experimentelle Studien publiziert; Ziel dieser Arbeit ist es, den Stand der Wissenschaft und Forschung auf diesem Gebiet sowohl auf Material- wie auch auf Komponentenebene zu erweitern.

Auf Materialebene wird eine neue semi-empirische Funktion für die mathematische Beschreibung der Flüssigwasserleitfähigkeit vorgeschlagen. Im Gegensatz zu bereits bestehenden Modellen beschreibt diese Funktion sowohl die Oberflächendiffusion wie auch den Kapillartransport, welche beide zum Flüssigkeitstransport im Bauteil beitragen.

Der zweite Teil dieser Arbeit besteht aus der Entwicklung eines einfachen experimentellen Verfahrens zur Bestimmung der Flüssigwasserleitfähigkeit unterschiedlicher Dämmmaterialien, die vor allem im Baubereich verwendet werden (z.B. Kalziumsilikat-Platte).

Zwei alternative Verfahren werden vorgeschlagen: Das erste basiert auf Desorptionsversuchen, das zweite Verfahren verwendet Messungen des Wärmeflusses, die mittels einer Heizplattenapparatur durchgeführt werden können.

Insbesondere das zweite Verfahren unterscheidet sich wesentlich von den in der Literatur zur Verfügung stehenden Ansätzen und bietetet im Vergleich zu diesen Vorteile, weil nur eine minimale Messausrüstung erforderlich ist (Heizplattenapparatur und Waage).

Darüber hinaus kann die Temperaturabhängigkeit der Flüssigwasserleitfähigkeit mit diesen Verfahren simultan bestimmt werden. Die experimentellen Ergebnisse werden verwendet, um ein numerisches Modell für die Simulation der gekoppelten Wärme- und Feuchtetransport in porösen Baustoffen zu validieren.

Eine weiterer Teil der Arbeit bestand darin, auf Bauteilebene sowohl Modelle für die Konvektion in Luftspalten, als auch Kriterien für die Auswirkung von Undichtheiten auf das Feuchterisiko inin der Baukonstruktion zu entwickeln.

Des Weiteren werden Modelle basierend auf Computational Fluid Dynamics (CFD) sowie vereinfachte Ansätze, die insbesondere für Langzeitsimulationen geeignet sind, entwickelt. Die Plausibilität dieser Ergebnisse wird durch numerische Beispielrechnungen und durch Vergleiche mit gemessenen Daten aus der Literatur analysiert.

Der letzte Teil dieser Arbeit betrachtet bauphysikalische Probleme, die in der Praxis vorkommen können, wie Schimmelwachstum hinter der Dämmung und das Auftreten von Bauschäden aufgrund eines zu hohen Wassergehaltes.

Auswirkungen der Luftleckagen hinsichtlich der Feuchtigkeitsverteilung werden untersucht. Verschiedene Systeme zur Abdichtung von Spalten an Balkenköpfe werden ebenfalls durch numerische Simulation analysiert.

Darüber hinaus wird das Verhalten von unterschiedlichen Gebäudebauteilen durch 2D- und 3D-Modellen simuliert, um allgemeine Kriterien zu definieren, die eine bauschadensfreie Planung gewährleisten.

Diese Arbeit zielt darauf ab, eine kurze aber vollständige Übersicht über das hygrothermische Verhalten von Baustoffen und Gebäudebauteilen zu geben. Innovative und detaillierte Charakterisierungsmethoden der physikalischen Vorgänge, aber auch Lösungsvorschläge für praktische bauphysikalische Probleme werden in dieser Arbeit vorgeschlagen.

Abstract

During recent years, energy efficiency in buildings has become one of the main priorities of European energy policy, playing a major role in the so called "20-20-20 targets" (20% reduction of greenhouse gas emissions, increasing renewable energy production to 20%, and a 20% improvement in the EU´s overall energy efficiency).

Great effort has to be made not only in the construction of new buildings, but also in the refurbishment of existing ones, according to high energy-efficiency standards. In particular, concerning the building envelope, adequate design and materials have to be employed to ensure high quality and damage-free constructions. Avoiding detailed description of well-known standard solutions, this work focuses on problems that continue to represent a challenge from the technical point of view, such as internal insulation systems.

Indeed, critical moisture conditions may occur in cases where internal thermal insulation is applied. In the long term, vapor diffusion from the inside of the building may lead to high levels of moisture content behind the insulation and even to the damage of components made of organic materials, such as timber beams.

A prerequisite for the correct planning of an insulation system is a deep knowledge of vapor and liquid water transfer in the employed materials. A lot of work in both numerical modeling and experimental research has been recently gone into this topic; the purpose of this work is to extend the resultant knowledge, focusing on both the material and the component scale.

Concerning the material scale, a semi-empirical function for mathematical description of the liquid water diffusivity is proposed by giving a physical interpretation of both phenomena contributing to the liquid transfer, means surface diffusion and capillary suction.

The second task of this work is the development of simple experimental procedures for the determination of the liquid water diffusivity in materials used for building insulation (for example, calcium silicate board).

Two alternative procedure are proposed: the first one based on desorption tests and the second one on heat flux measurements carried out with a hot plate apparatus. In particular, the second proposed procedure differs substantially from the other methods generally used to the same aim. The main advantages of the proposed method are the limited required equipment (only a guarded hot plate and a balance are used), and the fact that the dependence of the liquid water diffusivity on the temperature can be determined.

The experimental results are employed to validate a numerical model, including

coupled heat and moisture transfer in porous building materials introduced in the first part of the thesis.

On the component scale, great effort is made in the modeling of convection in air gaps and for evaluating its effect on moisture risk in constructions. Models based on computational fluid dynamics (CFD), as well as simplified models, suitable for long time simulations, are proposed. The plausibility of the results is analyzed by means of numerical tests and comparison with measured data from the available literature.

In the last part of the thesis, solutions for practical building physics problems, such as mold germination behind internal insulation and at timer beam ends, are introduced.

Considerations on the air-tightness of the building envelope are made by taking into account the impact of air leakages on moisture distribution. Different sealing systems for the wall-beam junction are analyzed. Furthermore, the behavior of building components sensitive to moisture damage is simulated by means of both 2D and 3D models, with the results compared.

This work aims to be a brief but complete overview of the hygrothermal behavior of building materials and components, presenting an innovative and detailed characterization of the physical background, but also proposing solutions for practical building physics problems.

Contents

Chapter 1

Introduction

The presence of excessive relative humidity at the surfaces of domestic rooms is unhealthy for the inhabitants since it may lead to mold growth. Moreover, water content above the critical value inside building components increases the risk of structural damage, such as the corrosion of steal or degradation of timber elements. In order to avoid such moisture damages, significant research effort has been recently made in terms of the optimization of the thermal insulation systems and of the building components. In the case of new buildings, standard solutions can generally be employed, guaranteeing adequate moisture protection. In addition, thermal losses through the building envelope can be minimized by applying external insulation, which represents the best solution from the technical and building physics point of view in temperate or cold climates.

Much more challenging is retrofitting of listed or historical buildings in order to improve their energy efficiency. In many cases the only practicable method is the application of internal insulation, since the aesthetics of the façade have to be preserved. Indeed, this solution presents some critical issues: on the one hand thermal bridges can hardly be avoided; on the other hand there is risk of condensation between the external wall and the insulation [56] [67].

The commonly used approach for avoiding moisture risk consists in applying a vapor retarder to the internal side of the insulation, so as to prevent moisture ingress due to diffusion. This procedure may present some critical issues however, since in practice it is a challenge to avoid gaps in the vapor tight layer (see [28] for how this challenge can be mastered).

An alternative way to handle this task is by employing capillary active materials as thermal insulation (e.g. cellulose or calcium silicate). In this case the insulating layer remains vapor-open, but it can dry out from the internal side due to capillary action. In fact, during the heating period, vapor diffusion and liquid water transfer often occur in opposite directions within the insulation, keeping the water content under the critical level.

The risk of moisture damage increases even more if the building envelope is not perfectly air tight. Moreover, timber components (e.g. timber beams), sensitive to moisture damage, are frequently present in historical buildings.

In such critical cases, numerical models can be helpful for the prediction of moisture risk, for the correct dimensioning of the insulation system and for the se-

lection of proper materials. Such hygrothermal models may integrate a thermal analysis for prediction of the energy performance of the building carried out with proper tools [27] [29].

Even if software based on mathematical models describing non-steady heat, air, moisture and salts transfer in construction materials (e.g. [26]) are already available on the market, the influence of convection inside air cavities enclosed in the construction is taken in to account only in few cases. 3D studies of constructions are also rare, since the high complexity of the models requires a great deal of numerical effort.

The present work aims principally to extend the current knowledge on these topics and is divided into three parts:

1. The first part includes a literature review addressing various models for heat and moisture transfer, based on the assumption of macroscopic continuous material for deriving energy and mass balance equations (chapter 2). Existing material models are described and compared, analyzing advantages and draw-backs. A new function for the mathematical description of the liquid water diffusivity is proposed (section 2.2.2). The effects of air cavity and cracks on moisture distribution are taken into consideration (chapter 3). Since complex models including CFD (computational fluid dynamic) require extremely high computational effort, a simplified numerical model, capable of long-term simulations, is developed (section 3.3). This simplified model is validated through comparison with CFD simulations and with measured data (section 3.4).

2. In the second part of the thesis (chapter 4) material properties of capillary-active materials (e.g. calcium silicate boards and blow-in cellulose) are determined. Particular effort is dedicated to the assessment of the liquid water diffusivity of calcium silicate. Two new methods are proposed for determination of this material function: the first one based on inverse simulation of desorption experiments (section 4.5) and the second one employing heat flux measurements performed on humid specimens (section 4.6). Moreover, the models introduced in the first part are validated through comparison with experimental data measured in the laboratory.

3. The last part of the thesis focuses on studying internal insulation systems and the the influence of convection on hygrothermal behavior of building components, considering also 3D-details (chapter 5). The scope is to derive from the simulation results practical design guidelines for planners. Typical building physics applications are taken into consideration such as moisture protection at embedded timber beam ends.

Chapter 2

Diffusive heat and moisture transfer in porous building materials

The theory of heat and mass transfer proposed in this chapter is mainly based on the works of the following authors:

- Balance equations system: Luikov [47] and Künzel [44]

- Moisture storage and capillary transfer: Krischer [41], Künzel [44] and Krus [42]

- Vapor diffusion: Krischer [41], Künzel [44] and Bednar [9]

- Effective thermal conductivity (conduction, radiation and pore-scale diffusion): Krischer [41]

Improvements of the state of the art are proposed for modeling the liquid water diffusivity (paragraph 2.2.2) and the vapor diffusion resistance factor (paragraph 2.2.4). A new empirical correlation which describes the liquid water diffusivity as a function of temperature and water content is introduced. Since liquid water transfer and vapor transfer occur simultaneously inside the porous matrix, difficulties arises in measuring and modeling separately these two phenomena, especially in the moisture range where their relevance is comparable. Taking into account this difficulty, different modeling approaches for the vapor diffusion resistance are compared and tested with experimental data (see also sections 4.4.1 and 4.6).

2.1 Balance equations

In the middle of the last century, Luikov [47] and Krischer [41] separately proposed to describe time-dependent heat, air and moisture transfer in porous hygroscopic materials through a system of coupled partial differential equations. They

derived these equations by imposing the equilibrium balance of energy and moisture within an representative element of volume (REV). Such "phenomenological-approach" assumes the porous medium as continuous on the macroscopic scale. Some years later Whitaker [75] obtained an equivalent system of equations starting from a microscopic-scale approach.

Neglecting the flux of dry air due to total pressure drops, the energy and moisture balances can be described by the following system:

$$\begin{cases} \dfrac{\partial H}{\partial t} = -\nabla \cdot (\dot{\mathbf{q}} + h_v \boldsymbol{j}_v + h_w \boldsymbol{j}_w) + S_h \\[2mm] \dfrac{\partial u}{\partial t} = -\nabla \cdot (\boldsymbol{j}_w + \boldsymbol{j}_v) + S_w \end{cases} \tag{2.1}$$

Where H represents the volumetric enthalpy, u the water content, $\dot{\mathbf{q}}$ the thermal flux per square meter; h_v and h_w the specific enthalpy of vapor and liquid water; $\boldsymbol{j}_w$ and $\boldsymbol{j}_v$ the liquid water and vapor fluxes per square meter; S_h and S_w the energy and mass sources.

The system (2.1) is suitable for describing heat and moisture transfer in porous media under the following main assumptions according to Whitaker ([75] pag. 193, [22]):

- The solid phase is a rigid matrix in a inertial frame

- The three phase system is in local equilibrium

- The porous medium is continuous at macroscopic scale

- Pressure variation are small so they do not affect thermodynamic properties

- Liquid water is free water. No chemically bound water is taken into account

Notice that, according to the assumption of continuity, material transfer and storage parameters can be defined inside the REV as functions of local temperature and water content. These parameters are derived considering the following temperature and pressure ranges: $0\ ^\circ C < \vartheta < 40\ ^\circ C$; $p \approx 1\ bar$ (ice formation is not taken into account in this work).

2.2   Moisture storage and moisture transfer

The capability of a porous material to storage water depends on the volumetric distribution of the open pores and on their shapes.

2.2.1   Moisture storage

For quantifying the adsorption and the desorption behaviors of porous materials it is advantageous to define first the pore distribution function $w(\tilde{r})$, varying between zero and one ([41], pag. 228). Assuming cylindrical pores and the pore radius as representative pore dimension we can write:

$$\frac{dw(\tilde{r})}{d\tilde{r}} = n(\tilde{r})\frac{V(\tilde{r})}{V_P} \tag{2.2}$$

where $n(\tilde{r})$ is the number of pores of radius $\tilde{r}$ inside the REV, $V(\tilde{r})$ is the volume of a single pore of radius $\tilde{r}$ and V_P is the total pore volume inside the REV. According to this model, the local water content $u(\mathbf{x}, t)$ is defined as follows:

$$u(\mathbf{x}, t) = \rho_w \int_{r_{min}}^{r(\mathbf{x},t)} \frac{dw(\tilde{r})}{d\tilde{r}} d\tilde{r} \tag{2.3}$$

where r_{min} is the minimum pore radius present in the material and $r(\mathbf{x}, t)$ is the radius of the largest wet pore at time t and position $\mathbf{x} = [x, y, z]$. ρ_w is the density of liquid water. It follows that the water content at free saturation u_f is given by:

$$u_f = \rho_w \int_{r_{min}}^{r_f} \frac{dw(\tilde{r})}{d\tilde{r}} d\tilde{r} \tag{2.4}$$

where r_f is the radius of the largest wet pore at free saturation.
Applying the assumption of local equilibrium between liquid and vapor phases introduced above, the water content can be calculated according to equation (2.3) as a function of the pore radius $r(\mathbf{x}, t)$, if the pore distribution $w(\tilde{r})$ is known.
Moreover, the water content can be expressed as a function of the capillary pressure $p_c(\mathbf{x}, t)$, considering the following relation between pore radius and capillary pressure:

$$r(\mathbf{x}, t) = \frac{2\sigma_w}{p_c(\mathbf{x}, t)} \tag{2.5}$$

Notice that the derivation of the water content from equation (2.3) presents practical difficulties since it requires previous knowledge of the function $w(\tilde{r})$. Moreover the assumption made above of cylindrical pores does not apply for real materials. These reasons make advantageous the use of empirical correlations describing the trend of the water content as a function of the capillary pressure or the relative humidity $\varphi(\mathbf{x}, t)$. In this work the following equation proposed by [35] is employed:

$$u(\mathbf{x}, t) = \frac{u_f}{1 + \left(\frac{p_c(\mathbf{x},t)}{k_1}\right)^{k_2}} \tag{2.6}$$

where k_1 and k_2 are material specific empirical parameters and u_f is the water content at free saturation, which in this study is assumed to be approximately equal to the maximal water content.
Other correlations describing the water content as a function of the relative humidity can be found e.g. in [50], pag. 91-94.
Taking into account the Kelvin equation (2.7) which gives a relation between the capillary pressure, the relative humidity φ and the temperature in Kelvin T:

$$p_c(\mathbf{x}, t) = -\rho_w R_v T(\mathbf{x}, t) ln(\varphi(\mathbf{x}, t)) \tag{2.7}$$

equation (2.6) can be written as follows:

$$u(\mathbf{x}, t) = \frac{u_f}{1 + \left(\frac{-\rho_w R_v T(\mathbf{x},t) ln(\varphi(\mathbf{x},t))}{k_1} \right)^{k_2}} \qquad (2.8)$$

It can be observed that, in accordance with experimental evidence, the temperature dependence of the water content is almost negligible within the temperature range of interest for building physics [30].

2.2.2   Liquid water transfer

Liquid water transfer may occur in porous materials principally due to two phenomena, presenting different relevance at different relative humidity ranges (hence, at different water content ranges); these are surface diffusion and capillary suction.
As observed by Künzel ([44], pag. 25-26), surface diffusion may already occur at relative humidity below 50 %, whereas capillary transport becomes predominant in the so called super-hygroscopic region ($\varphi > \approx 95$ %). Considering these phenomena occur simultaneously and both of them can be expressed assuming the water content u as transfer potential, it is advantageous to describe the total liquid water flux using a single equation including both contributions.
According to Krischer ([41], pages 220-231), the total flux of liquid water per surface unit $\boldsymbol{j}_w$ can be described through the following equation:

$$\boldsymbol{j}_w = -k \nabla u \qquad (2.9)$$

where k is the liquid water diffusivity expressed in $[m^2/s]$. Krischer demonstrated that this parameter depends on the water content, on the material porous structure and on the temperature.
Referring to Poiseuille's law, which describes liquid transfer in a single cylindrical capillary, assuming one-dimensional transfer and employing an ideal material model with parallel cylindrical pores of different radii, the function $k(r, T)$ can be derived. The liquid water diffusivity results directly proportional to the surface tension of liquid water $\sigma_w(T(\mathbf{x}, t))$ and inversely proportional to the viscosity $\eta_w(T(\mathbf{x}, t))$ both of which are functions of the temperature (see table 2.1). Moreover, according to the model of Krischer, the liquid water diffusivity depends on the porous structure of the material and can be written in the following simple form:

$$k = \frac{\sigma_w}{\eta_w} \xi(r(\mathbf{x}, t)) \qquad (2.10)$$

where the factor $\xi(r(\mathbf{x}, t))$ depends only on the pore distribution and hence can be rewritten as a function of the water content u: $\xi(u(r))$. Note that the exact trend of the function $\xi(u)$ depends on the shape, dimension and distribution of the pores, and in general cannot be exactly derived using analytical procedures due to the complexity of the microscopic porous structure.
Häupl et al. [34] proposed an approximated closed-form for the liquid water diffusivity as a function of the water content, deriving it from the measured pore

size distribution. Using a different approach, in this study we introduce a new semi-empirical model, where not only the pore size distribution (hence the local water content), but also the position of the pores inside the REV are considered. It can be observed that ξ has to increase with u due to the fact that at higher water content, even the larger pores become capable of capillary transfer. In order to better understand this phenomenon, we consider two exemplary materials with equal water retention curve, but different liquid water diffusivity.

The representative elementary volume (REV) of the first material presents fine pores on the border and large pores in the center and is reported in figure 2.1 a). Liquid water can be transferred through the REV due to capillary forces even at low water content, since small capillaries constitute a continuous connection between different material zones. By increasing water content, also the interior part of the REV is gradually activated to the capillary transfer. For this reason, we expect the function $\xi(u)$ to increase monotonically, as shown in figure 2.1 c). The second case is characterized by inverse pore displacement, as shown in figure 2.1 b). In this case, capillary transfer may start only if moisture content overcomes a certain value, whereas below this value liquid water transfer occurs only due to surface diffusion inside the larger pores. The shape of the function $\xi(u)$ approximates a step-function, as shown in figure 2.1 d).

Real materials can be described as random combinations of these two limiting cases.

Now we are looking for a mathematical function, able to reproduce the trend of $\xi(u)$ according to the physical interpretation described above. Taking into account the values of the liquid water diffusivity measured by different authors ([41] and [42]), it can be observed that a sum of exponential functions is suitable to this aim. In particular, we identify the following function for describe the general material behavior:

$$\xi(u) = \frac{u}{u_f} \sum_{i=1}^{N} \xi_i^* 10^{\zeta_i \left(\frac{u}{u_f} - 1 \right)} \tag{2.11}$$

where the parameters ξ_i^* and ζ_i are material-specific, and the sum $\sum_{i=1}^{N} \xi_i^*$ represents the maximal value of the function $\xi(u)$ reached at free saturation $(u = u_f)$. Note that the exemplary cases reported in figure 2.1 a) and b) can be adequately described through equation (2.11) with $N = 1$ and $N = 2$ respectively.

For the cases taken into consideration, satisfactory agreement with real material behavior can be obtained assuming $N = 2$.

In figure 2.2 the curves resulting from equations (2.10) and (2.11) are used for interpolating experimental data published by Krischer [41] and by Krus [42]. Good agreement between empirical model and measurements is reached.

Even if equation (2.11) approximate adequately the experimental data, different functions can be considered for description of $\xi(u)$ (e.g. polynomial forms). Investigation of such alternative models has to be carried out in future research.

According to equations (2.9) and (2.10), the liquid water flux is proportional to the gradient of the relative humidity as follows:

$$\boldsymbol{j}_w = -k\frac{du}{d\varphi}\nabla\varphi = -\frac{\sigma_w}{\eta_w}\xi\frac{du}{d\varphi}\nabla\varphi \qquad (2.12)$$

Traditional methods for experimental determination of the liquid water diffusivity k ([41], [54], [42], [14]) requires knowledge of the function $u(\mathbf{x}, t^*)$ which describes the water content distribution inside the material sample at given times t^*. The direct measurement of $u(\mathbf{x}, t^*)$ requires complex equipment such as e.g. a nuclear magnetic resonance (NMR) apparatus. In this study alternative simplified procedures are proposed, avoiding determination of water content profiles. One of these procedures is based on the inverse determination of the function $\xi(u)$ employing simple desorption experiments (see section 4.5). The second one is based on heat flux measurements by means of a heat plate apparatus (see section 4.6).
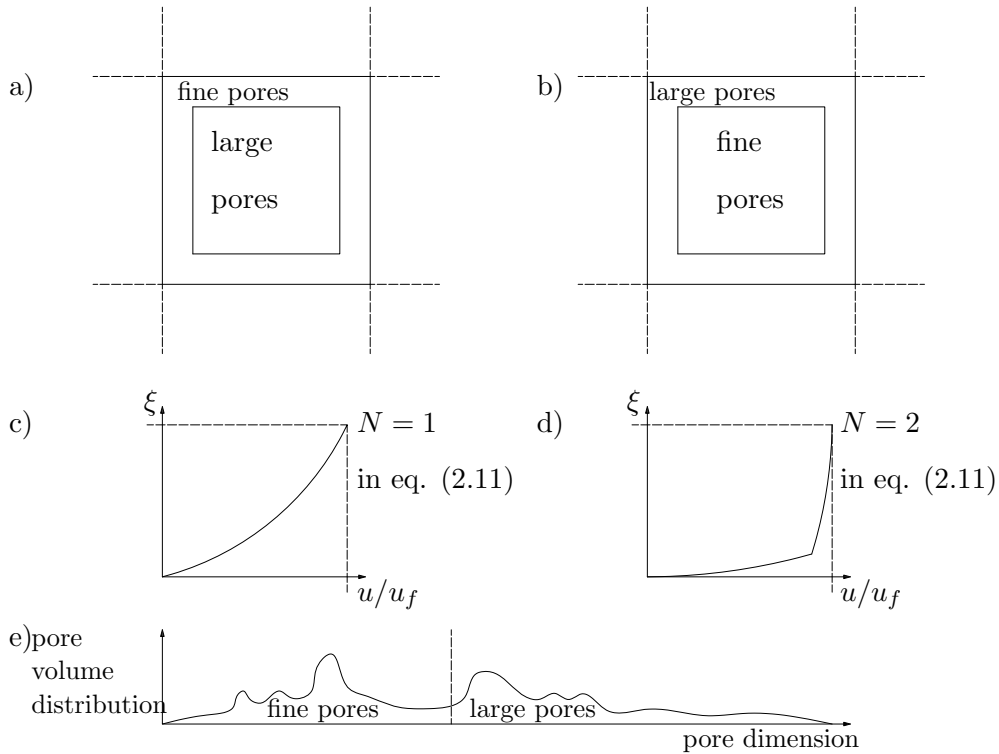
Figure 2.1: Representative elementary volumes (REV) of two different exemplary materials (a and b); plausible trends of the function $\xi(u)$ (c and d) and pore volume distribution (e)
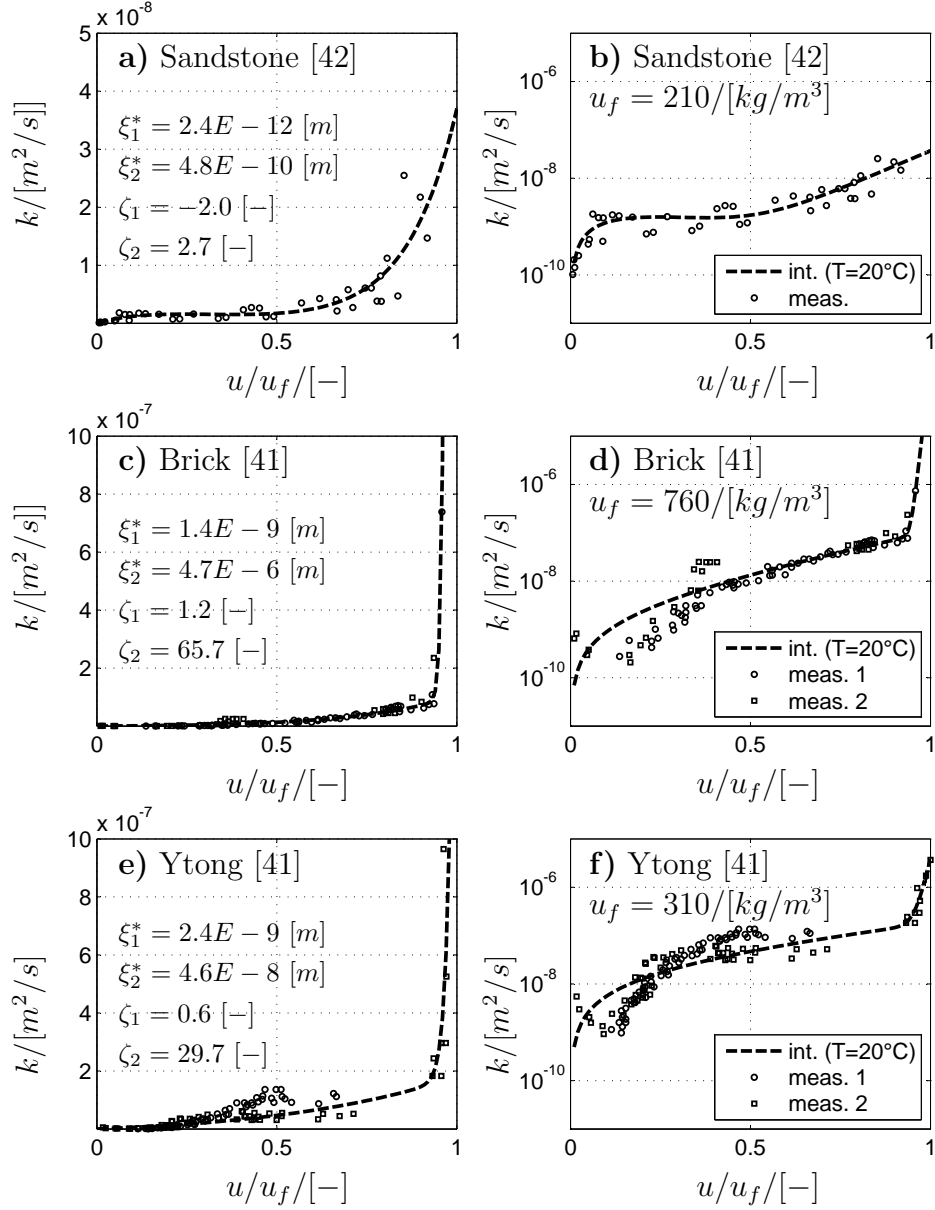
Figure 2.2: a), c), e): Liquid water diffusivity of sandstone, ytong and brick measured by [42] (water uptake test, NMR measurements) and by [41] pages 238-239 (meas.1: drying test, meas.2: water uptake test). Interpolation curves obtained by equations (2.10) and (2.11) with $N = 2$. b), d), f): Logarithmic scale representation

Table 2.1: Values of surface tension and viscosity of liquid water ([41] pag. 223)

T [°C]	σ_w [N/m]	η_w [kg/(ms)]
0	$75.5 \cdot 10^{-3}$	$1.750 \cdot 10^{-3}$
20	$72.7 \cdot 10^{-3}$	$0.959 \cdot 10^{-3}$
40	$69.2 \cdot 10^{-3}$	$0.453 \cdot 10^{-3}$
60	$65.8 \cdot 10^{-3}$	$0.343 \cdot 10^{-3}$

2.2.3 Vapor diffusion

According to different authors (e.g. [41], pag. 166, [9] and [44]), the diffusive flux of vapor in air can be described through the following equation:

$$\boldsymbol{j}_v = \frac{D_v p_v}{2R_v T^2}\nabla T - \frac{D_v}{R_v T}\nabla p_v \tag{2.13}$$

Considering that, inside porous materials, not all the space is available for the transfer of vapor molecules, the diffusion resistance factor μ is introduced and equation (2.13) is modified as follows:

$$\boldsymbol{j}_v = \frac{1}{\mu}\left(\frac{D_v p_v}{2R_v T^2}\nabla T - \frac{D_v}{R_v T}\nabla p_v\right) \tag{2.14}$$

many authors ([9], [44] pag. 22) observed that the first term of the right hand side in equation (2.14) is negligible within the temperature and pressure ranges considered in this work (see section 2.1). Hence the flux $\boldsymbol{j}_v$ can be simplified as follows:

$$\boldsymbol{j}_v = -\frac{1}{\mu}\frac{D_v}{R_v T}\nabla p_v \tag{2.15}$$

with:

$$p_v = \varphi\, p_s(\vartheta) \tag{2.16}$$

where $p_s(\vartheta)$ represents the saturation pressure of water vapor given by the following equation [6]:

$$p_s = 610,94 \cdot e^{\frac{17,625 \cdot \vartheta}{243,04+\vartheta}} \tag{2.17}$$

and ϑ is the temperature in [°C] ($\vartheta = T - 273.15$). Taking into account the definition of p_v given by equation (2.16), equation (2.15) can be written as follows:

$$\boldsymbol{j}_v = -\frac{1}{\mu}\frac{D_v}{R_v T}\left(p_s(T)\nabla\varphi + \varphi\frac{dp_s}{dT}\nabla T\right) \tag{2.18}$$

In the literature, numerous formula describing water vapor diffusivity in air are present. In civil engineering it is common to use the formula proposed by Schirmer [64], cited by [41] pag. 175:

$$D_v = 2,3 \cdot 10^{-5} \frac{p_{atm}}{p_v + p_{atm}} \left(\frac{T}{273}\right)^{1,81} \qquad [m^2/s] \qquad (2.19)$$

In this work the constant value $D_v = 2.662 \cdot 10^{-5} [m^2/s]$ is assumed, according to [26]. This value is obtained from equation (2.19) with: $\vartheta = 25,5$ $[°C]$; $\varphi = 0.5$ $[-]$ and $p_{atm} = 10^5$ $[Pa]$.

2.2.4   Diffusion resistance factor

The vapor diffusion resistance factor μ introduced in the previous section can be considered as a function of the water content.

Two opposing phenomena affect the transfer of vapor. On the one hand, increasing water content inside the material leads to reduced space for diffusion of water molecules in the gaseous phase. This phenomenon may produce an enhancement of the vapor diffusion resistance factor μ as assumed in [26]. On the other hand, by increasing the water content, bypass effects due to thin capillary filled by liquid water may occur, leading to an effective reduction of μ (water island theory according to [57], cited by [42]).

Experimental results obtained by means of dry and wet cup tests have shown that the total water flux increases with increasing water content inside the test specimens (see e.g. [61] and section 4.4 of this work). Since in this kind of tests vapor diffusion and liquid water transfer occur simultaneously and are superimposed, no exact knowledge of the only vapor flux contribution can be obtained (consider that at low relative humidity (dry cups, $\varphi < 0.5$) vapor diffusion is largely predominant whereas at higher water content liquid transfer increases). In order to enhance the knowledge on this phenomena, a different test based on heat flux measurements is introduced in section 4.6.1.

The diffusion resistance coefficient μ can be written as a function of φ using the following equation, as proposed in [71]:

$$\mu = \frac{\mu_0}{a\varphi^n + 1} \qquad (2.20)$$

This function does not consider the fact that, when the water content approximates the free saturation value, no more space is available for vapor transfer and hence μ should increase significantly. For taking into account this phenomenon, equation (2.20) can be modified as follows:

$$\mu = \frac{\mu_0}{\left(1 - \frac{u(\varphi)}{u_f}\right)(a\varphi^n + 1)} \qquad (2.21)$$

however equation (2.21) does not lead to any significant improvement of the results, according to the experimental cases considered in the following of this work. This can be explained considering that at high water contents the liquid water transfer becomes the dominant transfer mechanism, while vapor diffusion plays just a minor role, and taking into account the water island theory cited above.

2.3   Heat transfer

For calculation of the total heat flux through a porous moist material, it is necessary to identify the different heat transfer mechanisms. The influence of moisture is particularly important, since by increasing water content u the thermal transfer results significantly grown.

In this section, the approach proposed by Krischer [41] for modeling the apparent thermal conductivity of porous materials is applied to the REV, including all factors which significantly affect the total heat transfer. In other words, a form of $\lambda_{eff}(T, u)$ is determined for describing the total conductive and radiative heat flux, according to the following equation:

$$\dot{\mathbf{q}} = -\lambda_{eff}(T, u)\nabla T \qquad (2.22)$$

Notice that in equation (2.22) the enthalpy fluxes associated with the macroscopic mass transfer are not included. These have already been accounted in the first equation of system (2.1), through the terms $h_v\mathbf{j}_v$ and $h_w\mathbf{j}_w$

2.3.1   The model of Krischer for dry materials

According to the model of Krischer, a porous dry material is ideally constituted by alternated solid and gaseous phases disposed on parallel planes, as shown in figure 2.4 a). The effective thermal conductivity can assume two limit values depending on the direction of the phases. The first case considers phases parallel to the heat flux. According to this collocation, the main part of the thermal energy is transferred due to conduction through the phase presenting higher thermal conductivity. Hence, the effective thermal conductivity assumes in this case its maximal value λ_I which is given by the following equation:

$$\lambda_I = (1 - \psi)\lambda_{sm} + \psi\lambda_P \qquad (2.23)$$

where ψ is the total porosity of the material defined as follows:

$$\psi = \frac{V_P}{V} \qquad (2.24)$$

$$V_P = V - V_{sm} \qquad (2.25)$$

where V is the total volume, V_P is the pore volume and V_{sm} is the volume of the solid matrix.

The second limit case refers to an exemplary material with phases disposed perpendicularly to the heat flux direction. Hence, the effective thermal conductivity can be calculated with the following equation:

$$\lambda_{II} = \frac{1}{\frac{1-\psi}{\lambda_{sm}} + \frac{\psi}{\lambda_P}} \qquad (2.26)$$

In this case the entire heat flux crosses necessarily both the phases and the apparent thermal conductivity assumes its lowest value.

Real materials are in general random combinations of these two limit cases. Hence, the complex porous structure, constituted by cavities with various dimensions and shapes, can be idealized assuming parallel solid and gaseous phases, disposed in part perpendicularly and in part parallel to the heat flux.

In order to complete the model, it is necessary to introduce the weight parameter a which may assume values between 0 and 1. Thus, the total apparent thermal conductivity can be calculated as follows:

$$\lambda_{eff} = \frac{1}{\frac{1-a}{\lambda_I} + \frac{a}{\lambda_{II}}} \tag{2.27}$$

In figure 2.3 the effective thermal conductivity normalized with respect to λ_{sm} is reported as a function of the porosity, varying the parameter a and assuming $\lambda_P < \lambda_{sm}$ as a constant.

Assuming that the main mechanisms of thermal transfer inside the single pores are conduction and radiation[1], the equivalent thermal conductivity of the pores λ_P is given by the following equation:

$$\lambda_P = \lambda_g + \lambda_{Rad} \tag{2.28}$$

where the conductive term λ_g is added to the radiative term λ_{Rad} defined as follows [41]:

$$\lambda_{Rad} = \frac{4\sigma_S d_m}{\frac{2}{\varepsilon} - 1} T^3 \tag{2.29}$$

being σ_S the Stefan-Boltzman constant, ε the emissivity of the cavity surfaces, T the absolute temperature and d_m the mean diameter of the cavity. Since ε is in general not known, it is advantageous to introduce the coefficient C_{Rad}, to be determined by comparison with experimental data:

$$C_{Rad} = \frac{4\sigma_S d_m}{\frac{2}{\varepsilon} - 1} \tag{2.30}$$

Considering that the filling gas inside the pores is humid air, the following constant value for λ_g is assumed in the following of this study:

$$\lambda_g = 0,0259 \qquad [W/(mK)] \tag{2.31}$$

For more accurate estimation of λ_g as function of temperature and relative humidity, correlations proposed in [68] can be employed.

Inside the solid phase the thermal transfer occurs due to heat conduction. The temperature dependence of the thermal conductivity λ_{sm} is in general negligible, hence in this work it is considered as a constant.

---

[1]Natural convection inside the single pores does not take place, since the Rayleigh number Ra is very low. According to [20], natural convection in enclosures filled by air may occur for $Ra \geq 10^3$
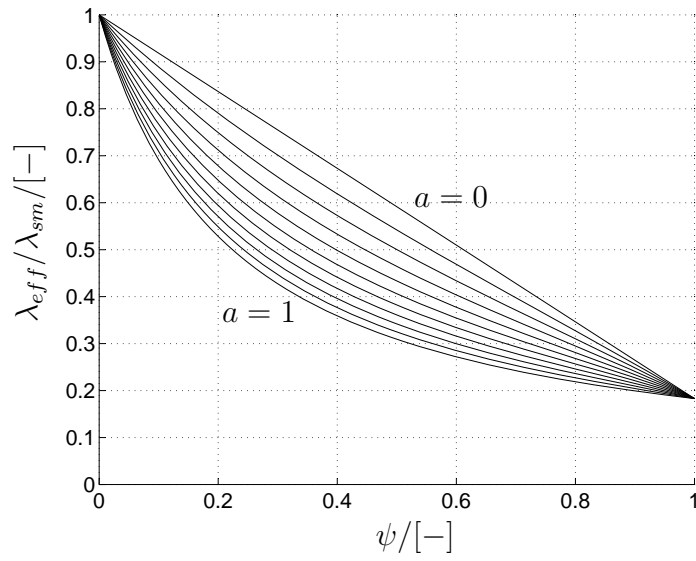
Figure 2.3: Normalized effective thermal conductivity as a function of the porosity and of the parameter a for a dry material (lines spaced with $\Delta a = 0, 1$)
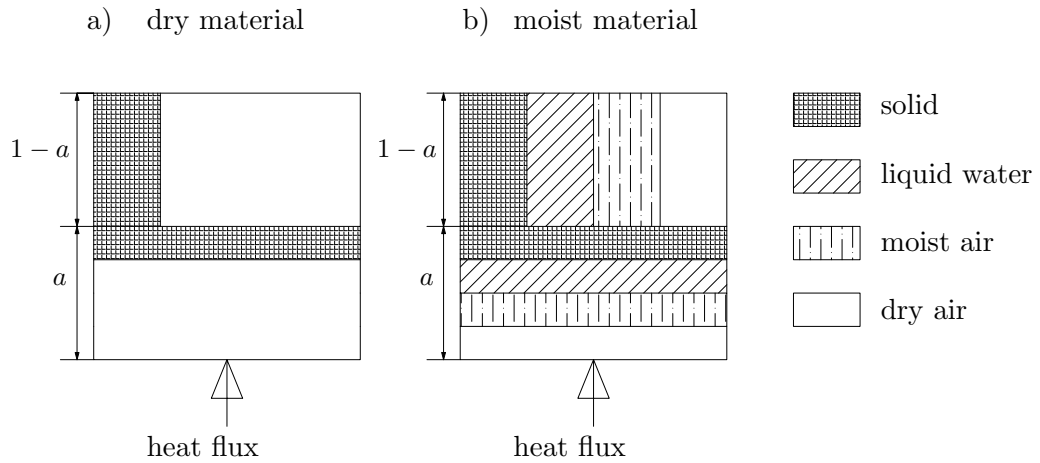

Figure 2.4: a) Model of Krischer for dry materials. b) Model of Krischer for moist materials

2.3.2 Influence of moisture on the effective thermal conductivity

Experimental evidence ([41], [51]) shows that by increasing the moisture content inside porous materials, the effective thermal conductivity also increases. This can be in part explained considering that enclosed air inside the pores is substituted with liquid water, which has thermal conductivity about twentyfive times higher; however, the main reason of this phenomenon is the enthalpy transfer connected to the mass fluxes in liquid and gaseous phases.

The thermal conductivity of liquid water can be described as a function of the temperature through the following polynomial function [60]:

$$\lambda_w = 0,557 + 0,0022\ \vartheta - 1,051 \cdot 10^{-5}\ \vartheta^2 + 1,081 \cdot 10^{-8}\ \vartheta^3 \qquad [W/(mK)] \quad (2.32)$$

The energy flux associated to the macroscopic mass transfer through the REV is already included in the first equation of system (2.1), through the terms $\boldsymbol{j}_v h_v$ and $\boldsymbol{j}_w h_w$. Microscopic mass transfer occurring inside the single pores may also affect the total energy transfer. In fact, water may evaporate at the warm moist surfaces of the pore and condensate at the cold surfaces transferring its latent heat of condensation. For taking into account this phenomena, the following equation proposed by Krischer can be employed:

$$\lambda_{diff} = \frac{\varphi D_v}{R_v T} \frac{p_0}{p_0 - p_s} h_{vl} \frac{dp_s}{d\vartheta} \qquad (2.33)$$

Where h_{vl} is the latent heat of evaporation at 0 °C and p_0 is the ambient pressure at standard conditions, assumed to be equal to the atmospheric pressure:

$$p_0 = p_{atm} \qquad (2.34)$$

The derivative of the saturation pressure with respect to the temperature can be obtained from (2.17) as follows:

$$\frac{dp_s}{d\vartheta} = \left(\frac{17,625}{243,04 + \vartheta} - \frac{17,625 \cdot \vartheta}{(243,04 + \vartheta)^2} \right) \cdot 610,84 \cdot e^{\frac{17,08\vartheta}{234,2+\vartheta}} \qquad (2.35)$$

2.3.3 The Krischer model for moist materials

The model of Krischer for dry materials introduced above (paragraph 2.3.1) can be extended in order to describe thermal conductivity of moist materials (figure 2.4 b). In addition to the solid and air layers, a liquid water layer is introduced. Moreover, the total pore fraction is supposed to be divided in two parts. In the first one, defined by the weight parameter b, moisture diffusion is supposed to occur and the associated enthalpy flux has to be included. The second part, corresponding to the fraction $1-b$, is not affected by micro diffusive mass transfer. Hence, in this second air fraction, heat transfer occurs just due to conduction and radiation, as explained above. Similarly to the dry material model, two limiting cases, described by the following equations, can be defined:

$$\lambda_I = (1-\psi)\lambda_{ms} + \psi_w\lambda_w + b(\psi-\psi_w)(\lambda_P + \lambda_{diff}) + (1-b)(\psi-\psi_w)\lambda_P \quad (2.36)$$

$$\lambda_{II} = \frac{1}{\frac{1-\psi}{\lambda_{sm}} + \frac{\psi_w}{\lambda_w} + \frac{b(\psi-\psi_w)}{\lambda_P+\lambda_{diff}} + \frac{(1-b)(\psi-\psi_w)}{\lambda_P}} \quad (2.37)$$

with:

a	Volume fraction weight parameter	b	Weight parameter mass diff.
λ_{sm}	Thermal conductivity of solid matrix	λ_P	Eq. thermal conductivity of the pores
λ_w	Liquid water thermal conductivity	ψ	Total porosity
λ_{diff}	Eq. thermal conductivity for mass diffusion	ψ_w	Volume fraction of liquid water

The described model is appropriate in case the material does not present closed air cavities which are not accessible to the moisture. If closed pores are present, an extended model proposed by Ochs can be employed [51].

Note that in the original model of Krischer ([41], pag. 274), the parameter b takes into account the total enthalpy flux due to mass diffusion. However, in this work we have already included the macroscopic mass diffusion in the first equation of system (2.1). For this reason, this parameter assumes here a different meaning, including only microscopic enthalpy transfer which may occur inside the single pores. Because of the experimental difficulties to separate macroscopic enthalpy fluxes overcoming the REV from the microscopic transfer, and considering this second contribution rather small, is here assumed: $b = 0$. Further investigation on this parameter has to be carried out in future research.

2.4   Energy storage

According to the material model introduced in the previous section, the volumetric enthalpy H can be described as follows:

$$H = (1-\psi)H_{sm} + \psi_w H_w + (\psi-\psi_w)H_g \quad (2.38)$$

where H_{sm}, H_w and H_g are the enthalpies of the solid matrix, of the liquid water and of the humid air included inside the pores respectively. H_{sm} is described by the following equation:

$$H_{sm} = \rho_{sm}\ c_{sm}\ \vartheta \quad (2.39)$$

where ρ_{sm} and c_{sm} are the density and the specific heat capacity of the solid matrix respectively.

The term H_w is described by means of the following equation:

$$H_w = \rho_w \, c_w \, \vartheta \tag{2.40}$$

where $c_w \approx 4186 \; [J/(kg \; K)]$ is the isobaric specific heat capacity of liquid water. Hence, the mass specific enthalpy of liquid water is defined by equation (2.41):

$$h_w = c_w \, \vartheta \tag{2.41}$$

The volumetric enthalpy of the humid air H_g is given by equation (2.57) introduced in the following section.

2.5 Enthalpy of the humid air

Within the temperature and pressure ranges which are of interest in the present work (see section 2.1), the following assumptions can be introduced [7]:

- The gaseous phase behaves like a mix of ideal gases

- Liquid water is assumed as incompressible

- The quantity of solved gas in the liquid phase is negligible

under these assumptions, the state equations for ideal gases (2.42), (2.43), (2.44) as well as the Dalton low, given by equation (2.45), apply:

$$p_{tot}V = (N_a + N_v)RT \tag{2.42}$$

$$p_a V = N_a RT \tag{2.43}$$

$$p_v V = N_v RT \tag{2.44}$$

$$p_{tot} = p_a + p_v \tag{2.45}$$

Equations (2.43) and (2.44) can be written in the following forms:

$$p_a = \rho_a R_a T \tag{2.46}$$

$$p_v = \rho_v R_v T \tag{2.47}$$

with:

$$\rho_a = \frac{N_a MM_a}{V} \tag{2.48}$$

$$\rho_v = \frac{N_v MM_v}{V} \tag{2.49}$$

$$R_a = \frac{R}{MM_a} \tag{2.50}$$

$$R_v = \frac{R}{MM_v} \tag{2.51}$$

where MM_a and MM_v are the molar masses of dry air and water respectively. The mass fraction of water in air is defined as follows:

$$X = \frac{M_v + M_w}{M_a} \tag{2.52}$$

where M_v is the mass of water vapor and M_w is the mass of liquid water. If no liquid water is present, it applies:

$$X_v = \frac{M_v}{M_a} \tag{2.53}$$

in this case the following expression is derived from (2.53), (2.43) and (2.44):

$$X_v = \frac{M_{m,w} N_v}{M_{m,a} N_a} = 0,622 \frac{p_v}{p_a} = 0,622 \frac{p_v}{p_{tot} - p_v} \tag{2.54}$$

at saturation it applies: $p_v = p_s$, thus equation (2.54) can be written as follows:

$$X_s = 0,622 \frac{p_s}{p_{tot} - p_s} \tag{2.55}$$

in a mixture of ideal gases the total enthalpy is equal to the sum of the enthalpies of the various components. Hence, the specific volumetric enthalpy of the gas mixture is obtained as follows:

$$H_g = \frac{M_a}{V} h_a + X_v \frac{M_a}{V} h_v \tag{2.56}$$

From (2.56) it follows:

$$H_g = \rho_a h_a + X_v \rho_a h_v \tag{2.57}$$

h_a and h_v are the enthalpy of dry air and of the water vapor for mass unit respectively. It applies:

$$h_a = c_{p,a} \vartheta \tag{2.58}$$

where ϑ is the temperature in Celsius degree and $c_{p,a}$ is the specific isobaric heat capacity of dry air. h_v is described by means of the following equation:

$$h_v = h_{vl} + c_{p,v} \vartheta \tag{2.59}$$

where $c_{p,v} \approx 1,86 \cdot 10^3 \quad [J/(kg\ °C)]$ is the isobaric specific heat capacity of the water vapor and $h_{vl} \approx 2502\ [kJ/kg]$ is the specific evaporation heat of water at $0\ °C$.

2.6 Driving equations in porous domains with temperature and relative humidity as system variables

Rewriting the system (2.1) with temperature T and relative humidity φ as dependent variables and setting the sources terms equal to zero ($S_h = 0$, $S_w = 0$) the following system is obtained:

$$
\begin{cases}
\dfrac{\partial H}{\partial \varphi}\dfrac{\partial \varphi}{\partial t} + \dfrac{\partial H}{\partial T}\dfrac{\partial T}{\partial t} = -\nabla \cdot (D_{e,T}\nabla T + D_{e,\varphi}\nabla \varphi) \\[2ex]
\dfrac{\partial u}{\partial T}\dfrac{\partial T}{\partial t} + \dfrac{\partial u}{\partial \varphi}\dfrac{\partial \varphi}{\partial t} = -\nabla \cdot (D_{m,T}\nabla T + D_{m,\varphi}\nabla \varphi)
\end{cases}
\tag{2.60}
$$

where the functions $u(T, \varphi)$ and $H(T, \varphi)$ are given by equations (2.8) and (2.38) respectively; the coefficients $D_{e,T}$, $D_{e,\varphi}$, $D_{m,T}$ and $D_{m,\varphi}$ can be written as functions of temperature and relative humidity as follows:

$$
D_{e,T} = \lambda_{eff} + (h_{l,v} + c_{p,v}T)\frac{\varphi D_v}{\mu R_v T}\frac{dp_s}{dT}
\tag{2.61}
$$

$$
D_{e,\varphi} = (h_{l,v} + c_{p,v}T)\frac{p_s D_v}{\mu R_v T} + c_{p,w}Tk\frac{du}{d\varphi}
\tag{2.62}
$$

$$
D_{m,T} = \frac{\varphi D_v}{\mu R_v T}\frac{dp_s}{dT}
\tag{2.63}
$$

$$
D_{m,\varphi} = \frac{p_s D_v}{\mu R_v T} + k\frac{du}{d\varphi}
\tag{2.64}
$$

The solution of system (2.60) is obtained by calculating the variables $T(\mathbf{x}, t)$ and $\varphi(\mathbf{x}, t)$ as functions of position and time, once boundary and initial conditions are assigned.

Notice that the driving equations are in general non-linear since the material-specific transfer coefficients depend on the variables of the system. This fact increases significantly the mathematical difficulties in finding a solution.

2.7 Analytical solutions for linear problems

Analytical solutions for the problem defined above (section 2.6) can be found only if the system of driving equations is linear and for a limited set of cases, presenting simple geometry and boundary conditions. For the majority of practical applications an analytical solution cannot be found, however the analytical approach still presents significant interest for two reasons: first, it provides good insight into the meaning of the material parameters influencing the physical phenomena; moreover analytical solutions, when available, can be used as accurate benchmarks for numerical schemes.

Numerous studies on this topic, which differ for the employed mathematical methodologies and for the type of assumed boundary conditions, are available in the literature.

Since the material properties are in general temperature and moisture dependent, Luikov and Mikhailov proposed to solve the problem by parting the domain in zones where the transfer coefficients are constant assuming an average value of the transport parameters in each zone. The same technique has been employed by Chiba and Sugano [17]. Solutions for problems with a symmetrical geometry (slab, cylinder, sphere) and for a single material domain have been obtained in [52] and [53]. Kulasiri and Woosdhead [43] proposed a method of solution valid for an infinite slab with first-type boundary conditions (temperature and moisture imposed on the surface). Solutions for third-type boundary conditions (temperature and moisture dependent convective heat and mass fluxes imposed through the boundary), were proposed by Pandey, Srivastava and Mikhailov [48] and in other works [45],[58] (in [58] the Laplace transformation technique has been employed). Solutions for 2 and 3D geometries has been found by Duarte and Ribeiro [23],[24]. In all these studies, constant conditions on the boundary were assumed. An analytical solution for one-dimensional problem with periodic boundary conditions has been proposed in [31].

2.8 Numerical approaches for solving non-linear problems

For the majority of real problems no analytical solution is available but numerical approaches can be employed. In recent times, numerical studies on heat and mass diffusion in porous materials have been published by numerous authors.

Lobo [46] compared the numerical quality of different finite difference (FD) schemes. Künzel [44] and Grunewald [33] developed solutions, based on the finite volume method (FVM), whereas Janssen used the finite element method (FEM) [39]. Other authors employed commercial FEM-based software (e.g. Comsol [73], Fluent [72] and Abaqus [69]).

One of the main differences between the models developed by the authors cited above concerns the choice of the moisture transfer potential. Till now, there is no general agreement on this point which is of great interest since it has influence on the solver performance and on the quality of the results. Moreover it has been observed that, due to the non linearity of the problem, the selection of the transfer potential is crucial for guarantee conservative numerical results.

Within a recent study, Janssen [38] tested three possible moisture transfer potentials namely: relative humidity, capillary pressure and negative logarithm of the inverse of the capillary pressure (φ, p_c and $-log(p_c)$). His results show that the first two variants (φ and p_c) are advantageous in terms of numerical performances if compared with the third one.

Alternatively so-called "mixed schemes", including simultaneously two different moisture potentials, can be employed. These solutions present the advantage that exact mass conservation and good numerical efficiency is guaranteed. They have

been tested by different authors (e.g. [16], [39]) and in combination with different numerical methods (FDM, FVM or FEM).

The transfer potential for moisture employed in this work is the relative humidity (also called water activity by some authors) (see section 2.6). Even if this formulation leads to a numerical schema that do not guarantee conservative results, the error can be kept within an acceptable range employing adequate numerical parameters. For more details on this point see [10] and [11], where the numerical quality of the solution and the solver performance have been tested in hygroscopic and super-hygroscopic range (relative humidity $\varphi > 0.95$).

The system of driving equations (2.60) has been implemented in the FEM based software Comsol which allows to solve non-linear systems of partial differential equations presenting the following generic form:

$$e_a \frac{\partial^2 \mathbf{u}}{\partial t^2} + d_a \frac{\partial \mathbf{u}}{\partial t} + \nabla\left(-c\nabla \mathbf{u} - \alpha \mathbf{u} + \gamma\right) + \beta \nabla \mathbf{u} + a\mathbf{u} = f \qquad (2.65)$$

with Neumann boundary conditions given by equation (2.66):

$$\vec{n} \cdot \left(-c\nabla \mathbf{u} - \alpha \mathbf{u} + \gamma\right) + q\mathbf{u} = g \qquad (2.66)$$

where the coefficients e_a, d_a, c, α, γ, β, a, f, q and g may depend on the variable $\mathbf{u}$ and on its derivatives with respect to time and position (for instance: $f = f(\mathbf{u}, \mathbf{u}_x, \mathbf{u}_{xx}, \mathbf{u}_t, \mathbf{u}_{tt})$). Equations (2.65) and (2.66) are solved using the Galerkin method.

Chapter 3

Modeling air cavities inclosed in the construction

In case air cavities or air gaps are present in the construction, a coupling approach is needed in order to describe energy and mass exchange between air and porous domains. The most exact way to handle this task is to calculate the velocity field inside the air-domain solving the Navier-Stokes equations due to computational fluid dynamics (CFD).

Studies concerning coupled modeling including CFD have been recently proposed by Defraeye [22] and Van Belleghem [70]. These authors have used the commercial program Fluent (finite volumes method) for solving the transfer equations inside the fluid domain and an own Heat-Air-Moisture code for diffusion inside the porous domain.

In this work, the same program (Comsol, finite elements method) is employed for solving the transfer equations in both the fluid and porous domains. Simulation models have been developed on two levels of complexity.

In the first level the transfer in air is fully coupled with diffusion in the porous domains employing CFD.

In the second level a simplified model that applies for forced convection in thin air gaps and does not require the solution of the Navier-Stokes equations is introduced. This so called "line-source" method, developed within this study and validated by comparison with CFD-results, is advantageous for long-term simulations since it presents reduced computational effort, if compared with CFD models.

3.1   Coupling approaches

Three different approaches for handling the interaction between porous and fluid domains are taken into consideration:

- Non-conjugate approach. This approach represents the simplest way for describing heat and mass exchange between fluid and porous domains. The temperature and moisture content inside the fluid, as well as the velocity field are not included in the simulation, but just considered as boundary

conditions of the porous domain. The boundary mass and energy fluxes are computed as function of the surface values of temperature and relative humidity through proper transfer coefficients (α for energy, β for mass).

- Semi-conjugate approach: also in this case transfer coefficients are employed for describing mass and energy fluxes at the domain boundaries. Indeed, the fluid conditions (temperature and water vapor density) are not assumed as inputs of the problem but computed by means of simplified numerical models. An example of semi-conjugate approach is the line-source method described in section 3.3.

- Conjugate approach: no previous knowledge of the transfer coefficients is required, since the fluid conditions are computed within the numerical model. In the fluid domains the velocity, pressure, temperature and moisture fields are obtained simultaneously by solving the Navier-Stokes equations and the balance equations for mass and energy.

3.2 Balance equations in air cavities

In this section the well known equations describing heat, air and moisture (HAM) transfer inside a fluid domain constituted by humid air are reported. The humid air is considered as a two-components gaseous mixture, including dry air and water vapor. The model applies under the following assumptions [22]:

- The mixture is not saturated

- Humid air is considered as an incompressible gas

- Thermal equilibrium between the mixture components applies

- No heat, mass or momentum sources are present

- Viscous heat dissipation is negligible

- Soret-effect (thermal diffusion) is negligible

- Pressure variations do not affect thermodynamic properties

- Potential and kinetic energy changes as well as pressure work are negligible

Hereby, the following system of partial differential equations can be derived.

3.2.1 Total mass balance

The total mass balance inside the air cavities is given by equation (3.1):

$$\frac{\partial \rho_g}{\partial t} = -\nabla \cdot (\boldsymbol{j}_g) \tag{3.1}$$

where ρ_g is equal to the sum of the densities of dry air ρ_a and of water vapor ρ_v:

$$\rho_g = \rho_a + \rho_v = \frac{M_a p_a}{RT} + \frac{M_v p_v}{RT} = \frac{p_g}{RT}\left(M_a x_a + M_v x_v\right) = \frac{p_g M_g}{RT} \qquad (3.2)$$

the total convective mass flux $\boldsymbol{j}_g$ is expressed as follows:

$$\boldsymbol{j}_g = \rho_g \mathbf{v} = \rho_a \mathbf{v}_a + \rho_v \mathbf{v}_v = \boldsymbol{j}_a + \boldsymbol{j}_v \qquad (3.3)$$

where the total fluxes of dry air and of water vapor $\boldsymbol{j}_a$ and $\boldsymbol{j}_v$ are give by a convective and a diffusive contribution as follows:

$$\boldsymbol{j}_a = \rho_a \mathbf{v}_a = \rho_a \mathbf{v} - D_a \nabla \rho_a \qquad (3.4)$$

$$\boldsymbol{j}_v = \rho_v \mathbf{v}_v = \rho_v \mathbf{v} - D_v \nabla \rho_v \qquad (3.5)$$

Notice that, from equations (3.3), (3.4) and (3.5) results that: $D_a \nabla \rho_a = -D_v \nabla \rho_v$.

The assumption of incompressible flow applied to equation (3.1), taking into account equation (3.3), leads the divergence of the velocity field to be equal to zero according to equation (3.6):

$$\nabla \cdot \mathbf{v} = 0 \qquad (3.6)$$

3.2.2   Vapor balance

The vapor balance can be written as follows:

$$\frac{\partial \rho_v}{\partial t} = -\nabla \cdot \left(\boldsymbol{j}_v\right) \qquad (3.7)$$

according to equation (3.5), equation (3.7) becomes:

$$\frac{\partial \rho_v}{\partial t} = -\nabla \cdot \left(\rho_v \mathbf{v} - D_v \nabla \rho_v\right) \qquad (3.8)$$

3.2.3   Energy balance

The energy balance within an infinitesimal volume element of gas mixture is given by equation (3.9):

$$\frac{\partial H_g}{\partial t} = -\nabla \cdot \left(-\lambda_g \nabla T + \boldsymbol{j}_a h_a + \boldsymbol{j}_v h_v\right) \qquad (3.9)$$

where the volumetric enthalpy H_g is defined according to equation (2.57), the thermal conductivity of the gaseous mixture (humid air) λ_g is given by equation (2.31), the dry air and water vapor fluxes $\boldsymbol{j}_a$ and $\boldsymbol{j}_v$ are given by equations (3.4) and (3.5) respectively, whereas the enthalpies h_a and h_v are expressed according to equations (2.58) and (2.59).

3.2.4 Momentum balance

For determination of the velocity distribution in the gaseous phase, the following Navier-Stokes equations for a Newtonian incompressible flow are employed:

$$\rho_g \frac{\partial \mathbf{v}}{\partial t} + \rho_g \left(\mathbf{v} \cdot \nabla\right) \mathbf{v} = \nabla \cdot \left(-p\mathbf{I} + \eta \nabla \mathbf{v}\right) + \rho_g \mathbf{g} \tag{3.10}$$

where p is the total pressure, $\mathbf{I}$ denotes the identity matrix and η is the dynamic viscosity of the gas mixture. In case of natural convection, the buoyancy forces, caused by density differences in the presence of gravitational field, are taken into account through the Boussinesq approximation. Considering that the gas mixture is assumed to be incompressible and the total pressure nearly constant, the density of the gas mixture ρ_g depends only on the temperature and the water vapor concentration through equation (3.2). Hence, it can be written as a first order truncated Taylor series as follows:

$$\rho_g(T, x_v) = \rho_{g,0} + \left(\frac{\partial \rho_g}{\partial T}\right)_0 \Delta T + \left(\frac{\partial \rho_g}{\partial x_v}\right)_0 \Delta X_v \tag{3.11}$$

where X_v is defined by equation (2.54), the subscript 0 denotes the reference state and it applies: $\Delta T = T - T_0$ and $\Delta X_v = X_v - X_{v,0}$.

Moreover, the total pressure can be written as sum of a static and a dynamic contribution, according to the following equation:

$$\nabla p = \nabla p_{stat} + \nabla p_{dyn} \tag{3.12}$$

where the gradient of the static pressure is given by equation (3.13):

$$\nabla p_{stat} = \rho_{g,0} \mathbf{g} \tag{3.13}$$

taking into account equations (3.11), (3.12) and (3.13), equation (3.10) becomes:

$$\rho_g \frac{\partial \mathbf{v}}{\partial t} + \rho_g \left(\mathbf{v} \cdot \nabla\right) \mathbf{v} = \nabla \cdot \left(-p_{dyn}\mathbf{I} + \eta \nabla \mathbf{v}\right) + \mathbf{g}\Delta \rho_g \tag{3.14}$$

where buoyancy term $\mathbf{g}\Delta \rho_g$ is given by equation (3.15), obtained taking into account the ideal gas equation:

$$\mathbf{g}\Delta \rho_g = \mathbf{g}\left[\left(-\frac{p_g M_g}{T^2 R}\right)_0 \Delta T + \left(\frac{(M_v - M_a)p_g}{RT}\right)_0 \Delta x_v\right] \tag{3.15}$$

3.2.5 Driving equations in air domains with temperature and relative humidity as system variables

The moisture balance and the energy balance given by equations (3.8) and (3.9) are following expressed employing temperature (T) and relative humidity (φ) as dependent variables:

$$F\frac{\partial \varphi}{\partial t}+\nabla \cdot (-D_{m\varphi a}\nabla \varphi - D_{mTa}\nabla T)$$
$$+ \varphi \left(\frac{\partial F}{\partial t} + \frac{\partial F}{\partial T}\mathbf{v}\cdot \nabla T\right) + F\mathbf{v}\cdot \nabla \varphi = 0 \tag{3.16}$$

$$\frac{\partial \varphi}{\partial t}F(h_v - h_a)+\frac{\partial T}{\partial t}\left[\varphi\frac{\partial F}{\partial T}(h_v - h_a) + F\varphi(c_{p,v} - c_{p,a}) + \rho_g c_{p,a}\right] =$$
$$- \mathbf{v}\cdot (A_\varphi \nabla \varphi + A_T \nabla T) - \nabla \cdot (-D_{e\varphi a}\nabla \varphi - D_{eTa}\nabla T) \tag{3.17}$$

where the transfer coefficients are defined as follows:

$$F = \frac{p_s}{R_v T} \tag{3.18}$$

$$D_{m\varphi a} = D_v F \tag{3.19}$$

$$D_{mTa} = D_v \varphi \frac{\partial F}{\partial T} \tag{3.20}$$

$$A_\varphi = (h_v - h_a)F \tag{3.21}$$

$$A_T = (h_v - h_a)\varphi\frac{\partial F}{\partial T} + \varphi F(c_{p,v} - c_{p,a}) + \rho c_{p,a} \tag{3.22}$$

$$D_{e\varphi a} = D_v(h_v - h_a)F \tag{3.23}$$

$$D_{eTa} = D_v(h_v - h_a)\varphi\frac{\partial F}{\partial T} + \lambda_g \tag{3.24}$$

At the interface between porous and fluid domains, continuity conditions for temperature and relative humidity as well as for total heat and mass fluxes, expressed by equations (3.25) to (3.28), are imposed:

$$[T(\mathbf{x}, t)]_{pd} = [T(\mathbf{x}, t)]_{fd} \qquad \mathbf{x} \in \partial \Omega \tag{3.25}$$

$$[\varphi(\mathbf{x}, t)]_{pd} = [\varphi(\mathbf{x}, t)]_{fd} \tag{3.26}$$

$$[D_{e,T}\nabla T(\mathbf{x}, t) + D_{e,\varphi}\nabla \varphi(\mathbf{x}, t)]_{pd} = [-D_{e\varphi a}\nabla \varphi(\mathbf{x}, t) - D_{eTa}\nabla T(\mathbf{x}, t)]_{fd} \tag{3.27}$$

$$[D_{m,T}\nabla T(\mathbf{x}, t) + D_{m,\varphi}\nabla \varphi(\mathbf{x}, t)]_{pd} = [-D_{m\varphi a}\nabla \varphi(\mathbf{x}, t) - D_{mTa}\nabla T(\mathbf{x}, t)]_{fd}$$
$$\tag{3.28}$$

where the subscripts pd and fd refer to porous and fluid domains respectively.

3.3 Line-source equations

The so called line-source model introduced in this section can be considered as a semi-conjugate coupling approach applied on a thin channel in which humid air is streaming due to forced convection.

The driving equations are obtained assuming one-dimensional transport of mass and energy along the channel axis. Streaming air is assumed to exchange water vapor and energy with the porous domains bordering the channel. The bulk air velocity $\mathbf{v}_b$ is assumed as constant along the gap axis and has to be given as an input, whereas the bulk density of vapor $\rho_{v,b}$ and the bulk air temperature T_b represent the dependent variables of the problem. The exchange of heat and moisture between air and porous boundaries is described by means of transfer coefficients (α and β).

Defining A as the cross section area, δV as the infinitesimal control volume and δS as the infinitesimal lateral surface of the channel, the balance equation for the generic bulk quantity Ξ_i transported by the streaming air can be written as follows:

$$\delta V \frac{\partial \Xi_i}{\partial t} = A \left(\Gamma_i(x) - \Gamma_i(x + \delta x) \right) + \Phi_i \delta S \tag{3.29}$$

where Φ_i represents a source term and Γ_i the convective flux of the bulk quantity Ξ_i which is defined as follows:

$$\Xi_i = \frac{\int_0^A \Xi_i(y) d\tilde{A}}{A} \tag{3.30}$$

Writing $\Gamma_i(x + \delta x)$ as the following truncated Taylor series:

$$\Gamma_i(x + \delta x) = \Gamma_i(x) + \frac{\partial \Gamma_i(x)}{\partial x} \delta x \tag{3.31}$$

and substituting (3.31) in (3.29) we obtain:

$$\delta V \frac{\partial \Xi_i}{\partial t} = -A \frac{\partial \Gamma_i(x)}{\partial x} \delta x + \Phi_i \delta S \tag{3.32}$$

dividing (3.32) by δV, considering that $\delta V = A\delta x$ and $\delta V = d\delta S$ we obtain:

$$\frac{\partial \Xi_i}{\partial t} = -\frac{\partial \Gamma_i(x)}{\partial x} + \frac{\Phi_i}{d} \tag{3.33}$$

where d represents the channel depth. The index i assumes the values 1 in case of mass balance and 2 in case of energy balance. By substituting in (3.33) the following terms:

$$\Xi_1 = \rho_{v,b} \tag{3.34}$$

$$\Xi_2 = H_{g,b} \tag{3.35}$$

$$\Gamma_1 = \mathbf{v}_b \rho_{v,b} \tag{3.36}$$

$$\Gamma_2 = \mathbf{v}_b H_{g,b} \tag{3.37}$$

$$\Phi_1 = \beta(p_{v,s} - p_{v,b}) \tag{3.38}$$

$$\Phi_2 = \beta(p_{v,s} - p_{v,b})h_v + \alpha(T_s - T_b) \tag{3.39}$$

we obtain:

$$\frac{\partial \rho_{v,b}}{\partial t} = -\mathbf{v}_b \frac{\partial \rho_{v,b}}{\partial x} + \frac{\beta(p_{v,s} - p_{v,b})}{d} \tag{3.40}$$

$$\frac{\partial H_{g,b}}{\partial t} = -\mathbf{v}_b \frac{\partial H_{g,b}}{\partial x} + \frac{\alpha(T_s - T_b)}{d} + \frac{\beta(p_{v,s} - p_{v,b})h_v}{d} \tag{3.41}$$

Equations (3.40) and (3.41) represent the balances of water vapor and energy in the air gap and the suffixes b and s refer to bulk and surface quantities respectively. The enthalpy of the steaming humid air H_g is given by equation (2.57) the density and the partial pressure of vapor (ρ_v and p_v respectively) are connected through the ideal gas equation (2.47).

3.4   Model evaluation

In this section both the conjugate and the line-source approaches presented above are tested by solving numerical problems with simple geometry and comparing the results with experimental data from other authors. The results reported in this part of the thesis have been in part already published in [49].

3.4.1   Comparison with measured data from the literature

In this section we consider the experiment performed by James et al. [37], concerning moisture buffering in overlapped gypsum boards bordering on one side with air streaming inside a channel. This experiment has been reproduced by means of 2D numerical simulations using both the line-source and the conjugate models.

In the conjugate model the velocity field is assumed to be stationary, thus the momentum and continuity equations in the air domain are not depending on temperature and relative humidity, which can vary during the time. A schematic representation of the experiment is shown in figure 3.1. The initial conditions inside the porous domain (gypsum boards) and the inlet conditions of the streaming air are reported in table 3.1.

The temporal trends of temperature and relative humidity measured by [37] at point **1** (see figure 3.1) are reported in figure 3.2 and in figure 3.3 respectively. In the same plots are reported also the results obtained within this study by means

of line-source and conjugate model, as well as numerical results from other authors cited by [37].

According to the conditions reported in table 3.1, during the first period of time the gypsum specimen absorbs moisture from the streaming air whereas during the second period it is dried.

A good agreement between all the numerical results can be observed. The deviations between the temperature trends are acceptable, if we consider that the absolute temperature variation is rather small. Taking into account the relative humidity, it can be observed some larger deviation between measured data and simulation results for both absorbing and drying phases. Since this behavior is common to all considered models, the deviation may be attributed to uncertainty affecting the input data.

The described heat end moisture transfer problem can be considered as one-dimensional, since relative humidity and temperature do not present significant variation along the x-axis. Moreover, the air flow in the channel can be considered as fully developed. This explains why models presenting different complexity produce similar results.

In the next section three more cases are taken into consideration for testing the models introduced above on more challenging two-dimensional instances. The aim is to analyze the deviations between different models.

Table 3.1: Initial conditions in the porous domain and air inflow conditions within the two time periods characterizing the experiment

Variable	Initial conditions porous domain	Inflow air $0h < t < 24h$	Inflow air $24h < t < 48h$
$\vartheta/[°C]$	23.3	23.8	22.5
$\varphi/[-]$	0.3	0.719	0.296

3.4.2 Comparing the line-source model with the conjugate model

In this section we consider three numerical tests, comparing the line-source model with the conjugate model. The first two cases (case A and B) are similar to the experiment described above, except for some differences concerning geometry, boundary and initial conditions. In particular, referring to figure 3.1, it applies: $L = 0.5\ m$; $h_{pd} = 1.6\ cm$ and $h_{fd} = 0.2\ cm$.

The last case study we take into consideration presents a 90° bended air channel inside a gypsum square domain of 10 cm side (see figure 3.4).

In table 3.2 the initial conditions inside the porous domain and the air inflow conditions are reported. The heat and mass transfer coefficients employed for the line-source model in equations (3.38) and (3.39) are in all cases: $\alpha = 46.2\ [W/(m^2 K)]$ and $\beta = 3 \cdot 10^{-7}\ [s/m]$ respectively.

In figure 3.5 the trends of temperature and relative humidity at positions **2** and **3** are reported.
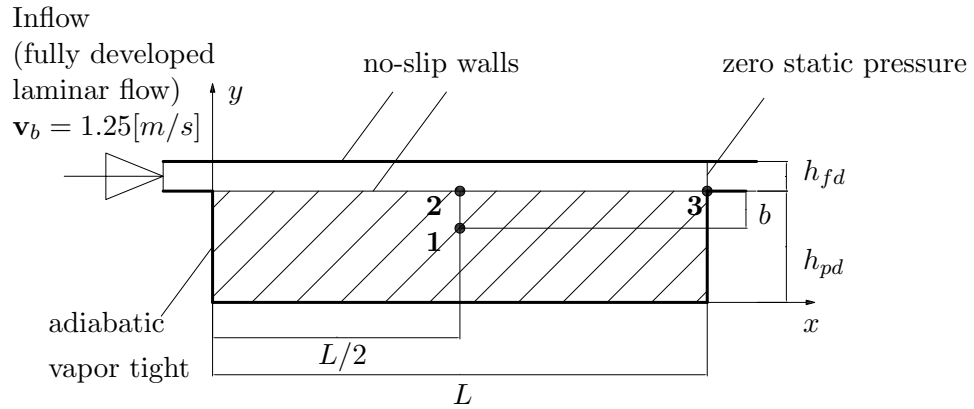
Figure 3.1: Schematic representation of the experiment executed by [37] and boundary condition of the numerical model. Dimensions: $b = 1.25\ cm$; $l = 50\ cm$; $h_{pd} = 3.75\ cm$ and $h_{fd} = 2.5\ cm$)
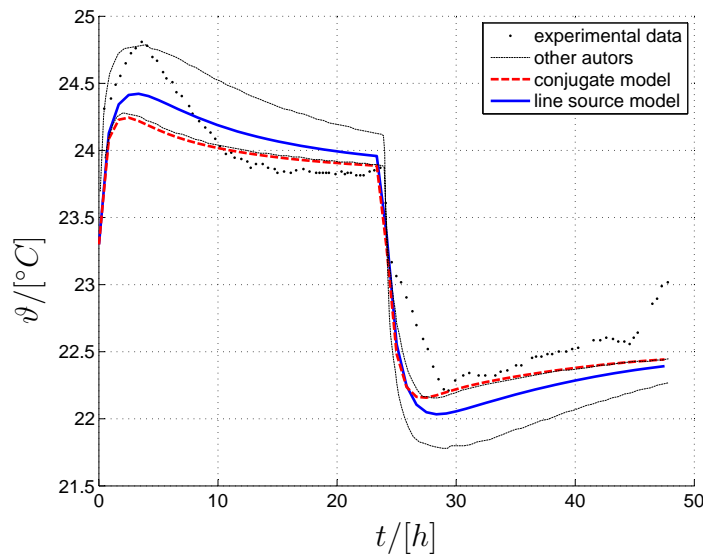

Figure 3.2: Temperature trend at point **1** plotted in figure 3.1
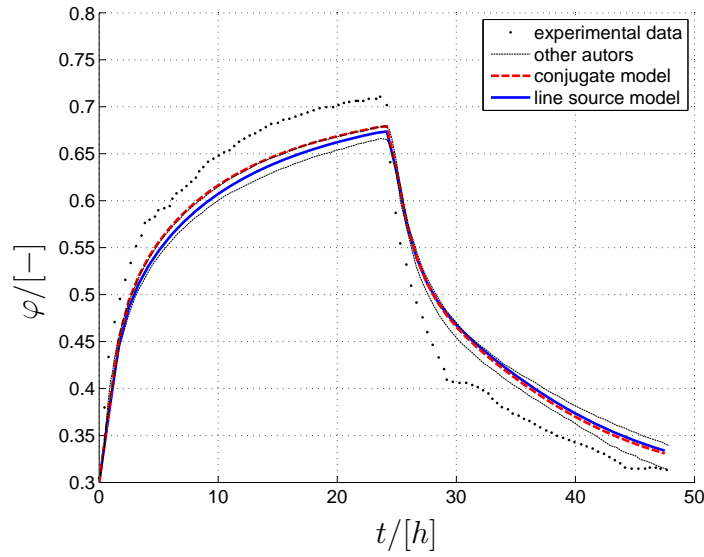
Figure 3.3: Relative humidity trend at point **1** plotted in figure 3.1

Table 3.2: Initial conditions in the porous domain (p.d.) and air inflow conditions for case A, B and C

| Variable	Initial conditions case A	Inflow air case A	Initial conditions case B	Inflow air case B	Initial conditions case C	Inflow air case C
$\vartheta/[°C]$	10	22	22	10	10	22
$\varphi/[-]$	0.5	0.7	0.7	0.5	0.5	0.7
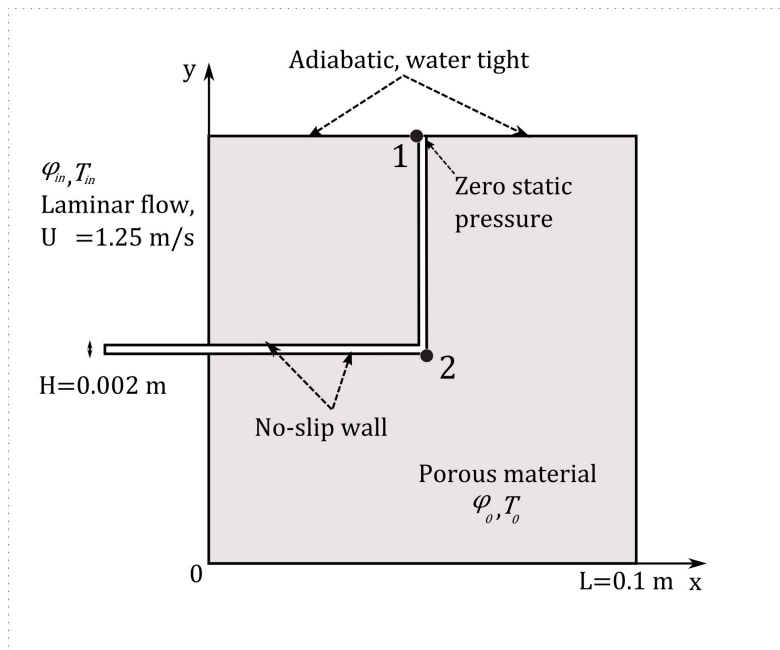
Figure 3.4: Geometry for case C

We first comment the results concerning case A. Here, the surface temperature increases standing, approaching the air temperature; the surface value of the relative humidity φ increases steeply during the first period and then decreases, approaching the value in the air.

An inverse behavior can be observer in case B, where the surface temperature decreases to the air value and the surface relative humidity first decreases and following increases approaching the air value.

These trends can be reproduced by means of both line-source and conjugate models with a good agreement.

In figures 3.6 and 3.8 temperature and relative humidity distributions are reported. Also in this case, a satisfactory agreement between the two models is observed. The good accordance between line-source and conjugate model can be explained since in cases A and B a fully developed flow occurs along the whole length of the channel.

The relative deviations between the models have been estimated according to the following parameter:

$$rd_u = \frac{u_{con} - u_{lin}}{u_{con}} \tag{3.42}$$

where u_{con} is the solution of the conjugate model and u_{lin} the one of the line-source. The results for cases A and B are shown in figures 3.7 and 3.9.

In case C (figures 3.10 and 3.11), the maximal deviation between line-source and conjugate model are reached at the channel corner or downstream of it, according to the fact that the flow presents a vortex and the assumption of constant heat and mass transfer coefficient applied in the line-source model is no more verified. However, the error remains also in this case within an acceptable range.
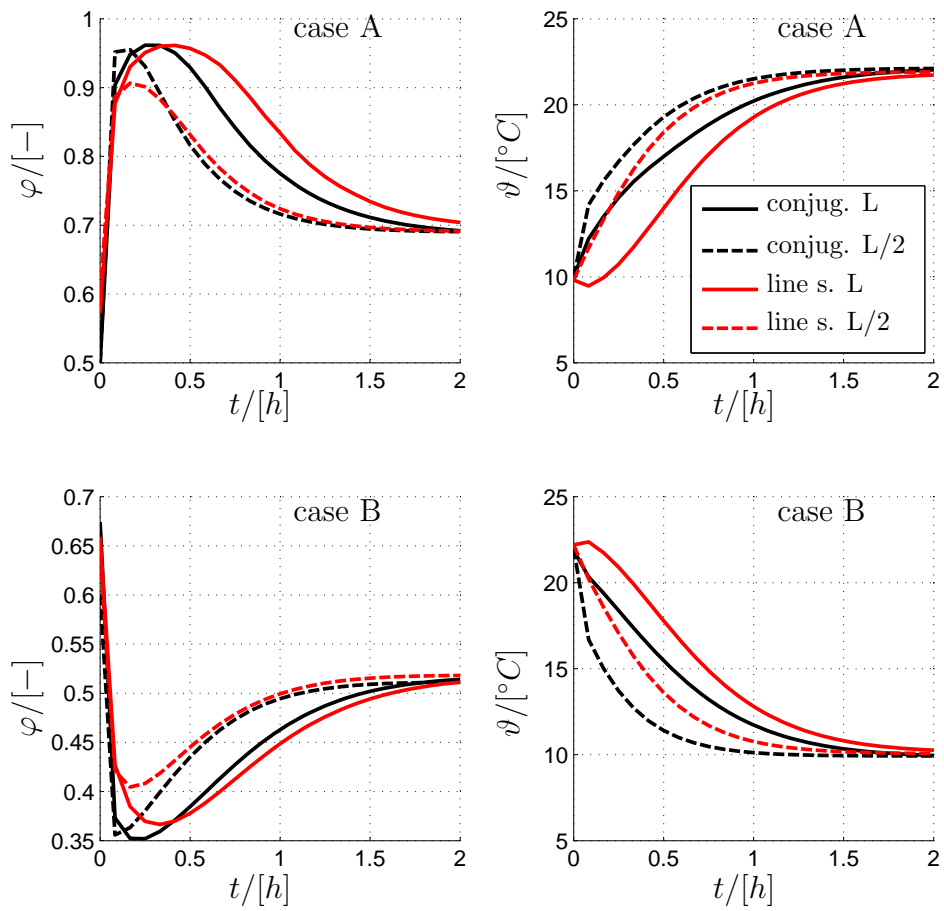
Figure 3.5: Relative humidity and temperature trends at points **2** ($L/2$) and **3** (L) (see figure 3.1); comparison between line-source and conjugate model
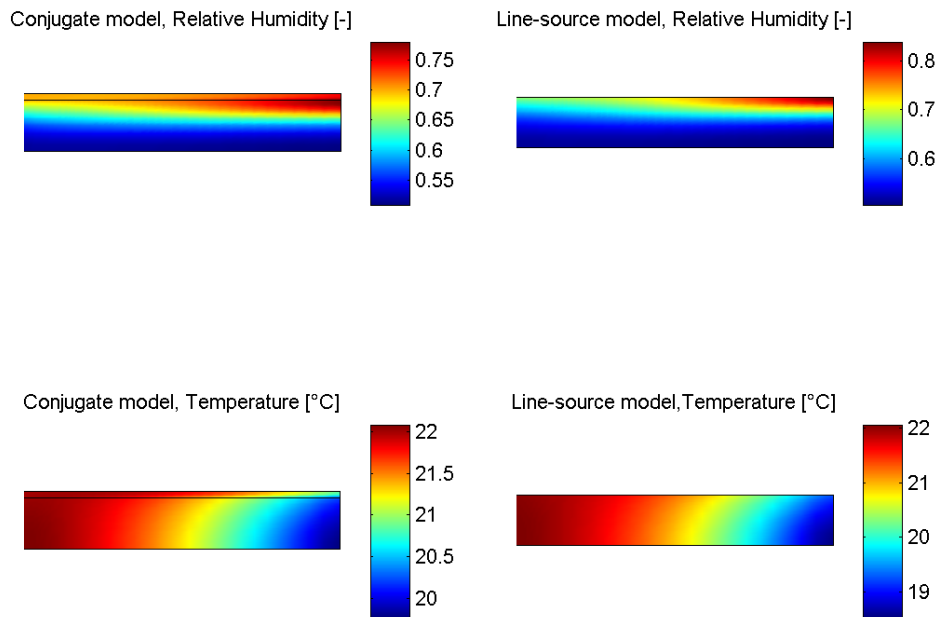
Figure 3.6: Relative humidity and temperature distribution for case A after 1 h
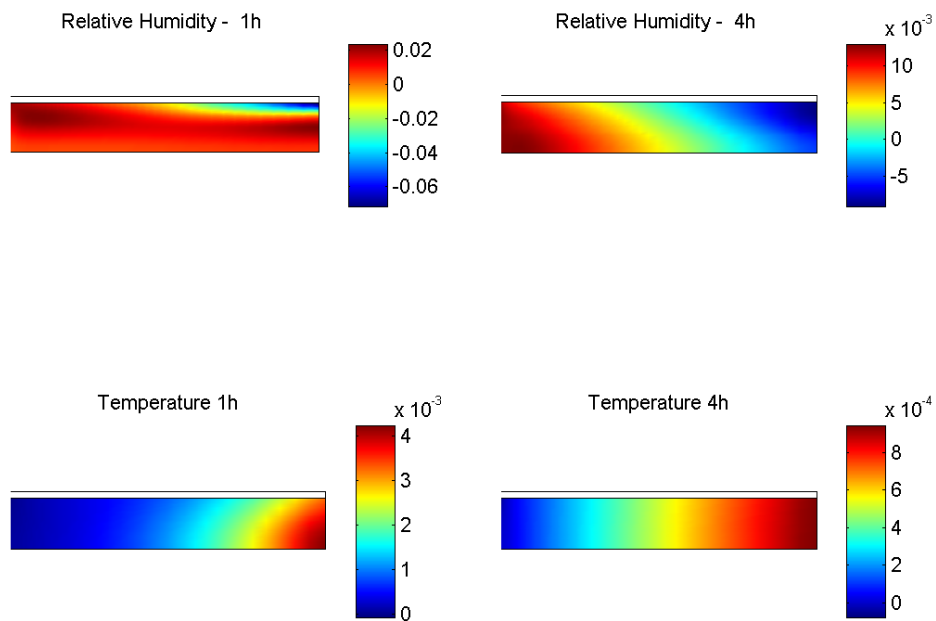
Figure 3.7: Relative deviations between line-source and conjugate models concerning relative humidity and temperature distributions for case A
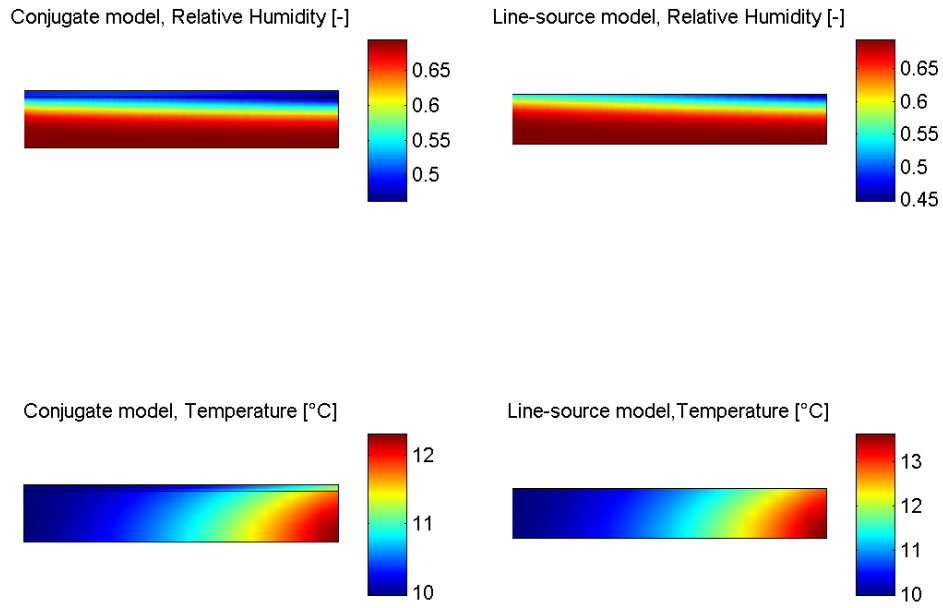
Figure 3.8: Relative humidity and temperature distribution for case B after 1 h
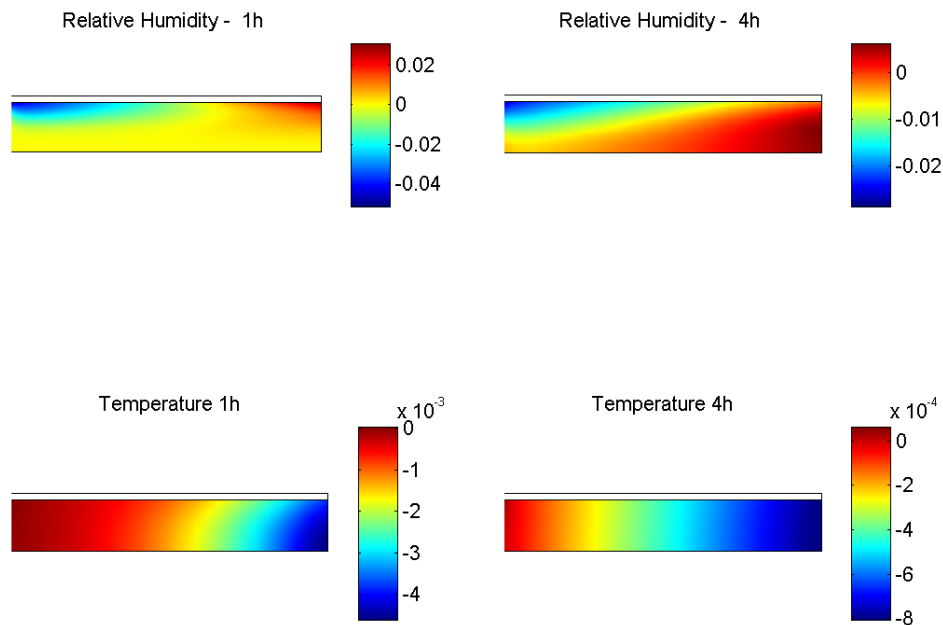
Figure 3.9: Relative deviations between line-source and conjugate models concerning relative humidity and temperature distributions for case B
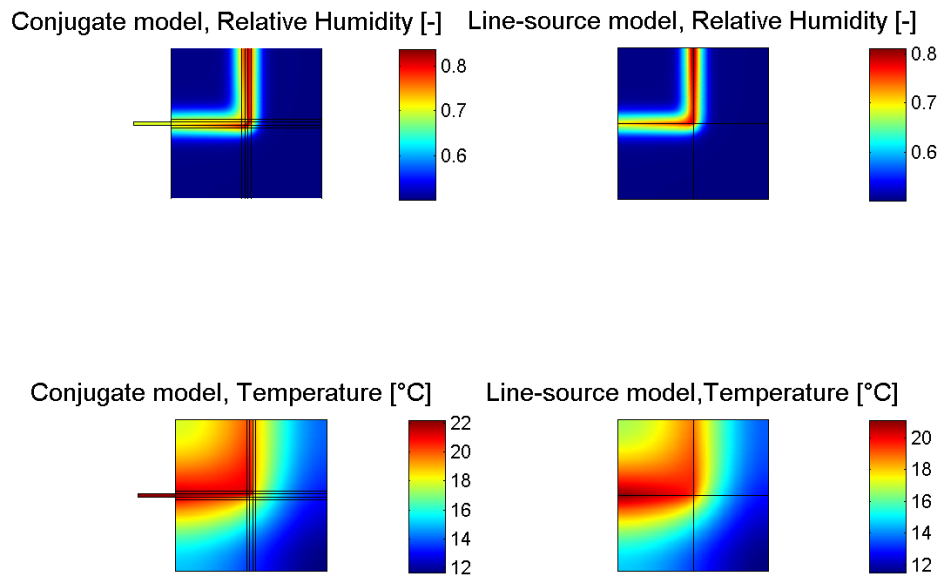
Figure 3.10: Relative humidity and temperature distribution for case C after 1 h
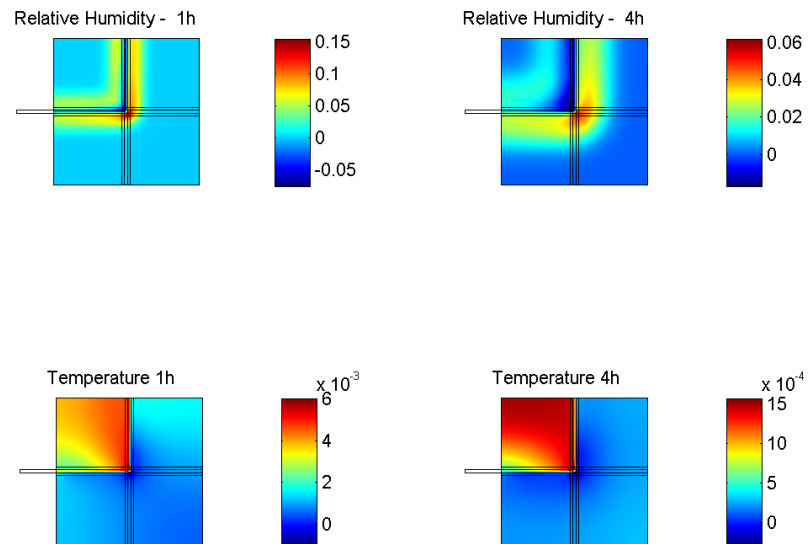
Figure 3.11: Relative deviations between line-source and conjugate models concerning relative humidity and temperature distributions for case C

Chapter 4

Determination of the material parameters and experimental validation of the model

In this chapter experimental results are employed for determination of the material parameters and for validation of the hygrothermal model described in chapter 2. The measurements have been performed on samples obtained from calcium silicate boards.

Firstly, standard methods are employed for characterization of the water storage function, of the porosity and of the diffusion resistance factor (sections 4.3 and 4.4). Then, two new experimental procedures for determination of the liquid water diffusivity are presented.

The first procedure is based on inverse simulation of simple desorption experiments (section 4.5); in the second one, heat flux measurements, performed on moist specimens by means of a heat plate apparatus, are employed (section 4.6). The proposed procedures are advantageous, compared to other methods generally used (e.g. [54], [42] and [14]), since no direct measurement of moisture distribution inside the specimens is required.

For the first procedure, a previous material characterization has to be performed. Once the other properties (such as bulk density, open porosity, diffusion resistance factor, water storage function and thermal conductivity) have been determined, the liquid water diffusivity is obtained by inverse simulation.

The second method does not requires any other previous measurement and can be directly used for simultaneous determination of liquid water diffusivity, thermal conductivity and diffusion resistance factor in the super-hygroscopic region.

4.1 Note on the material characteristics

Calcium silicate boards are composed of synthetic mineral xonotlite [1] mixed with randomly oriented cellulose fibers [61]. The choice of this material is motivated by the following reasons:

---

[1]Mineral xonotlite: $Ca_6[(OH)_2|Si_6O_{17}]$

- Calcium silicate is a capillary active material, hence liquid water diffusivity has large influence on the measured heat and mass transfer. This represents an important issue since one of the major aims of the present section is to set up simple experimental procedures for determination of this material property.

- Calcium silicate boards are simply workable by means of sawing and rubbing. Material samples with various geometry can be easily obtained.

- Calcium silicate boards are widely used as internal insulation in buildings.

4.2 Note on the convective heat and mass transfer coefficients

For determination of the diffusion resistance factor by means of dry and wet cup tests and for the simulation of desorption experiments, the knowledge of convective heat and mass transfer coefficients is required. To this aim, the empirical correlations reported below can be employed.

The mass transfer between the surface of a material sample and the surrounding air can be described through the following equation ([8], pag. 85):

$$j_v = \beta^*(\rho_{v,\infty} - \rho_{v,s}) \tag{4.1}$$

where β^* is the mass transfer coefficient; $\rho_{v,\infty}$ and $\rho_{v,s}$ are the density of water vapor in the air and at the surface respectively.

Similarly, the convective heat flux is described by equation (4.2):

$$\dot{q} = \alpha(T_\infty - T_s) \tag{4.2}$$

The heat and mass transfer coefficients are defined as follows:

$$\alpha = \frac{Nu_L \lambda_a}{L} \tag{4.3}$$

$$\beta^* = \frac{Sh_L D_v}{L} \tag{4.4}$$

where Nu_L and Sh_L are the average Nusselt and Sherwood numbers and L is the characteristic dimension of the system.

In case of natural convection, the Nusselt and the Sherwood numbers can be expressed as function of the Rayleigh number through a power low as follows:

$$Nu_L = c\ Ra_e{}^n \tag{4.5}$$

$$Sh_L = c\ Ra_m{}^n \tag{4.6}$$

the coefficients c and n have to be determined empirically.

In table 4.1 values determined by different authors in case of natural convection on horizontal plane are reported. The correlations present an uncertainty of

$\pm 50\,\%$ or more, compared to the experimental data. In particular, the correlation of Martorell et al. exp. presents deviations of the order of $40 - 60\,\%$ in the range $10^3 < Ra < 10^5$. Better engagement is obtained with results of numerical simulation ($\pm 5\,\%$ in the range $10^3 < Ra < 5 \cdot 10^5$; Martorell et al. num.)
These values have been determined with heat transfer experiments, however, according to the Lewis analogy, they apply also to the mass transfer.

Table 4.1: Values of the coefficients c and n of equations (4.5) and (4.6) for natural convection on horizontal plane [19]

Author	Fluid	validity	c	n
Bosworth exp.	unknown	laminar flow	0.710	0.250
Kitamura and Kimura exp.	air	$3.7E2 < Ra < 8E5$	1.307	0.200
Martorell et al. exp.	air	$2.9E2 \leq Ra \leq 3.3E5$	1.200	0.175
Martorell et al. num.	air	$8E2 \leq Ra \leq 2E6$	1.280	0.167

For natural convection on vertical surfaces, one of the following empirical correlations can be used:
Yovanovich and Jafarpur [77]:

$$Sh_L = 0.55\ Ra_m^{1/4} \tag{4.7}$$

Churchill and Chu [18], valid for $10^{-1} < Ra < 10^{12}$; $0 < Pr < \infty$:

$$Sh_L = \left(0.825 + \frac{0.387 Ra_m^{1/6}}{\left(1 + \left(\frac{0.437}{Sc} \right)^{9/16} \right)^{8/27}} \right)^2 \tag{4.8}$$

The Rayleigh number is defined for heat and mass transfer as follows:

$$Ra_h = Gr_h\ Pr \tag{4.9}$$

$$Ra_m = Gr_m\ Sc \tag{4.10}$$

Where the suffix h and m refer to heat and mass transfer respectively; Gr, Pr and Sc are the Grashof, the Prandlt and the Schmidt numbers, defined by equations (4.11), (4.12), (4.13) and (4.14):

$$Gr_h = \frac{g(T_s - T_\infty)L^3}{\frac{T_s+T_\infty}{2}\nu^2} \tag{4.11}$$

$$Gr_m = \frac{g\left(\rho_{v,s} - \rho_{v,\infty}\right)L^3}{\frac{\rho_{v,s}+\rho_{v,\infty}}{2}\nu^2} \tag{4.12}$$

$$Pr = \frac{\eta}{C_p\lambda_a} \tag{4.13}$$

$$Sc = \frac{\eta}{\rho_a D_v} \tag{4.14}$$

where η and ν are the dynamic and the cinematic viscosity of air.
Treating water vapor as an ideal gas, the following equation applies:

$$\rho_v = \frac{p_s}{R_v T}\varphi \tag{4.15}$$

substituting ρ_v in equation (4.1) and considering isotherm conditions, equation (4.16) is obtained:

$$j_v = \frac{\beta^* p_s}{R_v T}(\varphi_\infty - \varphi_s) \tag{4.16}$$

This equation gives the exchanged mass flux as a function of the difference between relative humidity in the air and at the surface. Introducing the parameter $\beta = \frac{\beta^*}{R_v T}$ the following form is obtained:

$$j_v = \beta p_s(\varphi_\infty - \varphi_s) \tag{4.17}$$

4.3 Measurement of the porosity and of the water storage function

In the hygroscopic region (up to about 95% relative humidity) the water storage function takes the name of absorption or desorption isotherm and can be measured by means of the desiccator method standardized in [5].
The measured data, interpolated with functions defined by equation (2.8), are reported in figure 4.1. As observed by different authors (e.g. [63]), for many materials there is hysteresis between absorption and desorption processes. This has been verified also within this work, determining the desorption curve from water saturated samples. In this case just one interpolation value is available at $\varphi \approx 0.52$. An additional value has been obtained after the desorption test by further humidification of the samples till $\varphi \approx 0.88$ (red line in figure 4.1).
Note that the water content at free saturation is supposed to be equal to the open porosity, which is determined by means of vacuum saturation experiments according to the method described in [1]. Moreover, no measured data in super-hygroscopic region ($\varphi > 0.95$) are available since for measurements in this range further equipment would be required (e.g. pressure plate apparatus or centrifuge apparatus [42]). Nevertheless, the determined material function presents sufficient accuracy for the purpose of this work.
In figure 4.2 the water content is represented as function of the capillary pressure logarithm, according to equation (2.6). The functions obtained in this study for adsorption and desorption behaviors are compared with the water storage function included in the database of the program Delphin [26], where no hysteresis is considered.
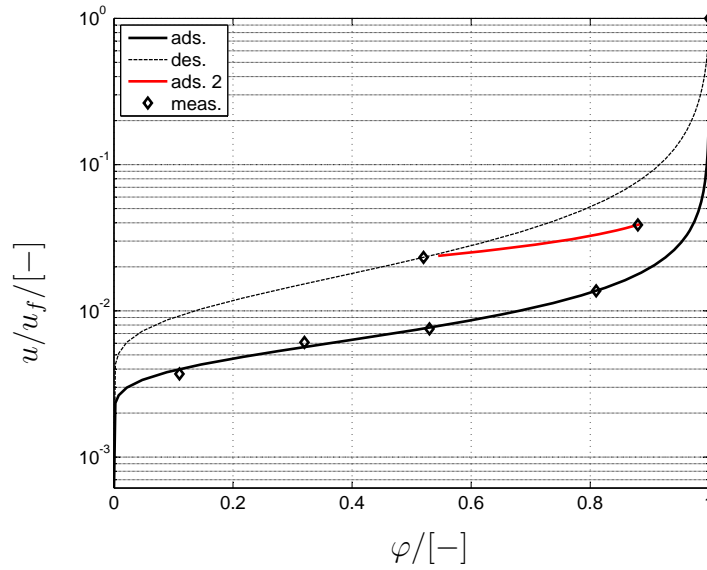
Figure 4.1: Moisture retention curves for adsorption and desorption of calcium silicate determined at 23.5 °C ($u_f = 850 \ kg/m^3$). Measured data interpolated with equation (2.8)
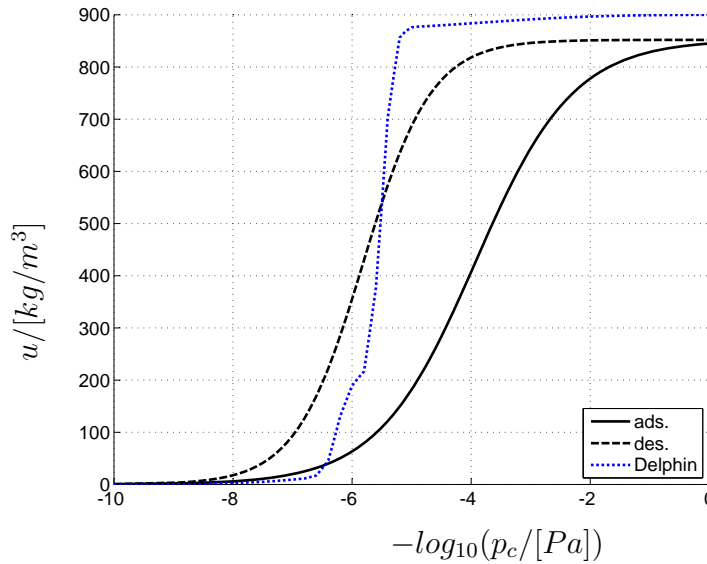

Figure 4.2: Results of the present study determined at 23.5 °C for adsorption and desorption compared with the water retention curve of Delphin 5.6 (a different calcium silicate with $u_f = 900 \ kg/m^3$) [26]

4.4   Isothermal moisture diffusion: cup test

For experimental determination of the moisture transfer coefficient $D_{m,\varphi}$ defined by equation (2.64) and hence of the diffusion resistance coefficient μ, dry and wet cup tests are commonly used. This method is described in detail within the standard EN ISO 12572 [4].

Glass cups are fulfilled with desiccant or with aqueous saturated solutions and closed on the top with the vapor-permeable test specimens as shown in figure 4.3. Afterward, the cups are putted inside a climatic chamber with controlled relative humidity and temperature. The samples prepared with desiccant are called dry cups, the others, containing aqueous salt solution, wet cups. The desiccant and the aqueous salt solution ensure a nearly constant relative humidity value inside the cups. After a certain period of time, constant mass gains (in case of dry cups) or mass losses (in case of wet cup) occur. The mass exchange rate is measured by weighing the cups at defined time intervals. When the steady state is reached, the parameters $D_{m,\varphi}$ and μ can be calculated as described in the following section.
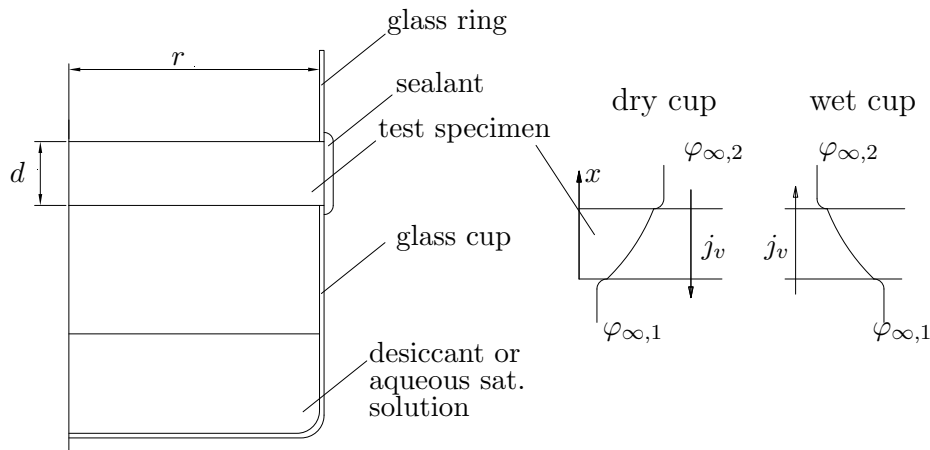
Figure 4.3: Schema of the cup test experiment

4.4.1   Steady-state conditions: determination of the diffusion resistance factor

The vapor flux j_v through the samples is given by equation (2.18). Under isothermal conditions and for the one-dimensional case, the following equation is derived:

$$j_v = -\frac{1}{\mu(\varphi)}\frac{D_v p_s(T)}{R_v T}\frac{\partial \varphi}{\partial x} \tag{4.18}$$

where in general the vapor flux and the relative humidity are functions of position and time: $j_v = j_v(x, t)$, $\varphi = \varphi(x, t)$.

Under steady-state conditions and in the absence of mass sources, j_v is constant. By applying variable separation to equation (4.18), integrating the mass flux between the upper and the lower surface of the specimen, the following expression is obtained:

$$\int_{x_2}^{x_1} j_v dx = -\frac{D_v p_s}{R_v T} \int_{\varphi_{s,2}}^{\varphi_{s,1}} \frac{1}{\mu(\varphi)} d\varphi \qquad (4.19)$$

The term $\frac{D_v p_s}{R_v T}$ can be considered constant under isothermal conditions. Assuming $\mu(\varphi) \approx const$ over the thickness of the specimen and $\varphi(x)$ approximately linear, j_v is given by the following equation:

$$j_v \approx \frac{D_v p_s}{R_D T \mu} \left| \frac{\varphi_{s,2} - \varphi_{s,1}}{x_2 - x_1} \right| \qquad (4.20)$$

the value of μ can be simply calculated from equation (4.21) if the vapor flux j_v is known:

$$\mu = \frac{D_v p_s}{R_D T j_v} \left| \frac{\varphi_{s,2} - \varphi_{s,1}}{x_2 - x_1} \right| \qquad (4.21)$$

This approach is commonly used according to the standard [4]. The experiment can be repeated for different $\varphi_{s,1}$ and $\varphi_{s,2}$ in order to determine a fragmented distribution of $\mu(\varphi_{mean})$ with $\varphi_{mean} = (\varphi_{s,1} + \varphi_{s,2})/2$. However the results obtained in this way are accurate only if $\mu(\varphi) \approx const$, which generally implies a small interval of relative humidity over the specimen $\Delta\varphi = \varphi_{s,1} - \varphi_{s,2}$ (for $\varphi_{s,1} < \varphi < \varphi_{s,2}$).

A different approach proposed in this study consists in solving the integral on the right hand side of equation (4.19) assuming the function $\mu(\varphi)$ given by equation (2.20). Writing (2.20) in (4.19) the following equation is obtained:

$$\int_{x_2}^{x_1} j_v dx = -\frac{D_v p_s}{R_v T \mu_0} \int_{\varphi_{s,2}}^{\varphi_{s,1}} \frac{1}{a\varphi^n + 1} d\varphi \qquad (4.22)$$

solving the integral, equation (4.23) is obtained:

$$j_v = \frac{D_v p_s}{R_v T \mu_0 \Delta x} \left| \frac{a}{n+1}(\varphi_{s,2}^{n+1} - \varphi_{s,1}^{n+1}) + \varphi_{s,2} - \varphi_{s,1} \right| \qquad (4.23)$$

The coefficients μ_0, a and n can be obtained from equation (4.23) by interpolation with measured values of j_v. To this aim, the Matlab-function *fminsearch* is employed. An advantage of the approach proposed here, is that a continuous function $\mu(\varphi)$ can be determined even if few measured data are available.

In order to close the problem, the surface values of relative humidity have to be determined. The standard approach is to assume the surface values equal to the values in the surrounding air ($\varphi_{s,1} \approx \varphi_{1,\infty}$ $\varphi_{s,2} \approx \varphi_{2,\infty}$). However, since we want investigate the impact of the boundary layer resistance on the results, the surface values are here obtained by an iterative procedure, employing equations (4.17)

and (4.23) and assuming natural convection. For determination of the Sherwood number, the correlation (4.6) is used. Note that the mass transfer coefficient β determined in this way represent a lowest theoretical limit, since mixed convection may occur during the experiment.

Measurements have been performed at three different temperature levels as reported in table 4.2.

In figure 4.4 the values measured at $23.5°C$ are reported on the $\varphi_{s,1} - \varphi_{s,2}$ plane, together with the iso-lines at constant j_v defined by equation (4.23). Note that if equation (4.20) instead of equation (4.23) is used, the iso-lines result straight parallel lines.

In figure 4.5 the function $j_v(\varphi_{s,1}, \varphi_{s,2})$ described by equation (4.23) is represented as a 3D-surface.

Figure 4.6 shows a comparison between all the measured flux values and the values calculated with equation (4.23). An acceptable agreement between calculation and measurements is reached.

Figure 4.7 shows the function $\mu(\varphi)$ obtained by interpolation using equation (4.23) and the discrete values of μ calculated according to the standard method with equation (4.21). In both cases the boundary layer resistance is taken into account.

In Figure 4.8 the influence of the mass transfer coefficient β on the measured water vapor diffusion resistance factor is shown.

In Figure 4.9 the function $\mu(\varphi)$ obtained in the present study is compared with data measured in other laboratories [61]. The deviation between the results (in particular for dry-cups tests) indicates that products made by different manufacturer may present significant differences.

The influence of the temperature on the moisture transfer can be observed in figure 4.10. Here the coefficient $D_{m,\varphi}(T,\varphi)$ calculated according to equation (2.64) is reported and compared with the measured values. The values measured at high φ exceed widely the model prediction, indeed, this deviation may have physical explication considering that at high relative humidity the contribution of liquid water diffusivity becomes relevant (see also section 4.6).

4.4.2 Study of the vapor transfer under transient conditions

Since dry and wet cup tests are performed under isothermal conditions and the moisture transfer through the sample can be considered as one-dimensional, the system (2.60) is reduced to the only one-dimensional mass balance as follows:

$$\frac{\partial u}{\partial \varphi}\frac{\partial \varphi}{\partial t} = -\frac{\partial}{\partial x}\left(D_{m,\varphi}\frac{\partial \varphi}{\partial x}\right) \tag{4.24}$$

with boundary conditions given by the following equations:

$$D_{m,\varphi}\frac{\partial \varphi(0,t)}{\partial x} = \beta p_s(\varphi_{\infty,1} - \varphi_{s,1}) \tag{4.25}$$

Table 4.2: Measured values of j_v with 14 mm-thick calcium-silicate specimens

case	$\frac{10^6 \cdot j_v}{[kg/(m^2 s)]}$	$\varphi_{\infty,1}$	$\varphi_{\infty,2}$	$\varphi_{s,1}$	$\varphi_{s,2}$	$\Delta\varphi_\infty$	φ_m	$\frac{10^8 \cdot \beta}{[kg/(m^2 s Pa)]}$	$\frac{\vartheta}{[°C]}$
1	2.42	0.00	0.56	0.04	0.52	0.54	0.28	2.2	23.5
2	1.66	0.31	0.54	0.34	0.51	0.23	0.43	2.1	23.5
3	5.28	0.00	0.88	0.07	0.80	0.86	0.44	2.5	23.5
4	4.78	0.31	0.87	0.38	0.81	0.55	0.59	2.5	23.5
5	3.36	0.94	0.56	0.89	0.61	0.36	0.75	2.4	23.5
6	0.83	0.94	0.88	0.92	0.89	0.04	0.91	1.9	23.5
7	2.62	0.00	0.42	0.07	0.06	0.31	0.21	1.1	30
8	9.44	0.00	0.87	0.38	0.16	0.56	0.44	1.9	30
9	6.15	0.91	0.42	0.89	0.86	0.38	0.67	2.5	30
10	1.70	0.91	0.87	0.92	0.89	0.01	0.89	2.0	30
11	0.44	0.00	0.42	0.03	0.38	0.35	0.38	1.0	15
12	3.65	0.00	0.87	0.17	0.69	0.51	0.69	1.2	15
13	1.46	0.91	0.42	0.87	0.90	0.03	0.89	2.1	15
14	3.53	0.91	0.87	0.96	0.49	0.37	0.68	2.4	15
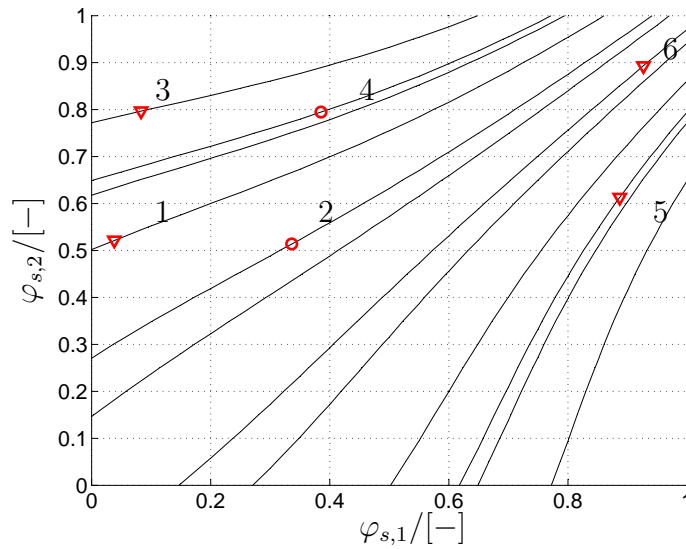
Figure 4.4: Iso-lines presenting constant j_v projected on the $\varphi_{s,1}$ - $\varphi_{s,2}$ plane and values measured at $\vartheta = 23.5°C$ (cases 1-6 in table 4.2)
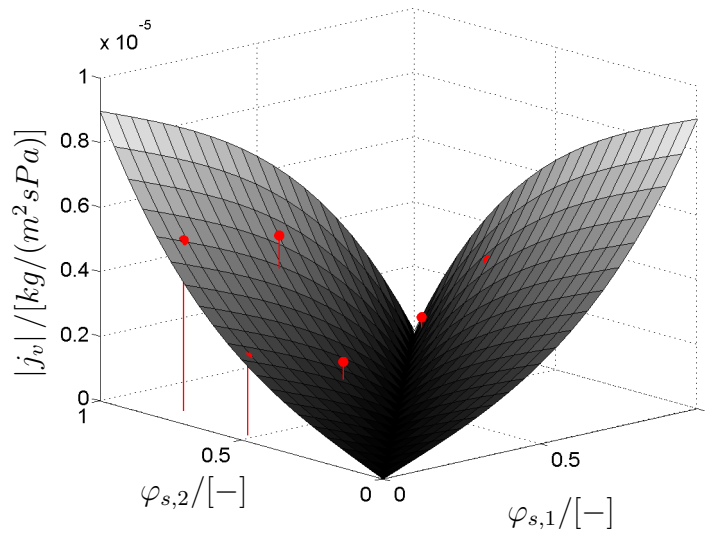
Figure 4.5: j_v as function of $\varphi_{s,1}$ and $\varphi_{s,2}$ and values measured at $\vartheta = 23.5°C$
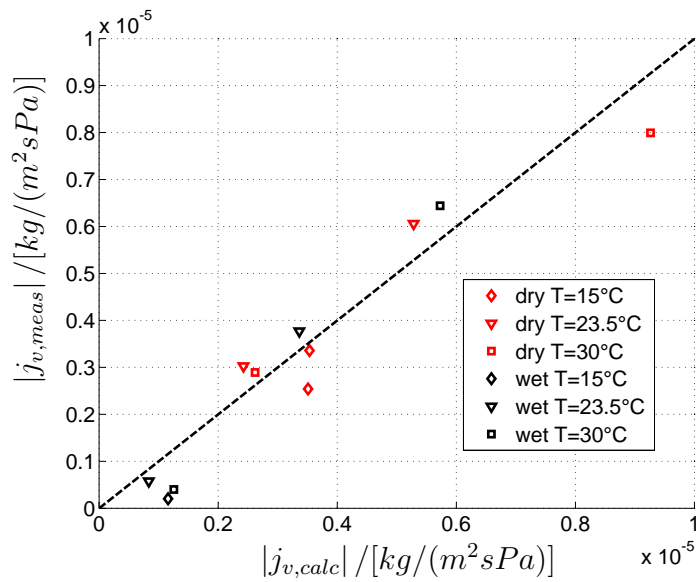
Figure 4.6: Comparison between measured data and results of equation (4.23)
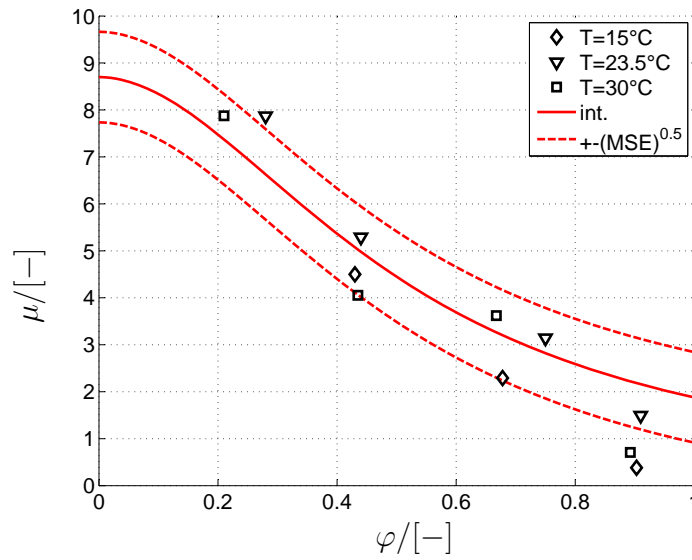
Figure 4.7: Trend of $\mu(\varphi)$ obtained from equation (2.20) with $a = 3.6287$ and $n = 1.9256$; discrete values calculated with equation (4.21); dashed red lines: interval defined by the root of the mean squared error (MSE)
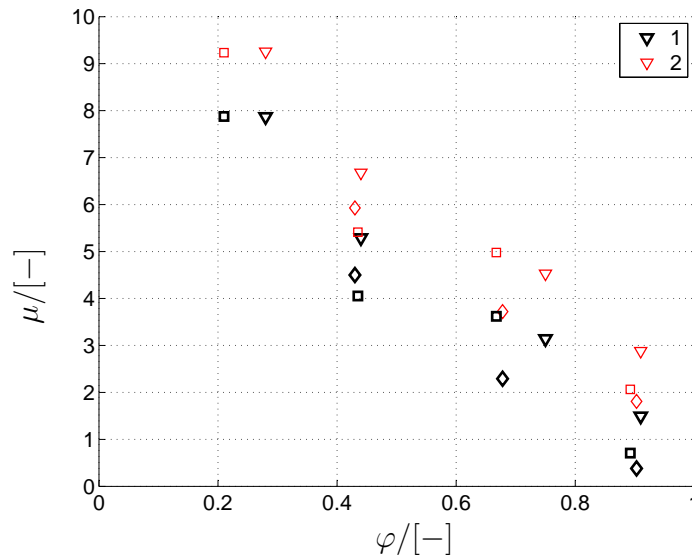
Figure 4.8: Influence of the mass transfer coefficient β on the measured vapor diffusion resistance factor. 1: $\beta = 2 \cdot 10^{-8} \left[\frac{kg}{m^2 sPa}\right]$; 2: $\beta = \infty$
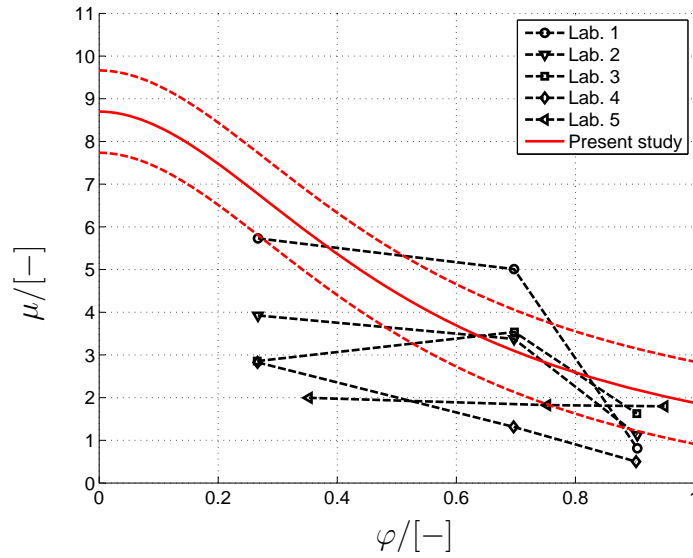
Figure 4.9: Water diffusion resistance factor plotted as a function of relative humidity. Comparison between the present study and data measured by others laboratories reported in [61]
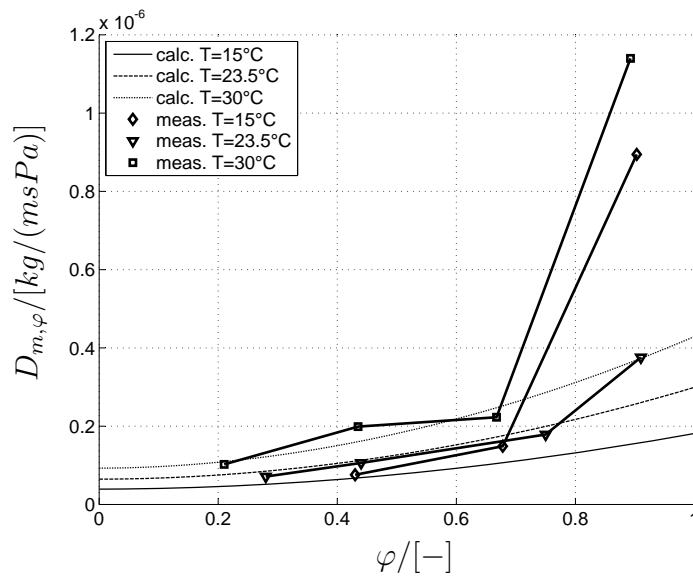
Figure 4.10: $D_{m,\varphi}(\varphi)$ trends according to equations (2.64) and (2.20) without taking into account the contribution of liquid water diffusivity. Discrete values calculated with equations (2.64) and (4.21)

$$D_{m,\varphi}\frac{\partial\varphi(l,t)}{\partial x} = \beta p_s(\varphi_{\infty,2} - \varphi_{s,2}) \qquad (4.26)$$

and with the initial condition given by equation (4.27):

$$\varphi(x,0) = \varphi_i \qquad (4.27)$$

equations (4.24) to (4.27) describe the transient moisture transfer during the cup tests and are solved employing the Matlab function *PDEPE* [66]. The transfer coefficient $D_{m,\varphi}$ is calculated according to equation (2.64) and the relation between water content u and relative humidity φ is given by equation (2.8), characterized in section 4.3.

In figure 4.11 the simulated trend of the mass loss along the time is reported and compared with measured data. This plot shows the transition from boundary conditions of case 6 to those of case 5, described in table 4.2. The vapor flux through the sample is calculated in three different ways:

- $j_{v,1}(t)$ vapor flux at the external surface of the sample calculated according to equation (4.26)

- $j_{v,2}(t)$ vapor flux at the internal surface of the sample calculated according to equation (4.25)

- $j_{v,3}(t)$ vapor flux through the sample calculated according to equation (4.23)

as expected, once steady state conditions are reached, the three fluxes assume the same value $j_{v,1} = j_{v,2} = j_{v,3}$.

4.5   Desorption test

Once the other material properties are known, the liquid water diffusivity $k(T,\varphi)$, described by equation (2.11), can be indirectly determined by means of simple water desorption tests.

The experiment consist in drying material samples, previously doused till the entire pore volume has been filled by liquid water. The drying rate is determined by recording the mass losses during the time. Since the test starts with water-saturated samples, we expect significant contribution of the capillary water transfer with respect to the total moisture transfer inside the samples. The capillary transfer function is determined by means of an inverse approach, searching for the best fitting between simulation and measured data.

To this aim, saturated calcium silicate samples (dimensions: 10 *cm* x 10 *cm* x 3 *cm*) are dried in atmosphere at controlled conditions. The experiment is repeated many times with different ambient temperature and relative humidity.

The numerical simulations are performed with a 3D model implemented with the
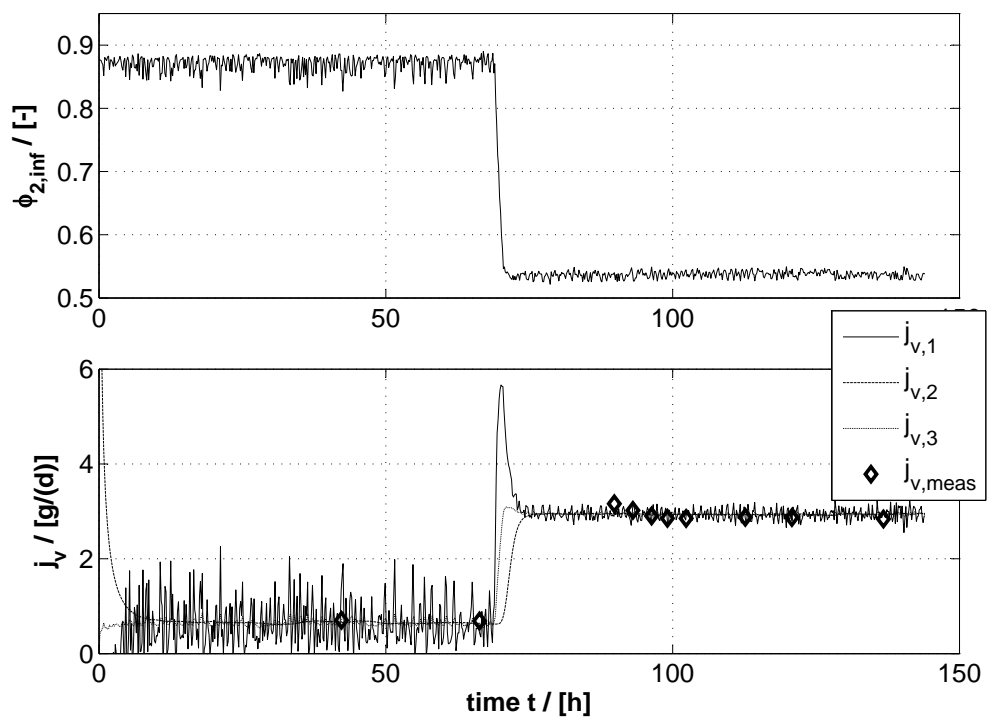
Figure 4.11: Transition from case 6 to case 5 (table 4.2); top: measured external relative humidity; bottom: time trend of the mass flux j_v

software Comsol. Both mass and energy transfer are included, since evaporation cooling has significant influence on the results.

This study can be considered also as a validation test for a 3D numerical model of heat and mass transfer in hygroscopic materials, representing an innovation with respect to the state of the art, since generally the previous works refer to one and two dimensional cases.

The moisture transfer in the samples can be adequately described by means of system (2.60) with boundary and initial conditions given by the following equations:

$$D_{m,T}\nabla T(\mathbf{x},t) + D_{m,\varphi}\nabla\varphi(\mathbf{x},t) =$$
$$\beta\left[p_{s,\infty}\varphi_\infty - p_s(T(\mathbf{x},t))\varphi(\mathbf{x},t)\right] \qquad \mathbf{x}\in\partial\Omega \tag{4.28}$$

$$D_{e,T}\nabla T(\mathbf{x},t) + D_{e,\varphi}\nabla\varphi(\mathbf{x},t) = \alpha\left[T_\infty - T(\mathbf{x},t)\right] +$$
$$h_v\beta\left[p_{s,\infty}\varphi_\infty - p_s(T(\mathbf{x},t))\varphi(\mathbf{x},t)\right] \qquad \mathbf{x}\in\partial\Omega \tag{4.29}$$

$$\varphi(\mathbf{x},0) = \varphi_i \qquad \mathbf{x}\in\Omega \tag{4.30}$$

$$T(\mathbf{x},0) = T_i \qquad \mathbf{x}\in\Omega \tag{4.31}$$

In case of natural convection, the coefficient of heat and mass transfer α and β can be determined employing the empirical functions reported in section 4.2. In case of mixed convection, the transfer coefficients can be derived by inverse procedure, simultaneously with the liquid water diffusivity.

Two phases can be observed during the drying process.

- The first phase is characterized by a constant drying rate. Liquid water is transported by capillary action from the inside to the surface of the sample. The relative humidity at the surface remains nearly constant ($\approx 100\%$). At the same time, due to evaporation cooling, the temperature inside the sample remains some degree under the surrounding air temperature.

- The second phase of the drying process presents reduced capillary water transfer and progressive reduction of the drying rate. The relative humidity at the surface decreases whereas the temperature increases, approximating the surrounding air conditions.

The water content and the drying rate of a sample in atmosphere at $\vartheta_a = 25\,^\circ C$ and relative humidity $\varphi_a = 40\ \%$ are reported in figure (4.12) and (4.13) respectively.

Since the slope of the drying rate depends on the liquid water diffusivity, this parameter can be determined by looking for the value leading to the best agreement between simulation and experimental results. To this aim, the following mean errors for water content and drying rate are defined:

$$err(m_w) = \frac{\sum_{i=1}^{n} \frac{|m_{w,meas} - m_{w,sim}|}{m_{w,meas,max}}}{n} \qquad (4.32)$$

$$err(\dot{m}_w) = \frac{\sum_{i=1}^{n-1} \frac{|\dot{m}_{w,meas} - \dot{m}_{w,sim}|}{\dot{m}_{w,meas,max}}}{n-1} \qquad (4.33)$$

where m_w represents the water content in $[g]$ and $\dot{m}_w = \frac{dm_w}{dt}$ the drying rate in $[g/h]$. The subscripts *meas* and *sim* refer to measured and simulated values respectively, whereas the subscript *max* refers to the maximal value reached during the experiment; n represents the number of measured data. The drying rate is calculated from the measured data for $i = 1$ to $n - 1$ as follows:

$$\dot{m}_{w,meas}^{i} = \left| \frac{m_w^{i+1} - m_w^{i}}{t^{i+1} - t^{i}} \right| \qquad (4.34)$$

Comparing the simulation results with the experimental data, the optimal value of the liquid water diffusivity at saturation is identified (see table 4.3). The iterative procedure for optimization is performed varying the function $\xi(u)$ (equation (2.11)) through the only parameter ξ_1^*. The other function parameters have been kept constant ($\zeta_1 = 1$; $N = 1$).

The experiment has been repeated with different ambient conditions as shown in figure 4.14 and 4.15. It can be observed that the simulation reproduces adequately both the drying phases described above, showing satisfactory agreement with the measured data.

In figure 4.16 the trend of the liquid water diffusivity obtained in this study is compared with the material function reported in the data base of the software Delphin [26]. The deviation between the results may be explained considering that the measured samples came from different manufacturers.

Further testing is performed measuring the surface temperature of the specimens by means of an infrared camera. During the first drying phase, it is some degree lower than the ambient temperature, what can be explained considering the evaporation cooling. In figure 4.17 the measured values of temperature in the center of the specimen are reported. Comparison with simulation results confirm the optimum value of liquid water diffusivity found above. Even if the measured data present some delay with respect to the simulation trend, the general process is adequately reproduced.

It is opportune to consider the effect of the liquid water diffusivity on the temperature distribution. It can be observed that higher liquid water diffusivity leads to faster change of the temperature and to more homogeneous temperature distribution. In other words, in case of higher liquid water diffusivity, reduced temperature difference between corner and center is expected. On the contrary, it has been observed that the dependence of the liquid water diffusivity on the temperature can be neglected within the temperature range characterizing this experiment ($\Delta T < 10K$).

The surface distribution of the temperature can be observed in figure 4.18 where experimental and simulation results at different time steps are reported. Visual

inspection confirms that, despite a delay of the measured data compared to the simulation, the process is reproduced with good agreement.
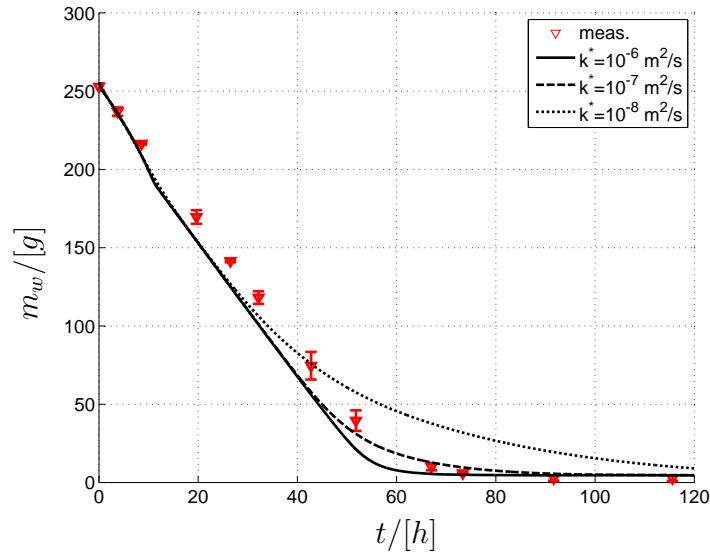
Figure 4.12: Desorption test (sample volume $V = 300\ cm^3$). Comparison between simulated and measured results. Ambient temperature: 25 °C, ambient relative humidity: 40 %
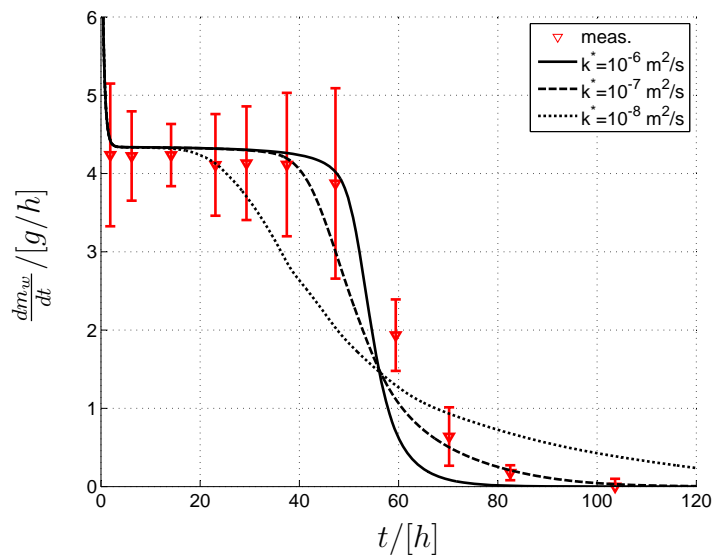
Figure 4.13: Drying rate: comparison between simulated and measured results. Ambient temperature: 25°C, ambient relative humidity: 40%
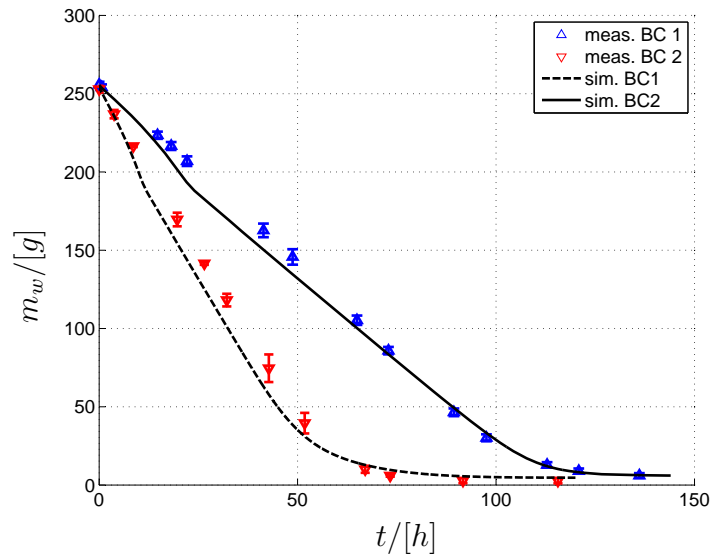
Figure 4.14: Desorption test: comparison between simulated and measured results. Boundary conditions: BC1: temperature: 23.5 $°C$, r. humidity: 52 %; BC2: temperature: 25 $°C$, r. humidity: 40 %
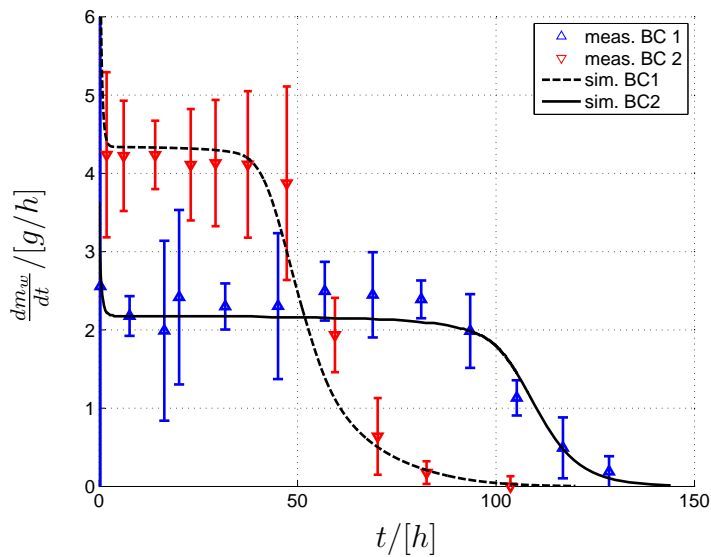
Figure 4.15: Drying rate: comparison between simulated and measured results. Boundary conditions: BC1: temperature: 23.5 $°C$, r. humidity: 52 %; BC2: temperature: 25 $°C$, r. humidity: 40 %
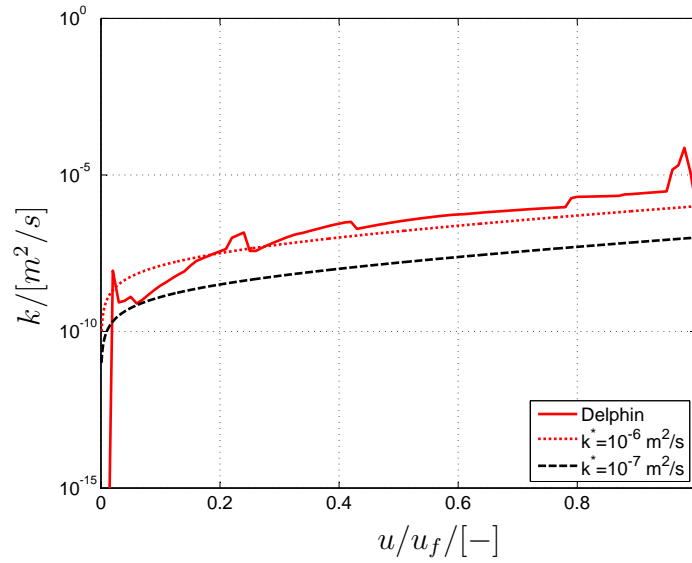
Figure 4.16: Liquid water diffusivity as function of relative water content. Comparison between results of the present study ($k(u = u_f) = 10^{-7}\ m^2/s$) and the function included in the database of Delphin 5.6 [26]
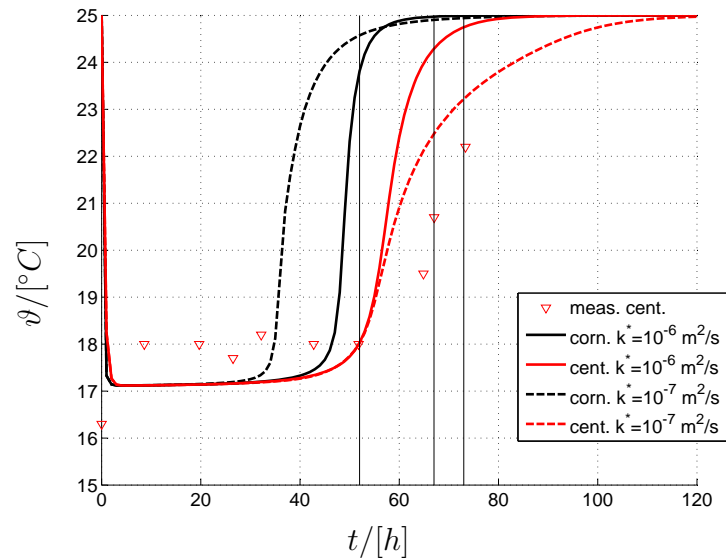
Figure 4.17: Trend of the surface temperature in the center and at the corner of the samples for different liquid water diffusivity. Ambient temperature: 25 $°C$, ambient relative humidity: 40 %

SURFACE TEMPERATURE [$°C$]
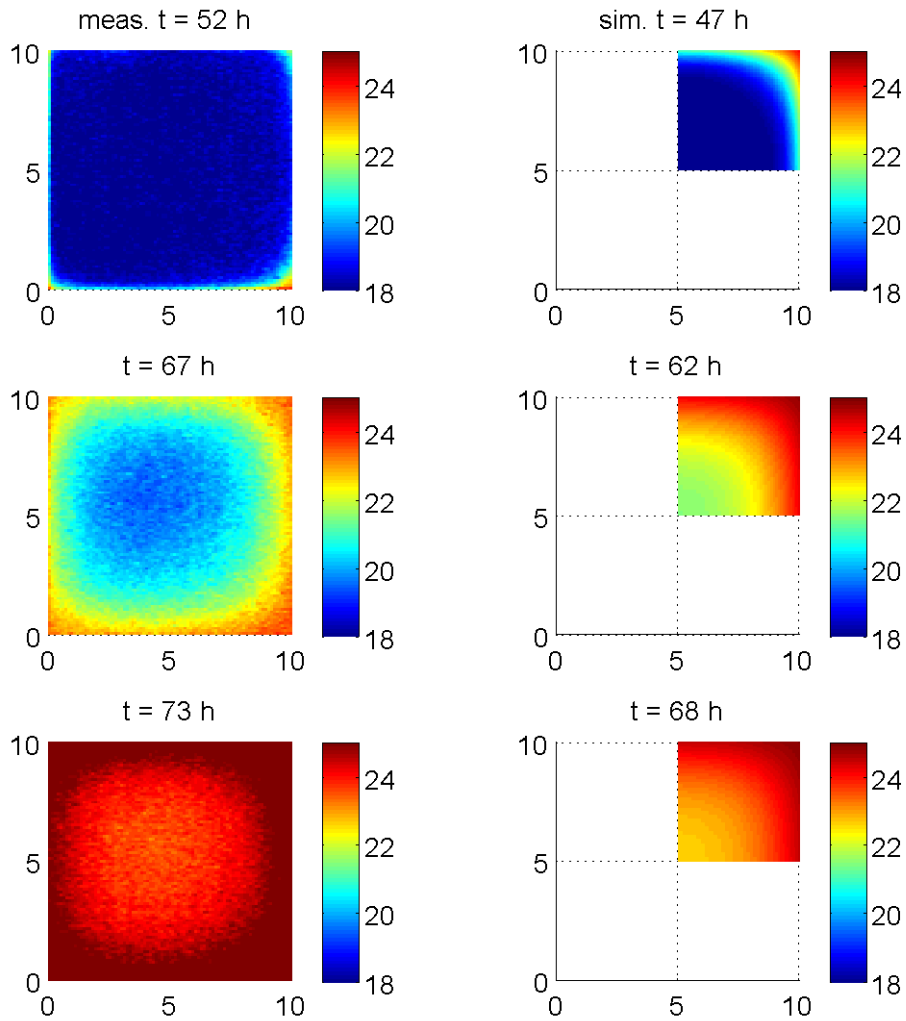
Figure 4.18: Surface temperature distribution at three different time steps. Left: infrared measurement; right: simulation. Ambient conditions: temperature: 25 $°C$, relative humidity: 40 %. Between simulation and measurements can be observed a delay of about 5 h.

Table 4.3: Errors for water content and drying rate calculated according to equations (4.32) and (4.33)

$err(m_w)$ [%]	$err(\dot{m}_w)$ [%]	$k(u = u_f, \xi_1^*)$ [m^2/s]
3.75	6.48	$1 \cdot 10^{-6}$
3.37	5.86	$1 \cdot 10^{-7}$
5.30	12.31	$1 \cdot 10^{-8}$

4.6 Heat flux measurements for determination of the liquid water diffusivity and of the diffusion resistance factor

In this section, heat flux measurements are employed for determination of the liquid water diffusivity. A similar procedure has been already applied to different bulk insulation materials e.g. foam glass gravels for the assessment of diffusion resistance factor by Ochs [51]. Here this technique is improved and adapted for application to capillary active materials such as calcium silicate.

This method is alternative to the one based on desorption tests presented above and can be used for validation of the results previously obtained. The measurements are performed by means of a hot plate apparatus (Taurus instruments TCA 300), according to the standard [3]. A schematic representation of the experimental set up is shown in figure 4.19.

Calcium silicate specimens are firstly doused till the entire pore volume is fully filled by liquid water and afterward partially dried, obtaining the required water content. After this process two specimen overlapped and sealed together are putted inside the hot plate apparatus. Controlled temperature difference is applied between the upper and the lower faces. The heat flux through the specimens is measured at both the cold and hot sides. In order to avoid further loss of mass during the measurement, aluminum foils are applied to the upper and lower faces of the specimens; the border surfaces are sealed using silicon.

All the specimens are composed by two overlying Calcium silicate plates of equal thickness. In this way the water content gradient along the sample axis can be approximately determined by disassembling the specimens after measurement and by weighing separately the upper and the lower part.

During the guarded hot plate experiment, heat and moisture transfer can be assumed as one-dimensional along the sample axis: vapor diffusion occurs from the hot side to the cold side of the specimen, whereas liquid water is transferred due to capillary forces in the opposite direction, except in case of dry or water saturated samples in which no significant mass transfer occurs. Notice that, once steady state conditions are reached, the liquid water flux compensates the vapor flux and the total mass flux becomes at each position equal to zero.

The influence of moisture transfer on total energy transfer can be observed by comparing the measured apparent thermal conductivity of the moist specimens with the values calculated according to the empirical model of Krischer (section 2.3.3) which has to be previously calibrated by measuring the heat flux through dry and water saturated samples in which no significant mass transfer occurs.

Considering that the energy flux associated with macroscopic mass transfer is not included in the model of Krischer, we expect the measured values to overcome the calculated ones. The value of the liquid water diffusivity can be directly derived by writing the energy balance over the specimens at steady state conditions.
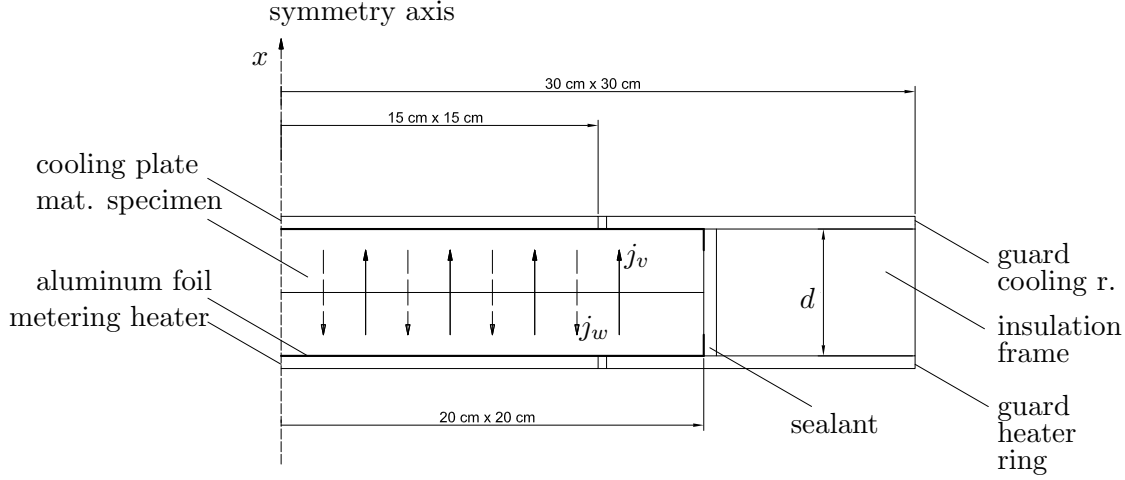
Figure 4.19: Schematic of the hot plate apparatus employed for measurements

4.6.1 Determination of the liquid water diffusivity

At steady state conditions the following system applies at every position along the sample axis:

$$
\begin{cases}
\dot{q}_{meas} = \lambda_{eff}(T,u)\dfrac{\partial T}{\partial x} + h_v(T)j_v(T,u) + h_w(T)j_w(T,u) \\
0 = j_v(T,u) + j_w(T,u)
\end{cases}
\tag{4.35}
$$

where temperature and water content are functions on the position x only: $T = T(x)$ and $u = u(x)$. In equation (4.35) $\dot{q}_{meas}$ represents the measured heat flux. The mass fluxes j_v and j_w and the specific enthalpies of water vapor and of liquid water h_v and h_w are calculated according to equations (2.18), (2.9), (2.59) and (2.41) respectively.
From system (4.35) and equation (2.9) equation (4.36) is derived:

$$
\dot{q}_{meas} = \lambda_{eff}(T,u)\frac{\partial T}{\partial x} + (h_v(T) - h_w(T))\, k\frac{\partial u}{\partial x}
\tag{4.36}
$$

The thermal conductivity λ_{eff} is calculated according to the model of Krischer described by equation (2.27) after previous calibration with data measured at different temperatures using completely dry and completely saturated samples. Via an iterative procedure based on the Matlab function *fminsearch*, best-fitting values for the parameters a, Cs and λ_{fs} are found (figure 4.21). Notice that these parameters are supposed to be constant over the whole moisture and temperature ranges, which is not necessarily the case but represents an acceptable approximation.
Assuming that the temperature and the water content profiles are nearly linear, it is possible to introduce the following approximations:

$$\frac{\partial T}{\partial x} \approx -\frac{\Delta T}{\Delta x} \qquad (4.37)$$

$$\frac{\partial u}{\partial x} \approx \frac{\Delta u}{\Delta x} \qquad (4.38)$$

$$T_m = \frac{T_{hot} + T_{cold}}{2} \qquad (4.39)$$

$$u_m = \frac{u_{hot} + u_{cold}}{2} \approx u(t = 0) \qquad (4.40)$$

where $\Delta T = T_{hot} - T_{cold}$, $\Delta u = u_{cold} - u_{hot}$ and $\Delta x = d$ (specimen thickness); u_{cold} and u_{hot} are obtained by weighing separately the upper and the lower part of the specimens after every measurement.

The measured heat flux $\dot{q}_{meas}$ can be written as a function of the total apparent thermal conductivity λ_{meas} as follows:

$$\dot{q}_{meas} = \lambda_{meas} \frac{\Delta T}{\Delta x} \qquad (4.41)$$

The liquid water diffusivity can be calculated through equation (4.42), which is derived from equation (4.36), employing equation (4.41):

$$k = \frac{(\lambda_{meas} - \lambda_{eff})\Delta T}{(h_v - h_w)\Delta u} \qquad (4.42)$$

All parameters on the right side of equation (4.42) are direct measured or obtained by calculation from measured data as described above.

4.6.2   Influence of the interface resistance

The measured specimens present a discontinuity between the upper and lower parts, which may affect the transfer phenomena. While the effect of this discontinuity on the conductive-radiative heat transfer can be considered as negligible, mass transfer may be significantly influenced as observed by [21]. Due to this fact, the results of the liquid water diffusivity calculated with equation (4.42) may underestimate the real values.

Introducing the interface resistance R_k, the flux of liquid water can be written according to (4.43):

$$j_w = \frac{\Delta u_{int}}{R_k} = \frac{k}{\Delta x + kR_k}\Delta u \qquad (4.43)$$

where Δu_{int} is the discontinuity in the water content profile due to the interface resistance (figure 4.20); thus, equation (4.42) becomes as follows:

$$k = \frac{\frac{(\lambda_{meas} - \lambda_{eff})\Delta T}{(h_v - h_w)\Delta u}}{1 - R_k \frac{(\lambda_{meas} - \lambda_{eff})\Delta T}{(h_v - h_w)\Delta u}} \qquad (4.44)$$

The value of the resistance R_k can be derived by repeating the measurements using monolithic specimens or varying the specimen thickness.
In this study, this effect has been neglected as a first approximation, considering that the specimens have good surface finiteness and are pressed against each other with a force of $400 \ [N]$ during the experiment.
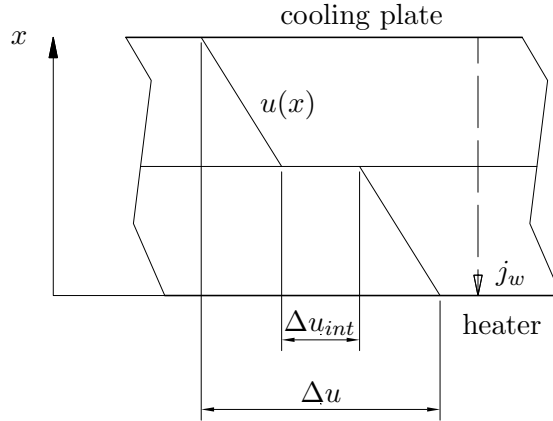
Figure 4.20: Discontinuity in the water content profile due to the interface resistance

4.6.3 Measured results of liquid water diffusivity

In figure 4.22 the measured heat fluxes are reported as function of the water content and of the temperature.
In figure 4.23 the values of the thermal conductivity calculated with the model of Krischer are compared with the measured data: as expected, the measured data overcome the results of the Krischer model unless for completely dry or completely saturated samples. This is due to the fact that in these two limit cases, no mass transfer occurs. For all other cases, the gap between measured values and the empirical model can be quantified as follows:

$$\lambda_{meas} - \lambda_{eff} = \frac{k(h_v - h_w)\Delta u}{\Delta T} \tag{4.45}$$

In figure 4.24 the values of Δu, obtained by weighing the specimens after each measure are shown.
In figure 4.25 the values of liquid water diffusivity calculated with equation (4.42) are interpolated with curves defined by equation (2.11), calibrated with $N = 2$ (four free parameters). The trend of the curves is in accordance with the physical interpretation given in section 2.2.2. The influence of the temperature on the liquid water diffusivity can be observed.
Comparing these results with those previously obtained by means of desorption tests and reported in figure 4.16 an acceptable agreement between the two methods can be observed. However with the heat plate method a better characterization of the liquid conductivity k is obtained.

In figure 4.26 the results of this study are compared with those obtained by other authors employing different techniques ([34] and [15]). Good agreement can be observed in the mid-range of the water content ($0.2 < u/u_f < 0.5$), whereas significant deviations are present at high and at low water contents. This fact can on the one hand be explained due to material differences, on the other hand due to the surface resistance which is not considered within this study (see section 4.6.6).
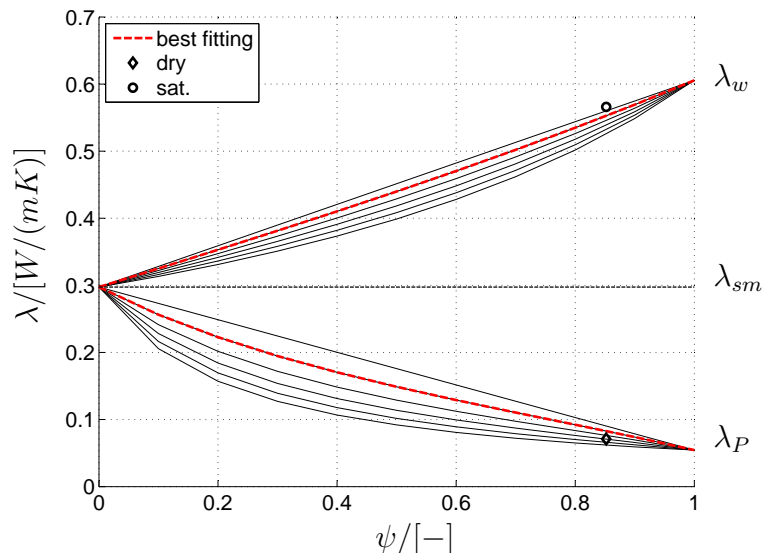
Figure 4.21: Schematic representation for calibration of the model of Krischer using dry and saturated samples ($\vartheta_m = 25°C$). Best fitting parameters: $a = 0.18839$; $\lambda_{sm} = 0.2974[W/(mK)]$. ($Cs = 1.11e - 9[W/(mK^4)]$ previously determined with dry samples)

4.6.4 Determination of the diffusion resistance factor in the super-hygroscopic region

In this section, considerations are made on the physical meaning of the vapor diffusion resistance factor μ appearing in equation (2.15), taking into account the experimental results.

This material property can be considered as a function of the water content. Two opposing phenomena may affect the transfer of vapor: on the one hand, increasing water content leads to reduced space for diffusion of water molecules in the gaseous phase; this fact should produce an enhancement of the vapor diffusion resistance μ as assumed by [34]. On the other hand, thin capillaries filled by liquid water represent shortcuts for vapor diffusion (water island theory, according to [57], cited by [42]). This phenomenon may lead to an effective reduction of μ by increasing the water content.

A quantitative assessment of these two effects is particularly difficult, since liquid water transfer occurs simultaneously with vapor diffusion.
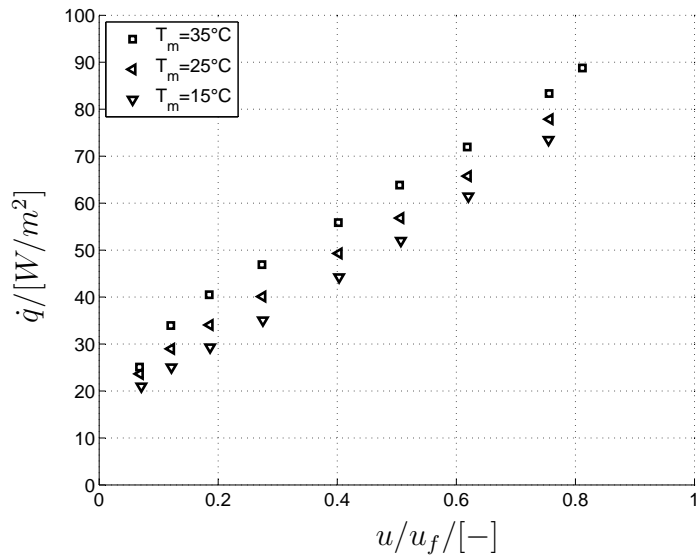
Figure 4.22: Measured heat flux
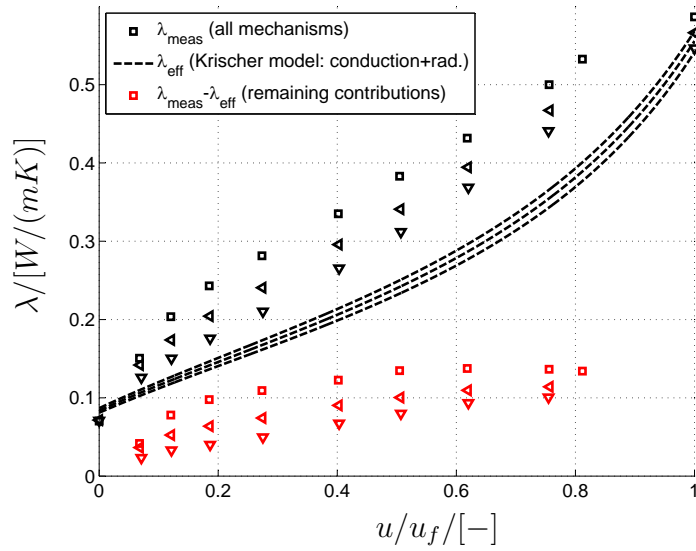
Figure 4.23: Measured apparent thermal conductivity and trends calculated according to the model of Krischer
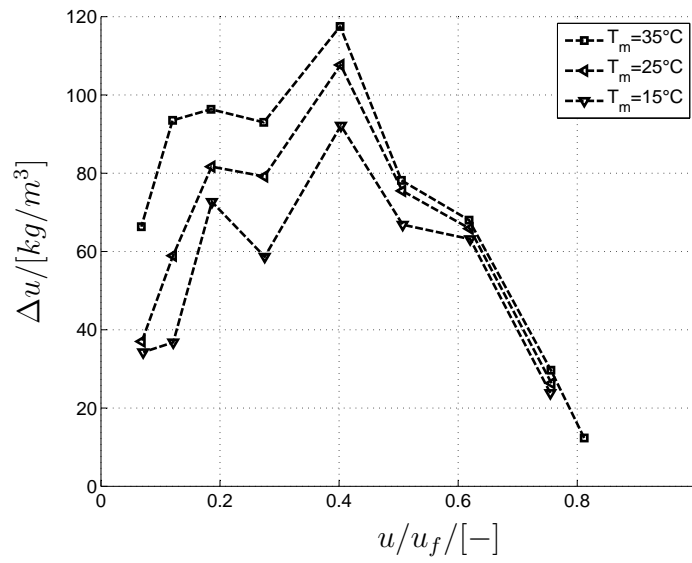
Figure 4.24: Measured apparent $\Delta u = u_{cold} - u_{hot}$
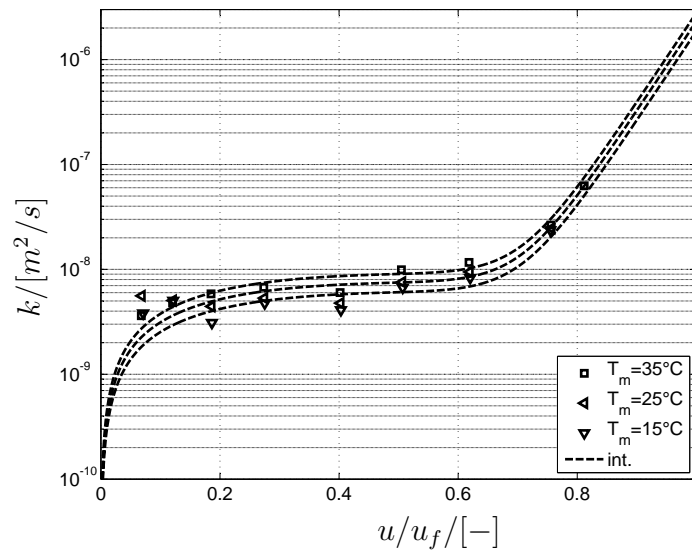
Figure 4.25: Measured values of the liquid water diffusivity obtained by means of the heat plate method and interpolation curves according to equation (2.11) with $N = 2$
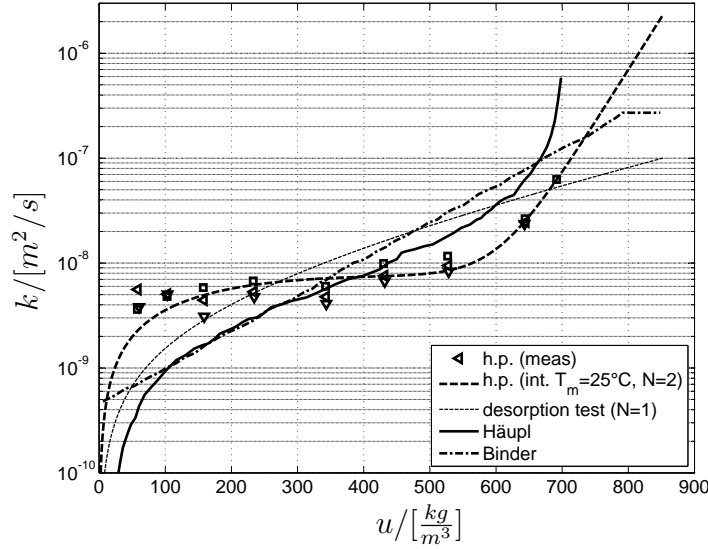
Figure 4.26: Comparison between the values of liquid water diffusivity obtained within this study and the results from other authors ([34] and [15])

Diffusion experiments, performed in hygroscopic range by means of dry and wet cup tests, show that the total water flux increases with increasing of the water content (figure 4.10). Indeed, since in this kind of test vapor diffusion and liquid water fluxes are superimposed, no exact knowledge on the only vapor flux contribution can be obtained.

The heat flux experiment described above gives useful information concerning the diffusion resistance factor in the super-hygroscopic range, since in this test vapor and liquid fluxes are opposing each other.

Equations (2.15) and (2.9) can be written as follows in the one dimensional case:

$$j_v = -\frac{1}{\mu}\frac{D_v}{R_v T}\left(p_s(T)\frac{\partial\varphi}{\partial x} + \varphi\frac{dp_s}{dT}\frac{\partial T}{\partial x}\right) \tag{4.46}$$

$$j_w = -k\frac{\partial u}{\partial x} \tag{4.47}$$

From equations (4.46), (4.47), (4.37), (4.38) and from the second equation of system (4.35), the following expression for the vapor diffusion resistance factor is derived:

$$\mu = \frac{\varphi D_v}{R_v T k}\frac{dp_s}{dT}\frac{\Delta T}{\Delta u} - \frac{D_v p_s(T)}{R_v T k}\frac{\Delta\varphi}{\Delta u} \tag{4.48}$$

We can approximately calculate the value of μ introducing further simplifications, valid in the super-hygroscopic region according to the trend of the water retention curve (figure 4.1):

$$\varphi \approx 1 \tag{4.49}$$

$$\Delta\varphi \approx 0 \tag{4.50}$$

According to the introduced simplifications, it applies:

$$\mu \approx \tilde{\mu} = \frac{D_v}{R_v T k} \frac{dp_s}{dT} \frac{\Delta T}{\Delta u} \tag{4.51}$$

4.6.5   Measured results of diffusion resistance factor

The results calculated with equation (4.51) are reported in figure 4.27.
Notice that even if μ is not a function of the temperature, $\tilde{\mu}$ may depend on it,
however the deviation between values at different temperatures is low.
Moreover, the measurement error may also depend on the temperature, because
of different thermal losses of the heat plate apparatus.
From figure 4.28 it is clear that the vapor diffusion resistance factor still decreases
with the water content within the super-hygroscopic range. This accredits the
hypothesis that capillaries filled by liquid water generate shortcuts for vapor
transfer, reducing the path length that vapor molecules have to pass through.
The diffusion resistance factor of the humid material becomes even lower than
one, and is therefor lower than the resistance produced by an air layer of equal
thickness.
In figure 4.28 the values of $\tilde{\mu}$ obtained by way of heat plate measurements are
compared with the diffusion resistance factor measured by means of cup tests.
It can be observed that the values measured with wet cups are in some cases
even lower than those obtained due to the heat flux experiments. This fact can
be explained considering that, in the case of cup experiments, the contribution
of liquid water transfer is included, leading to underestimation of the diffusion
resistance. This effect can be neglected for dry cups, but becomes relevant in
case of wet cups.

4.6.6   Error estimation

In this section, random and systematic errors affecting the heat plate test are
investigated.
First, we consider the random uncertainty due to limited precision of the employed
instrumentation (digital balance and heat plate apparatus). Since the liquid water
diffusivity is calculated as a function of many measured parameters according to
equation (4.42), the uncertainty of each input parameter influences the overall
uncertainty of the final result.
According to the uncertainty propagation theory, the uncertainty σ_f of a non-
linear differentiable function $f(A, B)$ can be calculated as follows:

$$\sigma_f^2 = \left|\frac{\partial f}{\partial A}\right|^2 \sigma_A^2 + \left|\frac{\partial f}{\partial B}\right|^2 \sigma_B^2 + 2\frac{\partial f}{\partial A}\frac{\partial f}{\partial B}\sigma_{AB} \tag{4.52}$$

where A and B are the input variables, assumed as exactly known constants,
σ_A and σ_B the uncertainties of the input variables, and σ_{AB} the covariance.
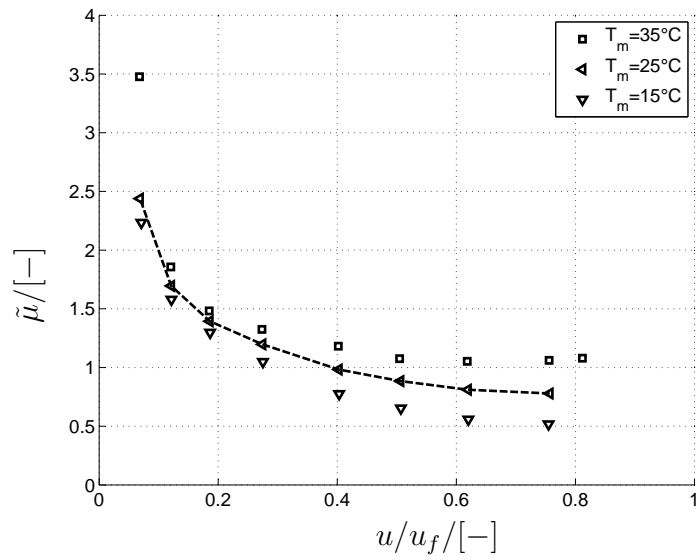
Figure 4.27: Factor $\tilde{\mu}$ versus water content u/u_f
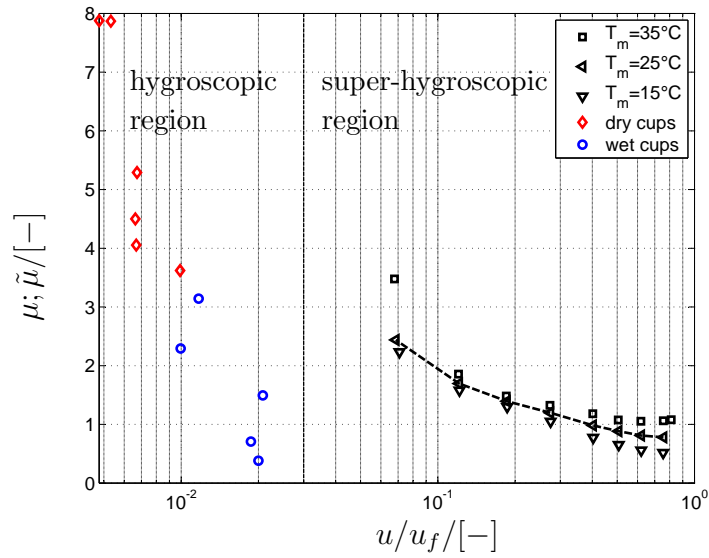
Figure 4.28: Comparison between the parameter $\tilde{\mu}$ and the diffusion resistance factor μ determined by cup tests (section 4.4.1)

Considering equation (4.42) and assuming independent input variables (covariance equal to zero), the uncertainty of the liquid water diffusivity σ_k is calculated:

$$\left(\frac{\sigma_k}{k}\right)^2 = \left(\frac{\sigma_{\lambda_{meas}} + \sigma_{\lambda_{eff}}}{\lambda_{meas} - \lambda_{eff}}\right)^2 + \left(\frac{\sigma_{T_{hot}} + \sigma_{T_{cold}}}{T_{hot} - T_{cold}}\right)^2 + \\ \left(\frac{\sigma_{h_v} + \sigma_{h_w}}{h_v - h_w}\right)^2 + \left(\frac{\sigma_{u_{hot}} + \sigma_{u_{cold}}}{u_{cold} - u_{hot}}\right)^2 \tag{4.53}$$

where the water content difference $(u_{cold} - u_{hot})$ is given by the following equation:

$$u_{cold} - u_{hot} = 2\left(u_2 - u_1\right) \tag{4.54}$$

with:

$$u_1 = \frac{M_{wet,hot} - M_{dry,hot}}{V} \tag{4.55}$$

$$u_2 = \frac{M_{wet,cold} - M_{dry,cold}}{V} \tag{4.56}$$

being u_1 and u_2 the mean water contents of hot and cold samples, M_{wet} and M_{dry} the masses of wet and dry samples, and V the sample volume.
In the same way, the uncertainty $\sigma_{\tilde{\mu}}$ affecting the parameter $\tilde{\mu}$ is calculated from equation (4.51), :

$$\left(\frac{\sigma_{\tilde{\mu}}}{\tilde{\mu}}\right)^2 = \left(\frac{\sigma_k}{k}\right)^2 + \left(\frac{\sigma_{u_{hot}} + \sigma_{u_{cold}}}{u_{cold} - u_{hot}}\right)^2 \tag{4.57}$$

where the uncertainty on the temperature has been considered as negligible, compared to other terms.
According to the instrumentation data sheets, the balance has a repeatability of ± 0.01 [g] while the measured thermal conductivity presents an uncertainty of max. ± 3 %.
Some difficulties occur by estimating the uncertainty of λ_{eff}, since this value is not directly measured, but obtained through calibration of a complex empirical model. We assume as a first approximation $\sigma_{\lambda_{eff}} = 10$ %, considering this as a rather conservative value ([41] pag. 275-276). For a further improvement of the accuracy, more advanced models may be used (e.g. [74], [62]): investigation on this point is required and will be object of future work.
The assumed uncertainties of the input parameters are reported in table 4.4, while in table 4.5 the values of the input parameters, of the liquid water diffusivity and of the parameter $\tilde{\mu}$ are reported with their estimated uncertainties.
Figure 4.29 shows the uncertainty intervals of the liquid water diffusivity tanking values measured at 35 °C as an example; similarly, in figure 4.30 the uncertainty intervals estimated for the parameter $\tilde{\mu}$ are reported. Note that these results don´t take into account the systematic errors that may affect the experiment, such as the interface resistance R_k described in section 4.6.2.

In order to quantify the impact of this parameter on the final results, the calculation has been repeated assuming different values of the interface resistance (hence different discontinuities of the water content profile Δu_{int}). The results of this analysis are shown in figure 4.31, taking again the liquid water diffusivity at 35 $°C$ as an example.

This plot confirms that an accurate determination of the interface resistance is required.

Table 4.4: Assumed uncertainties on the input parameters due to limited precision of the employed instrumentation

Parameter	Dimension	Uncertainty	Dimension
λ_{meas}	$[W/(mK)]$	3	$[\%]$
λ_{eff}	$[W/(mK)]$	10	$[\%]$
u_{hot}	$[kg/m^3]$	33.3	$[g/m^3]$
u_{cold}	$[kg/m^3]$	33.3	$[g/m^3]$
T_{hot}	$[K]$	0.1	$[K]$
T_{cold}	$[K]$	0.1	$[K]$

Table 4.5: Input parameters and results of k and $\tilde{\mu}$. The uncertainties have been estimated assuming the values reported in table 4.4

λ_{mea} $[\frac{W}{mK}]$	$\sigma_{\lambda_{meas}}$ $[\frac{W}{mk}]$	λ_{eff} $[\frac{W}{mK}]$	$\sigma_{\lambda_{eff}}$ $[\frac{W}{mK}]$	u_1 $[\frac{kg}{m^3}]$	u_2 $[\frac{kg}{m^3}]$	ϑ_{hot} $[°C]$	ϑ_{cold} $[°C]$	k $[\frac{m^2}{s}]$	σ_k $[\frac{m^2}{s}]$	$\tilde{\mu}$ $[-]$	$\sigma_{\tilde{\mu}}$ $[-]$
0.53	0.016	0.40	0.040	689	695	40	30	4.5e-8	1.9e-8	1.1	0.5
0.44	0.013	0.34	0.034	637	649	20	10	1.7e-8	0.8e-8	0.5	0.2
0.47	0.014	0.35	0.035	638	652	30	20	1.8e-8	0.8e-8	0.8	0.3
0.50	0.015	0.36	0.036	637	651	40	30	1.9e-8	0.7e-8	1.1	0.4
0.37	0.011	0.28	0.028	513	544	20	10	0.6e-8	0.2e-8	0.6	0.2
0.39	0.012	0.29	0.029	511	544	30	20	0.7e-8	0.3e-8	0.8	0.3
0.43	0.013	0.29	0.029	510	544	40	30	0.8e-8	0.3e-8	1.1	0.3
0.31	0.009	0.23	0.023	415	449	20	10	0.5e-8	0.2e-8	0.7	0.3
0.34	0.010	0.24	0.024	412	450	30	20	0.5e-8	0.2e-8	0.9	0.3
0.38	0.011	0.25	0.025	411	450	40	30	0.7e-8	0.2e-8	1.1	0.3
0.27	0.008	0.20	0.020	320	367	20	10	0.3e-8	0.1e-8	0.8	0.3
0.30	0.009	0.21	0.021	316	370	30	20	0.3e-8	0.1e-8	1.0	0.3
0.34	0.010	0.21	0.021	313	372	40	30	0.4e-8	0.1e-8	1.2	0.3
0.21	0.006	0.16	0.016	220	249	20	10	0.3e-8	0.2e-8	1.0	0.5
0.24	0.007	0.17	0.017	214	254	30	20	0.4e-8	0.1e-8	1.2	0.4
0.28	0.008	0.17	0.017	210	256	40	30	0.5e-8	0.1e-8	1.3	0.3
0.18	0.005	0.14	0.014	141	177	20	10	0.2e-8	0.1e-8	1.3	0.6
0.20	0.006	0.14	0.014	138	179	30	20	0.3e-8	0.1e-8	1.4	0.4
0.24	0.007	0.15	0.015	133	182	40	30	0.4e-8	0.1e-8	1.5	0.3
0.15	0.005	0.12	0.012	94	113	20	10	0.4e-8	0.2e-8	1.6	0.8
0.17	0.005	0.12	0.012	88	118	30	20	0.4e-8	0.1e-8	1.7	0.6
0.20	0.006	0.13	0.013	79	126	40	30	0.3e-8	0.1e-8	1.9	0.4
0.13	0.004	0.10	0.010	52	69	20	10	0.3e-8	0.2e-8	2.2	1.3
0.14	0.004	0.11	0.011	49	68	30	20	0.4e-8	0.2e-8	2.4	1.0
0.15	0.005	0.11	0.011	41	74	40	30	0.3e-8	0.1e-8	3.5	1.3
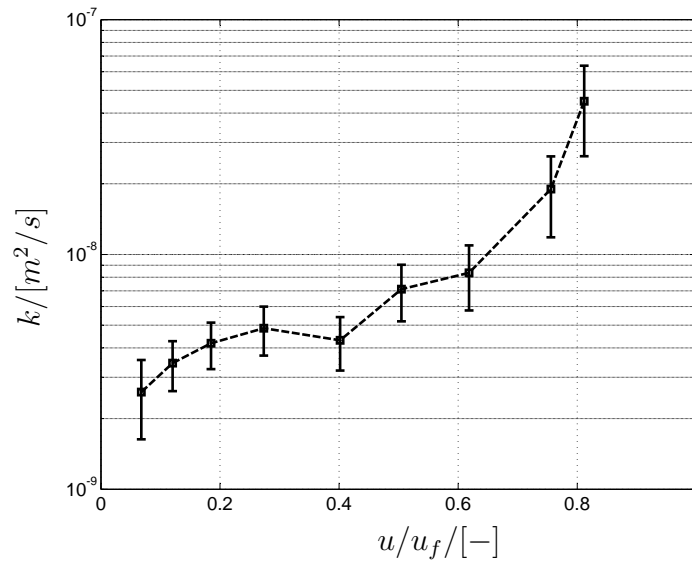
Figure 4.29: Uncertainty affecting the measured liquid water diffusivity calculated according to the input values reported in table 4.4 ($\vartheta_m = 35$ °C)
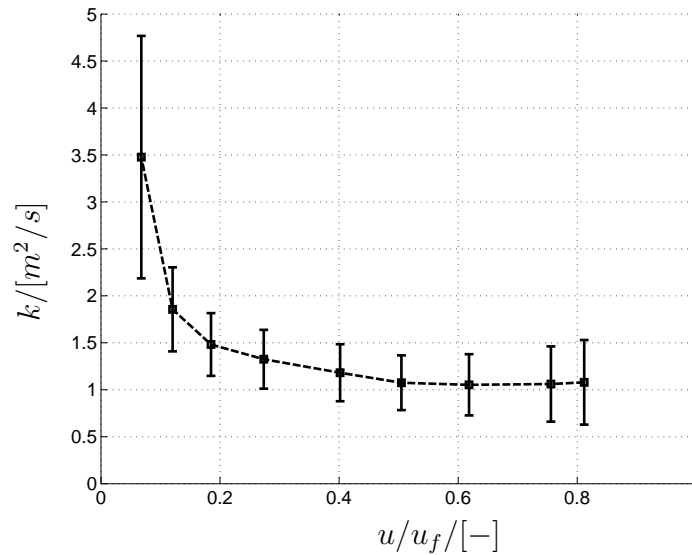
Figure 4.30: Uncertainty affecting $\tilde{\mu}$ calculated according to the input values reported in table 4.4 ($\vartheta_m = 35$ °C)
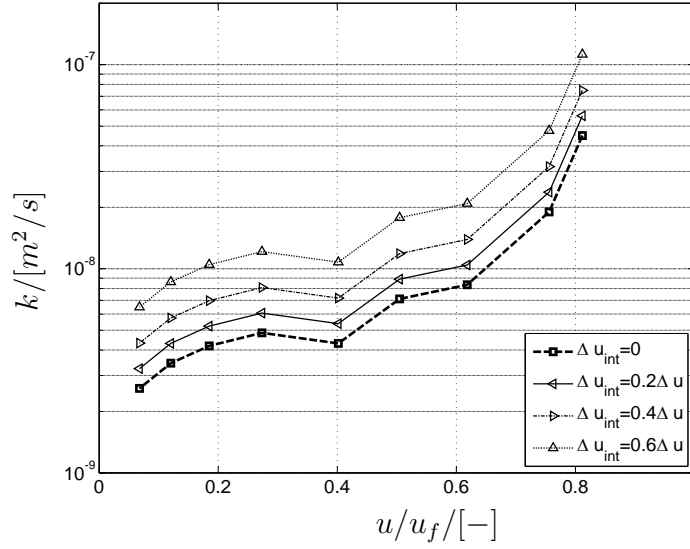
Figure 4.31: Influence of the interface resistance on the measured liquid water diffusivity ($\vartheta_m = 35\ °C$)

4.6.7 Study of the transient period

The results obtained with the heat plate experiment can be used also for validation of the model reported in section 2.6.

The time-dependent heat and moisture transfer trough the sample is described by system (2.60), which for the one dimensional case and assuming $\frac{\partial u}{\partial T}\frac{\partial T}{\partial t} \approx 0$ can be written as follows:

$$\begin{cases} \dfrac{\partial H}{\partial \varphi}\dfrac{\partial \varphi}{\partial t} + \dfrac{\partial H}{\partial T}\dfrac{\partial T}{\partial t} = -\dfrac{\partial}{\partial x}\left(D_{e,T}\dfrac{\partial T}{\partial x} + D_{e,\varphi}\dfrac{\partial \varphi}{\partial x}\right) \\[2mm] \dfrac{\partial u}{\partial \varphi}\dfrac{\partial \varphi}{\partial t} = -\dfrac{\partial}{\partial x}\left(D_{m,T}\dfrac{\partial T}{\partial x} + D_{m,\varphi}\dfrac{\partial \varphi}{\partial x}\right) \end{cases} \tag{4.58}$$

with the following boundary conditions at the cold plate ($x = 0$) and at the hot plate ($x = d$):

$$T(0,t) = T_C(t) \tag{4.59}$$

$$j_v(0,t) + j_w(0,t) = D_{m,T}\frac{\partial T(0,t)}{\partial x} + D_{m,\varphi}\frac{\partial \varphi(0,t)}{\partial x} = 0 \tag{4.60}$$

$$T(d,t) = T_W(t) \tag{4.61}$$

$$j_v(d,t) + j_w(d,t) = D_{m,T}\frac{\partial T(d,t)}{\partial x} + D_{m,\varphi}\frac{\partial \varphi(d,t)}{\partial x} = 0 \tag{4.62}$$

The assumed initial conditions are:

$$T(x, 0) = T_i \tag{4.63}$$

$$\varphi(x, 0) = \varphi_i \tag{4.64}$$

The following results refer to a sample presenting water content $u = 0.52\ u_f$ and mean temperature $\vartheta_{mean} = 15°C$, taken as an example. Similar considerations can be done for the other cases.

In figure 4.32 a), the time trends of energy fluxes measured and simulated at the cooling and heating plate are reported; whereas in figure 4.32 b) the total simulated energy flux is represented as sum of the conductive/radiative contribution (dashed line), and of the enthalpy flux contribution (pointed line).

The energy fluxes reach steady state conditions after approximately 5 hours, however, to obtain equilibrium of moisture distribution, a longer period of time is needed; this can be observed in figure 4.33 a) where the water content profiles are reported. A time period of approximately $48h$ is needed for complete achievement of the steady state, however the employed measuring time $(24h)$ can be considered as acceptable.

Consider also that some uncertainty is introduced in the time-dependent model, due to the fact that no exact trend of the storage term $\frac{\partial u}{\partial \varphi}$ in the super-hygroscopic region is known. For more exhaustive evaluation concerning the minimum time needed for the steady state, Δu has to be measured at different time steps during the experiment. This analysis has to be performed within further improvement of this work.

As shown in figure 4.33 b), the temperature distribution reaches the steady state after few hours; much earlier than the moisture distribution. Notice that the assumption of quasi-linear temperature and water content profiles introduced in section 4.6.1 seems to be a good approximation of the steady state conditions.

In figure 4.33 c), d) and e) the liquid water flux (j_w), the vapor flux $(-j_v)$ and total mass flux $(j_v + j_w)$ inside the specimen are reported at different time steps. In figure 4.33 f) the thermal conductivity, calculated according to the model of Krischer, is shown. It can be observed that this parameter does not present large variations inside the specimen for the considered conditions.
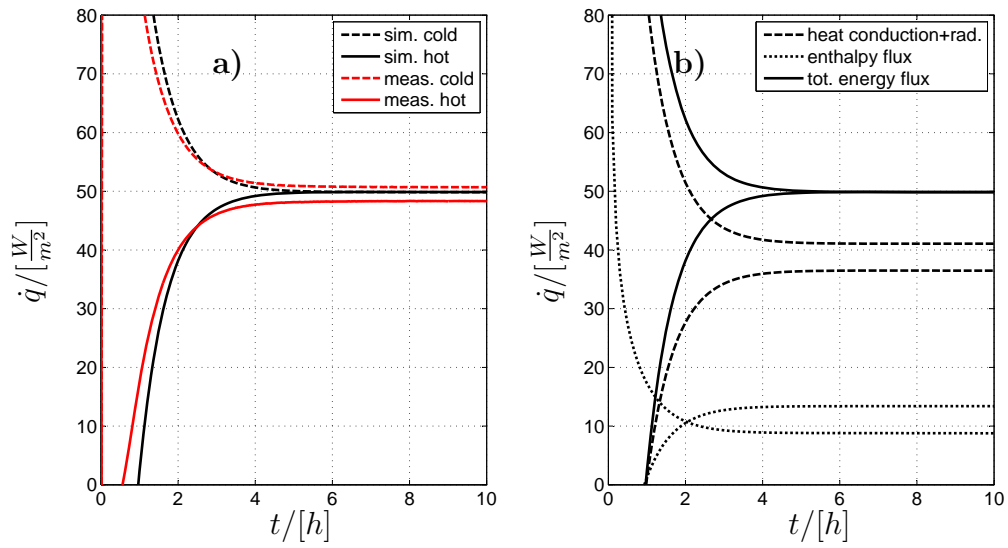
Figure 4.32: Measured and simulated energy fluxes referring to a sample with $\frac{u}{u_f} = 0.52$ and $\vartheta_m = 15\ ^\circ C$ (a). Total simulated energy flux given by the conductive and radiative contributions added to the enthalpy flux (b)
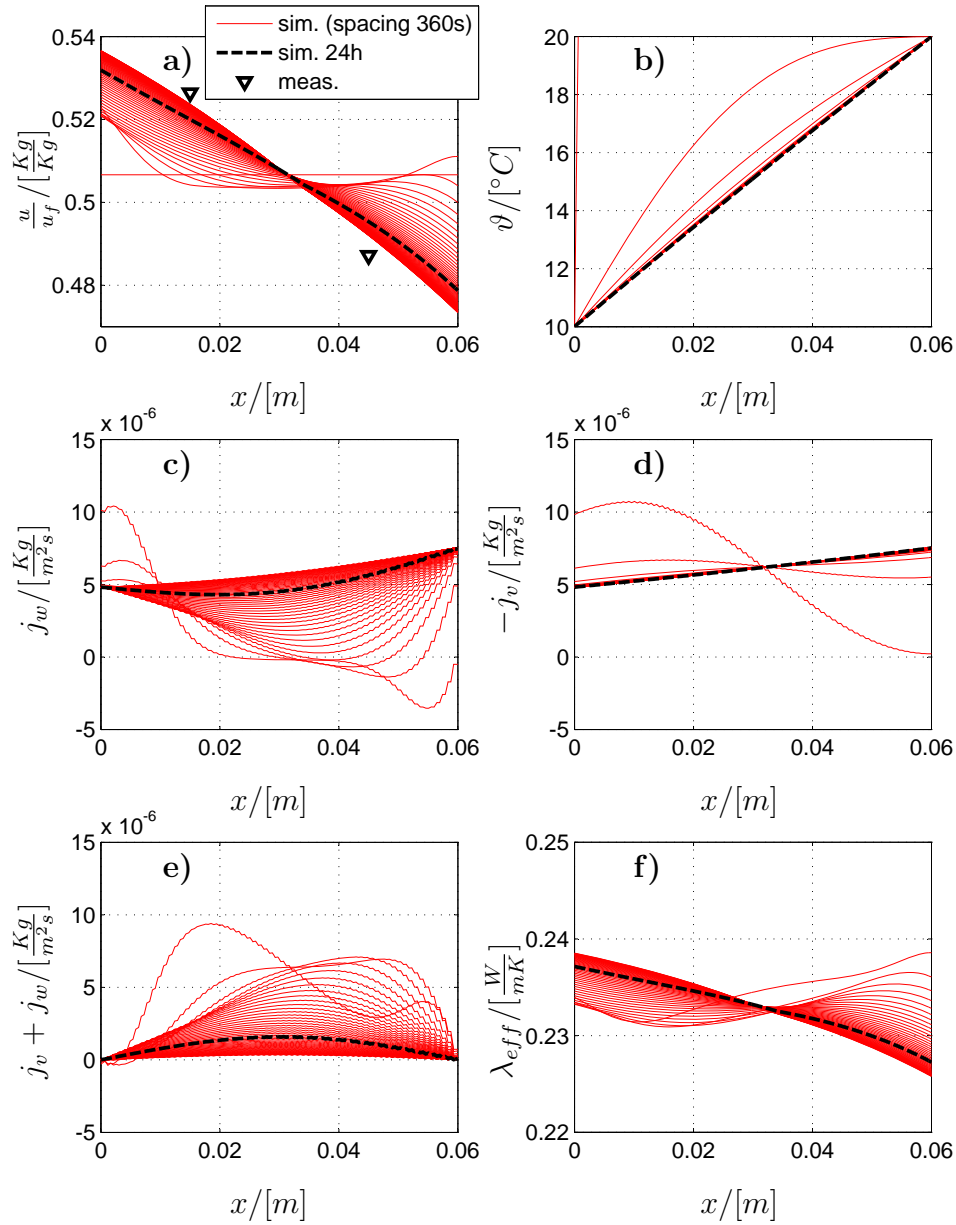
Figure 4.33: Profiles of: a) water content, b) temperature, c) liquid water flux, d) vapor flux, e) total moisture flux, f) thermal conductivity over the specimen thickness. Exemplary case: $\frac{u}{u_f} = 0.52$ and $\vartheta_{mean} = 15°C$

Chapter 5

Solutions for practical building physics problems

The last part of this thesis aims to study the hygrothermal behavior of various construction components of practical interest for building physics. Avoiding a detailed description of well-standardized solutions for the building envelope, we focus on options which still present a challenge from the technical point of view (e.g. walls with applied internal insulation and timber beam ends embedded in intern insulated masonry walls).

Internal insulation systems are analyzed by means of numerical simulations and employing analytical models (section 5.2).

In section 5.3 the focus lies on moisture risk assessment at timber beam ends.

On the one hand, the interaction between building components and air cavities or gaps, in which forced convection occurs, is taken into consideration; yet other cases presenting 3D-geometries are analyzed. Such complex situations have been rarely investigated till now in the literature.

Simulation models on different levels of complexity are developed, by implementing the equation system introduced in section 2 with Comsol.

The results of this chapter have been in part already published in [12], [13] and [11].

5.1 Moisture sources affecting the building envelope

According to [28], the following moisture sources may affect an external building wall exposed to environmental conditions:

1. *Initial material moisture, introduced during the edification of the building.* In order to prevent moisture damages, it is recommended to reduce as far as possible the initial moisture rate e.g. through adequate material stocking and planning proper drying periods during the edification phase.

2. *Moisture rising from the ground due to capillary action.* This problem is particularly common in historical or old buildings, which have no moisture

barrier in the foundations. Several alternatives for the retrofit are available (e.g. injection methods [56] or anti damp preservation [76]).

3. *Driving rain on the building facade.* An adequate roof overhang may be useful as rain protection. In case of retrofit of the building, the application of hydrophobic, diffusion-open exterior plasters is recommended, since this reduces the absorbed moisture through the external wall [56].

4. *Moisture infiltration due to convection through air leakages in the construction.* To reduce this moisture source, air leakages through the Building envelope have to be carefully avoided. This transfer mechanism is investigated in section 5.3.

5. *Water vapor diffusion from the internal environment.* This process may become particularly important in case internal insulation is applied, and is described in detail in section 5.2.

Moisture transfer due to convection and diffusion (point 4 and 5) is investigated within the following sections, while driving rain and the other sources described above do not represent the object of this study. For solutions concerning these phenomena, we refer to the work of other authors.

5.2 Internal insulation systems

In case internal insulation is applied e.g. vapor diffusion from the inside of the building may lead to high values of moisture content behind the insulation and even to water condensation and subsequent damage of components made of organic materials (e.g. timber beams).
Two solutions are possible for avoiding this moisture risk.
The standard solution consists in applying a vapor retarder on the internal side of the insulation, avoiding incoming of moisture due to diffusion. This procedure is challenging, since in practice some diligence is needed to avoid gaps in the vapor tight layer (see [28] for how this challenge can be mastered).
A different way to handle this task is to employ capillary active materials as thermal insulation (e.g. cellulose or calcium silicate). In this case the insulation remains vapor open, but it can dry out from the internal side due to capillary action. In fact, during the heating period, vapor diffusion and liquid water transfer occur in opposite directions inside the insulation, keeping the water content under a critical level. This kind of solution is in general more expensive than the traditional one, realized with a vapor retarder.
A prerequisite for correct planning of internal insulation systems is a deep knowledge of vapor and liquid water transfer in the employed materials: in other words, a method for the correct prediction of moisture level inside the construction as a function of material properties and boundary conditions is needed. To this aim, numerical and analytical solutions have been already proposed by numerous authors.

An analytical method commonly used for prediction of water condensation inside the wall is the so called Glaser method, standardized in [2]. However, this method is not adequate in case liquid water transfer occurs. Hence, it can not be applied e.g. to constructions with capillary-active internal insulation, which represent one of the topics of this work.

In order to overcome the limits of the Glaser method, Häupl proposed an analytical method, including liquid water redistribution, which has been implemented in the software COND [25]. Moreover, numerous software based on numerical solutions of the driving equations reported in section 2, are now available on the market. This kind of software may be useful for evaluation of the moisture risk inside the wall (e.g. [26]).

The numerical approach is the most accurate one, but also requires the knowledge of a large amount of parameters (material functions, climate data ecc.), presents high programming effort and may be very time-consuming for the user. Analytical solutions are necessarily more approximated but admit better overview on the input parameters and a simple implementation.

In the following section we introduce a simple analytical method, specific for evaluation of capillary active internal insulation system and alternative to the one developed by Häupl. Due to the introduced simplifications, the proposed method applies just for specific cases (reduced moisture transfer from/to the external side, no vapor retarder on the internal side).

In order to test the method, we consider the simplified wall model represented in figure 5.1, comparing the results with those obtained by the standard Glaser method and by numerical simulation in winter conditions.
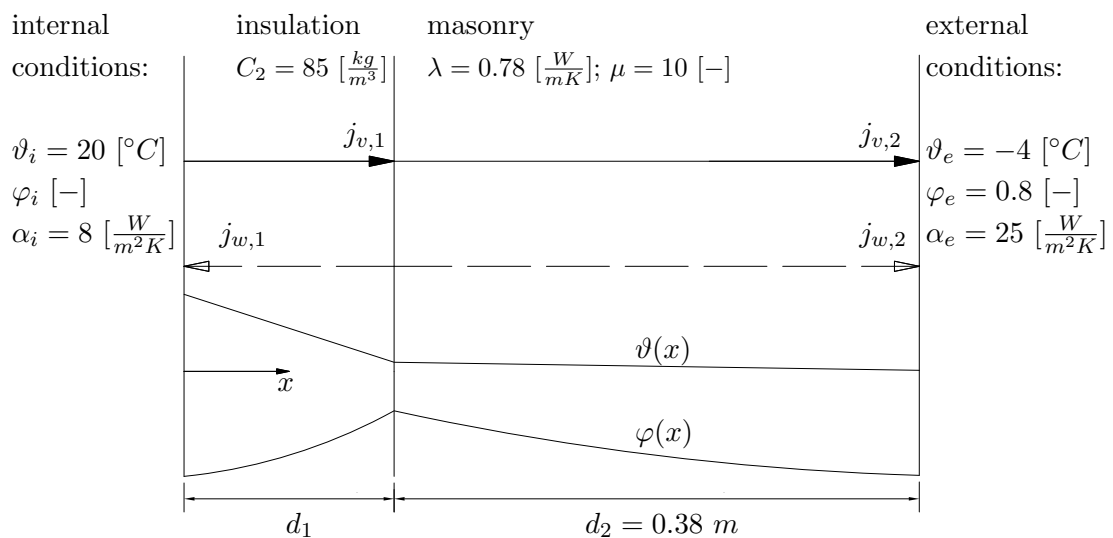
Figure 5.1: Schematic representation of a wall with applied internal insulation for typical winter conditions $(\vartheta_e < \vartheta_i)$

5.2.1 Analytical method for evaluation of moisture level behind capillary active internal insulation

Our aim is to derive the relative humidity $(\varphi_{1,2})$ and the temperature $(T_{1,2})$ behind the insulation, expressed as functions of constant boundary conditions, material parameters and geometry.

Considering the plot in figure 5.1, the mass balance at the interface between insulation and masonry at steady state conditions can be written as follows:

$$j_{v,1} - j_{w,1} = j_{v,2} + j_{w,2} \tag{5.1}$$

Assuming the mass fluxes through the masonry as negligible compared to the other terms, we obtain the following equation:

$$j_{v,1} = j_{w,1} \tag{5.2}$$

this simplification is allowed if the masonry presents higher diffusion resistance and lower liquid water diffusivity than those of the internal insulation, and if the temperature difference over the insulation is much higher than the one over the masonry.

The flux of vapor and liquid water through the insulation layer, are approximately expressed through equations (5.3) and (5.4):

$$j_{v,1} = \frac{D_v}{R_v \bar{T} \mu} \left(\bar{p}_s \frac{\varphi_{s,i} - \varphi_{1,2}}{\Delta x} + \bar{\varphi} \frac{d\bar{p}_s}{dT} \frac{T_{s,i} - T_{1,2}}{\Delta x} \right) \tag{5.3}$$

$$j_{w,1} = -\bar{k} \frac{\partial u}{\partial \varphi} \frac{\varphi_{s,i} - \varphi_{1,2}}{\Delta x} \tag{5.4}$$

where $\Delta x = d_1$ represents the insulation thickness; the saturation pressure $\bar{p}_s$ and the liquid water diffusivity $\bar{k}$ are calculated at mean values of temperature and relative humidity defined as follows:

$$\bar{\varphi} = \frac{\varphi_{s,i} + \varphi_{1,2}}{2} \tag{5.5}$$

$$\bar{T} = \frac{T_{s,i} + T_{1,2}}{2} \tag{5.6}$$

the mean value of the liquid water diffusivity is calculated by integration of equation (2.10) over the insulation thickness as follows:

$$\bar{k} = \frac{\int_{u_{s,i}}^{u_{1,2}} k(u) du}{u_{1,2} - u_{s,i}} \tag{5.7}$$

where the values of the water content at the internal surface $(u_{s,i})$ and behind the insulation $(u_{1,2})$ can be expressed as functions of the relative humidity due to the moisture retention curve (see sections 2.2.1 and 4.3). Notice that the moisture retention curve $(u(\varphi))$ is nearly linear in the hygroscopic range $(\varphi < 0.95)$, hence in this range it can be written in the following form with good approximation:

$$u = C_1 + C_2 \, \varphi \tag{5.8}$$

$$\frac{\partial u}{\partial \varphi} = C_2 \tag{5.9}$$

where the coefficients C_1 and C_2 are obtained by comparison with measured data.

From equations (5.3), (5.4) and (5.2) the following expression for $\varphi_{1,2}$ is derived:

$$\varphi_{1,2} = \varphi_{s,i} + \left(\frac{D_v p_s}{R_v \bar{T} \bar{\mu}} + \bar{k} \frac{\partial u}{\partial \varphi} \right)^{-1} \frac{D_v \bar{\varphi}}{R_v \bar{T} \mu} \frac{dp_s}{dT} \left(T_{s,i} - T_{1,2} \right) \tag{5.10}$$

Employing equations (5.5) to (5.10), after mathematical transformation, the following closed-form for the relative humidity behind the insulation is derived:

$$\varphi_{1,2} = \varphi_{s,i} \frac{2 \left(\bar{k} C_2 + \frac{D_v p_s}{R_v \bar{T} \bar{\mu}} \right) + \frac{dp_s}{dT} \left(T_{s,i} - T_{1,2} \right)}{2 \left(\bar{k} C_2 + \frac{D_v p_s}{R_v \bar{T} \bar{\mu}} \right) - \frac{dp_s}{dT} \left(T_{s,i} - T_{1,2} \right)} \tag{5.11}$$

Since in equation (5.11) the parameter $\bar{k}$ depends on $\varphi_{1,2}$, an iterative procedure has to be employed for solving the problem. The remaining terms on the right hand side of equation (5.11) are defined as follows:

$$T_{1,2} = T_i - \left(\frac{1}{\alpha_i} + \frac{d_1}{\lambda_1} \right) \dot{q} \tag{5.12}$$

$$T_{s,i} = T_i - \frac{1}{\alpha_i} \dot{q} \tag{5.13}$$

where α_i is the internal heat transfer coefficient and $\dot{q}$ the heat flux through the wall defined as follows:

$$\dot{q} = U \; (T_i - T_e) \tag{5.14}$$

being U the overall conductance of the wall.

The relative humidity at the internal surface can be determined according to the following equation, assuming approximately the same partial pressure of water vapor in the air and at the surface:

$$p_{v,s,i} = p_{v,i} \tag{5.15}$$

$$\varphi_{s,i} = \varphi_i \frac{p_s(T_i)}{p_s(T_{s,i})} \tag{5.16}$$

5.2.2   Results evaluation

In order to evaluate the sensitivity of different internal insulation systems with respect to material properties, boundary conditions and insulation thickness, a parameter study has been performed.

The results of the simplified method presented above are compared with those obtained by the standard Glaser-method and by time-dependent numerical simulations with the software Comsol. The numerical simulation with applied periodic boundary conditions for temperature and relative humidity, can be considered as a good approximation of the real construction behavior in absence of driving rain on the facade.

The considered cases without a vapor retarder on the internal surface are reported in tables 5.1 and 5.2; whereas table 5.3 refers to the cases with an applied vapor retarder.

In figure 5.3 the values of relative humidity behind the insulation are reported. The results of the time dependent numerical simulation are here the maximal values reached during the heating period (worst case).

It can be observed that, in absence of a vapor retarder and with capillary active internal insulation (cases 1 to 74), the method proposed above is always conservative with respect to the numerical simulation. Moreover, for mid-range relative humidity ($0.5 < \varphi_{1,2} < 0.8$) the simplified model approximates very well the numerical results. Note that the Glaser method indicates in the most cases water condensation, thus it does not give useful information on the system quality.

In figure 5.2 can be observed that the simplified model is able to reproduce properly the trend of $\varphi_{1,2}$ in case of capillary active insulation and in absence of a vapor retarder. Coherently, the predicted trend of $\varphi_{1,2}$ decreases with the insulation thickness, whereas higher values of the diffusion resistance factor μ and of the thermal conductivity lead to lower moisture behind the insulation (figure 5.2 a) and b). As expected, the internal relative humidity presents a strong influence on the results (figure 5.2 c); however, the parameter having the main impact on the moisture level behind the insulation is the liquid water diffusivity (figure 5.2 d). Hence, an accurate assessment of this material property is essential for the correct prediction of the moisture risk.

For insulation with low capillary action, the method proposed in the previous section is not adequate. In case a vapor retarder with moderate s_d value is applied (figure 5.3, cases 75 to 78), the standard Glaser-Method gives still an acceptable approximation of the numerical results; whereas for high s_d-values it may underestimate the relative humidity behind the insulation.

5.3   Timber beam ends integrated in an external wall

At timber beam ends integrated in external walls may occur critical moisture conditions, in particular if thermal insulation is applied on the internal side of the wall. This is in part due to the fact that the external wall remains cold during the winter, adsorbing water vapor. Moreover, since an air tight junction
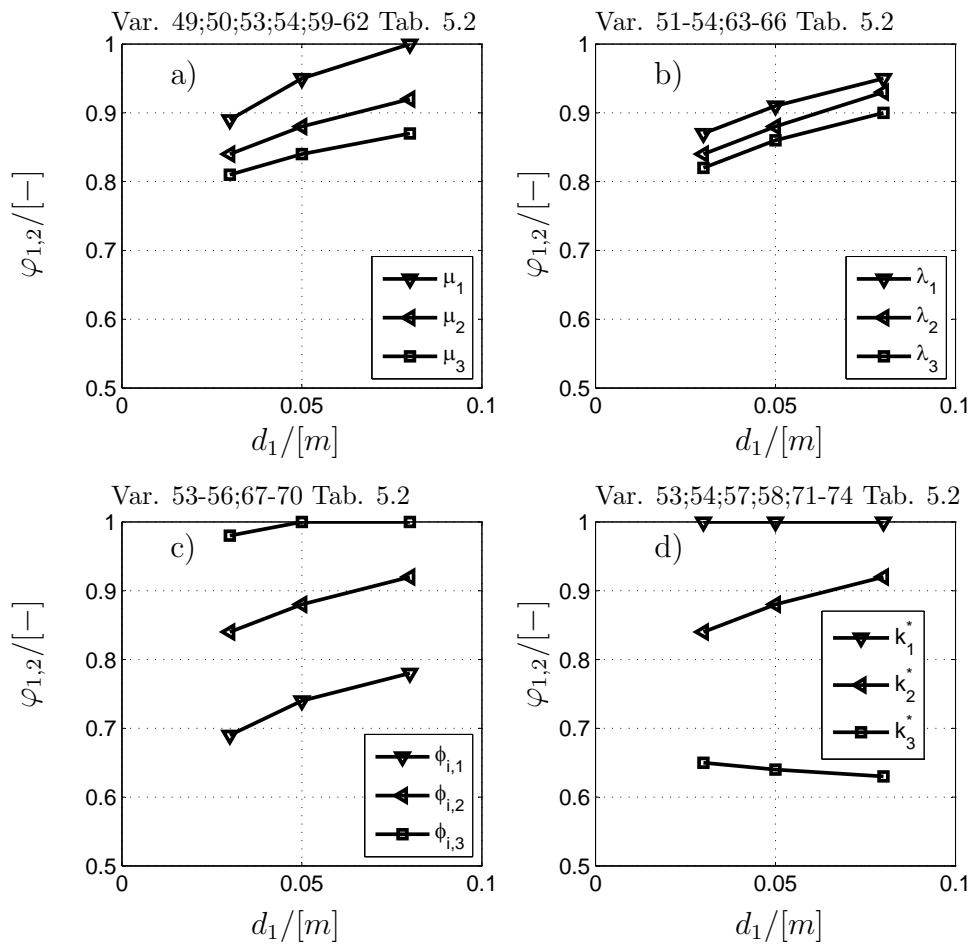
Figure 5.2: Relative humidity behind the insulation as a function of the insulation thickness calculated according to equation (5.11). Influence of different model parameters: a) diffusion resistance factor of the insulation: $\mu_1 = 4$; $\mu_2 = 6$; $\mu_3 = 8$; b) thermal conductivity of the insulation: $\lambda_1 = 0.05\frac{W}{mK}$; $\lambda_2 = 0.07\frac{W}{mK}$; $\lambda_3 = 0.09\frac{W}{mK}$; c) internal relative humidity: $\varphi_{i,1} = 0.4$; $\varphi_{i,2} = 0.5$; $\varphi_{i,3} = 0.6$; d) max. liquid water diffusivity: $k_1^* = 1E-8\frac{m^2}{s}$; $k_2^* = 1e-7\frac{m^2}{s}$; $k_3^* = 1E-6\frac{m^2}{s}$
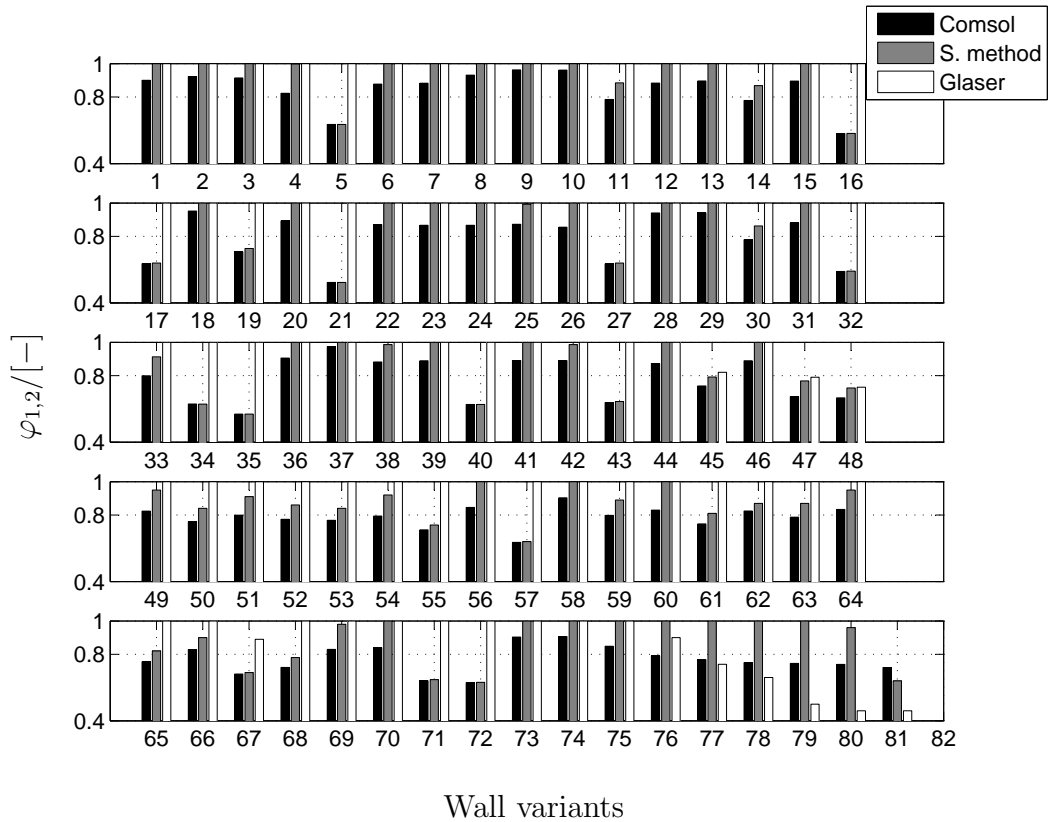
Figure 5.3: Relative humidity behind the insulation for the cases reported in tables 5.1, 5.2 (systems without vapor retarder) and 5.3 (systems with vapor retarder). Comparison between numerical simulation (Comsol), standard Glaser-method and simplified analytical model presented in this study

Table 5.1: Wall variants without a vapor retarder on the internal surface. Values of relative humidity behind insulation calculated with the simplified model (φ_s), the Glaser method (φ_g) and simulated with Comsol (φ_c)

| var.	μ	λ	k^*	ζ	k	d_1	φ_i	φ_s	φ_g	φ_c	$\vartheta_{1,2}$
	[−]	$[\frac{W}{mK}]$	$[\frac{m^2}{s}]$	[−]	$[\frac{m^2}{s}]$	[cm]	[−]	[−]	[−]	[−]	[°C]
1	6	0.07	1e-07	1.8	1.07e-10	5	0.5	1	1.00	0.90	5.3
2	4	0.07	1e-07	1.8	1.12e-10	5	0.5	1	1.00	0.92	5.3
3	6	0.05	1e-07	1.8	1.20e-10	5	0.5	1	1.00	0.91	3.7
4	6	0.07	1e-07	1.8	8.35e-11	5	0.4	1	1.00	0.82	5.3
5	6	0.07	1e-05	1.8	4.90e-09	5	0.5	0.64	1.00	1.00	5.3
6	8	0.07	1e-07	1.8	1.03e-10	5	0.5	1	1.00	0.88	5.3
7	6	0.09	1e-07	1.8	9.77e-11	5	0.5	1	1.00	0.88	6.5
8	6	0.07	1e-07	1.8	1.31e-10	5	0.6	1	1.00	0.93	5.3
9	6	0.07	1e-09	1.8	1.27e-12	5	0.5	1	1.00	0.96	5.3
10	6	0.07	1e-07	3.8	1.80e-12	5	0.5	1	1.00	0.96	5.3
11	6	0.07	1e-07	0.8	6.47e-10	5	0.5	0.88	1.00	0.79	5.3
12	6	0.07	1e-07	1.8	2.58e-12	3	0.5	1	1.00	0.88	3
13	6	0.07	1e-07	3.8	1.30e-12	8	0.5	1	1.00	0.90	7.7
14	6	0.07	1e-06	1.8	7.06e-10	5	0.5	0.87	1.00	0.78	5.3
15	6	0.07	1e-05	3.8	1.38e-10	5	0.5	1	1.00	0.90	5.3
16	6	0.07	1e-05	0.8	4.13e-08	5	0.5	0.58	1.00	0.58	5.3
17	6	0.07	1e-06	0.8	4.56e-09	5	0.5	0.64	1.00	0.64	5.3
18	6	0.07	1e-09	0.8	1.05e-11	5	0.5	1	1.00	0.95	5.3
19	6	0.07	1e-06	1.8	5.72e-10	5	0.4	0.73	1.00	0.71	5.3
20	6	0.07	1e-06	3.8	1.23e-11	5	0.4	1	1.00	0.89	5.3
21	6	0.07	1e-06	0.8	3.69e-09	5	0.4	0.52	1.00	1.00	5.3
22	6	0.07	1e-09	1.8	9.51e-13	5	0.4	1	1.00	0.87	5.3
23	6	0.07	1e-09	3.8	1.26e-14	5	0.4	1	1.00	0.87	5.3
24	6	0.07	1e-09	0.8	8.20e-12	5	0.4	1	1.00	0.87	5.3
25	6	0.07	1e-07	1.8	8.30e-11	2.4	0.5	0.99	1.00	0.87	8.7
26	13	0.07	1e-07	1.8	9.53e-11	5	0.5	1	1.00	0.85	5.3
27	6	0.09	1e-05	1.8	4.94e-09	5	0.5	0.64	1.00	0.63	6.5
28	6	0.09	1e-09	1.8	1.11e-12	5	0.5	1	1.00	0.94	6.5
29	6	0.09	1e-07	3.8	1.52e-12	5	0.5	1	1.00	0.94	6.5
30	6	0.09	1e-07	0.8	6.29e-10	5	0.5	0.86	1.00	0.78	6.5
31	6	0.09	1e-05	3.8	1.25e-10	5	0.5	1	1.00	0.88	6.5
32	6	0.09	1e-05	0.8	4.20e-08	5	0.5	0.59	1.00	0.59	6.5
33	6	0.05	1e-07	0.8	6.70e-10	5	0.5	0.91	1.00	0.80	3.7
34	6	0.05	1e-05	1.8	4.84e-09	5	0.5	0.63	1.00	0.63	3.7
35	6	0.05	1e-05	0.8	9.71e-08	5	0.5	1	1.00	0.57	3.7
36	6	0.05	1e-05	3.8	2.31e-12	5	0.5	1	1.00	0.91	3.7
37	6	0.05	1e-07	3.8	2.31e-12	5	0.5	1	1.00	0.97	3.7
38	6	0.15	1e-07	1.8	8.23e-11	5	0.5	0.99	1.00	0.88	8.8
39	6	0.09	1e-07	1.8	1.16e-10	0.08	0.5	1	1.00	0.89	4.2
40	6	0.07	1e-05	1.8	4.82e-09	0.08	0.5	0.63	1.00	1.00	3
41	6	0.07	1e-05	0.8	1.65e-10	0.08	0.5	1	1.00	0.89	3
42	6	0.09	1e-07	1.8	8.23e-11	0.03	0.5	0.99	1.00	0.89	8.8
43	6	0.07	1e-05	1.8	4.98e-09	0.03	0.5	0.64	1.00	0.64	7.7
44	6	0.07	1e-05	3.8	1.13e-10	0.03	0.5	1	1.00	0.87	7.7
45	6	0.09	1e-07	1.8	9.46e-11	0.03	0.4	0.79	0.82	0.74	3
46	8	0.07	1e-07	1.8	9.46e-11	0.08	0.4	1	1.00	0.89	3
47	6	0.07	1e-07	1.8	6.10e-11	5	0.3	0.77	0.79	0.67	5.3

Table 5.2: Wall variants with capillary active insulation in absence of a vapor retarder on the internal surface (figure 5.3). Values of relative humidity behind insulation calculated with the simplified model (φ_s), the Glaser method (φ_g) and simulated with Comsol (φ_c)

var.	μ	λ	k^*	ζ	$\bar{k}$	d_1	φ_i	φ_s	φ_g	φ_c	$\vartheta_{1,2}$
	$[-]$	$[\frac{W}{mK}]$	$[\frac{m^2}{s}]$	$[-]$	$[\frac{m^2}{s}]$	$[cm]$	$[-]$	$[-]$	$[-]$	$[-]$	$[°C]$
48	6	1	1e-07	1.8	5.71e-11	5	0.5	0.73	0.73	0.67	14
49	4	0.07	1e-07	0.8	7.00e-10	5	0.5	0.95	1.00	0.82	5.3
50	8	0.07	1e-07	0.8	6.13e-10	5	0.5	0.84	1.00	0.76	5.3
51	6	0.05	1e-07	0.8	6.70e-10	5	0.5	0.91	1.00	0.80	3.7
52	6	0.09	1e-07	0.8	6.29e-10	5	0.5	0.86	1.00	0.77	6.5
53	6	0.07	1e-07	0.8	6.11e-10	3	0.5	0.84	1.00	0.77	7.7
54	6	0.07	1e-07	0.8	6.78e-10	8	0.5	0.92	1.00	0.79	3
55	6	0.07	1e-07	0.8	5.33e-10	5	0.4	0.74	1.00	0.71	5.3
56	6	0.07	1e-07	0.8	7.61e-10	5	0.6	1	1.00	0.85	5.3
57	6	0.07	1e-06	0.8	4.56e-09	5	0.5	0.64	1.00	0.64	5.3
58	6	0.07	1e-08	0.8	9.35e-11	5	0.5	1	1.00	0.90	5.3
59	4	0.07	1e-07	0.8	6.48e-10	3	0.5	0.89	1.00	0.80	7.7
60	4	0.07	1e-07	0.8	7.44e-10	8	0.5	1	1.00	0.83	3
61	8	0.07	1e-07	0.8	5.85e-10	3	0.5	0.8	1.00	0.75	7.7
62	8	0.07	1e-07	0.8	6.35e-10	8	0.5	0.87	1.00	0.82	3
63	6	0.05	1e-07	0.8	6.35e-10	3	0.5	0.87	1.00	0.79	6.1
64	6	0.05	1e-07	0.8	6.97e-10	8	0.5	0.95	1.00	0.83	1.6
65	6	0.09	1e-07	0.8	5.93e-10	3	0.5	0.82	1.00	0.75	8.8
66	6	0.09	1e-07	0.8	6.62e-10	8	0.5	0.9	1.00	0.83	4.2
67	6	0.07	1e-07	0.8	4.97e-10	3	0.4	0.69	0.89	0.68	7.7
68	6	0.07	1e-07	0.8	5.63e-10	8	0.4	0.78	1.00	0.72	3
69	6	0.07	1e-07	0.8	7.23e-10	3	0.6	0.98	1.00	0.83	7.7
70	6	0.07	1e-07	0.8	7.91e-10	8	0.6	1	1.00	0.84	3
71	6	0.07	1e-06	0.8	4.63e-09	3	0.5	0.65	1.00	0.64	7.7
72	6	0.07	1e-06	0.8	4.50e-09	8	0.5	0.63	1.00	0.63	3
73	6	0.07	1e-08	0.8	7.91e-11	3	0.5	1	1.00	0.90	7.7
74	6	0.07	1e-08	0.8	1.09e-10	8	0.5	1	1.00	0.91	3

Table 5.3: Wall variants with vapor retarder. Values of relative humidity behind insulation calculated with the simplified model (φ_s), the Glaser method (φ_g) and simulated with Comsol (φ_c)

var.	μ	λ	k^*	ζ	$\bar{k}$	d_1	φ_i	s_d	φ_s	φ_g	φ_c	$\vartheta_{1,2}$
	$[-]$	$[\frac{W}{mK}]$	$[\frac{m^2}{s}]$	$[-]$	$[\frac{m^2}{s}]$	$[cm]$	$[-]$	$[m]$	$[-]$	$[-]$	$[-]$	$[°C]$
75	2	0.05	1e-09	1.8	1.5e-12	5	0.5	2	1	1	0.85	3.7
76	2	0.05	1e-09	1.8	1.4e-12	5	0.5	5	1	0.9	0.79	3.7
77	2	0.05	1e-09	1.8	1.4e-12	5	0.5	10	1	0.74	0.77	3.7
78	2	0.05	1e-09	1.8	1.3e-12	5	0.5	15	1	0.66	0.75	3.7
79	2	0.05	1e-09	1.8	9.5e-13	5	0.5	100	1	0.5	0.75	3.7
80	2	0.05	1e-09	1.8	6.5e-13	5	0.5	500	0.8	0.46	0.74	3.7
81	2	0.05	1e-09	1.8	5.7e-13	5	0.5	1000	0.72	0.46	0.72	3.7

between beam and wall is hardly achievable, warm, humid air may stream from the inside of the building keeping further moisture inside the construction. Even water condensation may occur, since the air decreases its temperature by coming into contact with the wall. The schematic of the construction we are taking into account is show in figure 5.4.

The problem of timber beams embedded in an internal insulated wall has been the object of numerous scientific projects in the last years (e.g. [32]). In this work we focus on the influence of convection (streaming air in gaps between wall and beam) and on comparing three dimensional and two dimensional models. This second task aims to find out if the effort required by complex three dimensional analysis is justified or may be avoided without loosing accuracy.

5.3.1   Influence of convection

In case air thickness at the junction between insulation and floor is not guaranteed, the moisture transfer due to convection may significantly overcome the diffusive transfer [11].

In figure 5.4 the floor-wall junction of a building with installed internal insulation is represented.

For modeling the streaming air inside the thin gap between beam and wall, the line-source model, introduced in section 3.3, is employed. This one-dimensional flow model is coupled with the two-dimensional moisture and heat diffusion inside the construction, described by the PDE system reported in section 2.6.

The volumetric air flow through the gap, needed as simulation input, is calculated as function of the pressure drop over the gap Δp, according to the following power low:

$$\dot{V} = C\Delta p^n \tag{5.17}$$

where the coefficients C and n, depending on the gap dimension and on the roughness of the surfaces, have to be determined through experimental procedure. Values measured by Peper [55] for different sealing systems are reported in table 5.4. Variants a to d refer to different employed sealing methods: the reference case (variant a) represents a perfect air tight construction, whereas variant d refers to sealing due to adhesive tape only. The other variants represent intermediate states between these two limit cases.

It can be observed that, due to the reduced gap thickness (assumed as $2\ mm$) and the low volumetric flow, laminar flow occurs (Reynolds-number: $Re << 10^4$).

In order to calculate the volumetric air flow through equation (5.17), the pressure drop over the single ceiling has to be previously evaluated. This can be determined considering the pronounced stack effect during the heating period, which determines the air flow directed from the bottom to the top of the building [59]. The total pressure drop between the air inflow (building bottom) and outflow (building top), can be expressed according to Bernoulli in two different ways, through equations (5.18) and (5.19):

$$\Delta p_{ext} = g\rho_{g,out}(z_2 - z_1) \tag{5.18}$$

Table 5.4: Volumetric air flow $\dot{V}$ and air velocity v for different sealing variants (*values calculated assuming a gap thickness of 2 mm)

| sealing variant	n [−]	C [$m^3/(hPa^n)$]	Max. $\dot{V}$ [m^3/h]	Max. v * [m/s]	Max. Re* [−]
a	−	−	0	0	−
b	0.6	0.01	0.02	0.0028	0.4
c	0.61	0.034	0.07	0.009	1.3
d	0.59	0.669	1.32	0.183	26.4
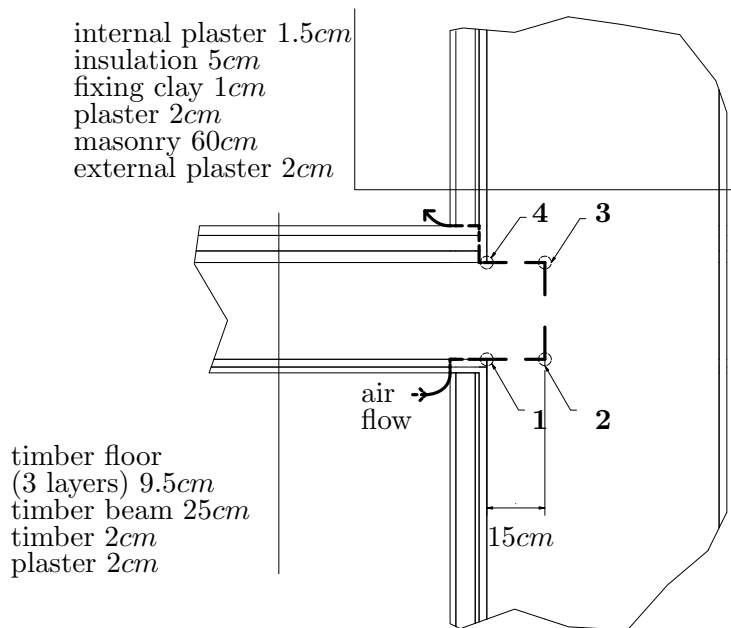
Figure 5.4: Schematic of the floor-wall junction. Positions 1 to 4 refer to the results reported in figures 5.6 and 5.7

$$\Delta p_{int} = g\rho_{g,int}(z_2 - z_1) + \frac{1}{2}\rho_{g,int}(v_2^2 - v_1^2) + \sum_{i=1}^{N}(\Delta p_i) \tag{5.19}$$

where $\rho_{g,out}$ is the density of air at outside conditions (assumed as a constant), g is the gravity acceleration, $h = z_2 - z_1$ is the high of the building and Δp_i is the pressure loss concentrated on the i-th floor.

The pressure drop outside the building Δp_{ext} is equal to the pressure drop inside the building Δp_{int}, since they refer to the same inlet and outlet positions. It applies:

$$\Delta p_{ext} = \Delta p_{int} \tag{5.20}$$

moreover, considering air as an ideal gas, we can write:

$$\rho_{g,out} = \frac{p}{R_a T_{out}} \tag{5.21}$$

$$\rho_{g,int} = \frac{p}{R_a T_{int}} \tag{5.22}$$

The internal and the external temperatures T_{int} and T_{out} are assumed to be constant. According to equations (5.18) to (5.22), the sum of the pressure losses inside the building is derived:

$$\sum_{i=1}^{N}(\Delta p_i) = \rho_{g,out}gh\frac{T_{int} - T_{out}}{T_{int}} \tag{5.23}$$

where N represents the number of floors. Assuming equal pressure drop Δp on every floor we finally obtain:

$$\Delta p = \frac{1}{N}\rho_{g,out}gh\frac{T_{int} - T_{out}}{T_{int}} \tag{5.24}$$

which gives the pressure drop over the single floor.

The material data employed for the simulation, as well as the boundary conditions are reported in [11].

In figure 5.5, the temperature and humidity fields at different times are reported for case d (sealing due to adhesive tape only). These images show that, during the winter period, the streaming air keeps moisture inside the construction, which however is getting dry during the summer.

In order to evaluate the moisture damage risk for timber components and the mold germination risk, four positions indicated in figure 5.4 are considered. The values of relative humidity versus temperature for the sealing variants reported in table 5.4 are shown in figure 5.6. In the same diagrams are indicated the mold germination limit and the timber damage limit according to [40] and [65] respectively. These plots show that increasing the volume of streaming air in the gap between beam and masonry leads to higher moisture risk for the construction.

For better quantifying the mold germination risk, further analysis on the simulation results has been performed employing the method proposed by [36].
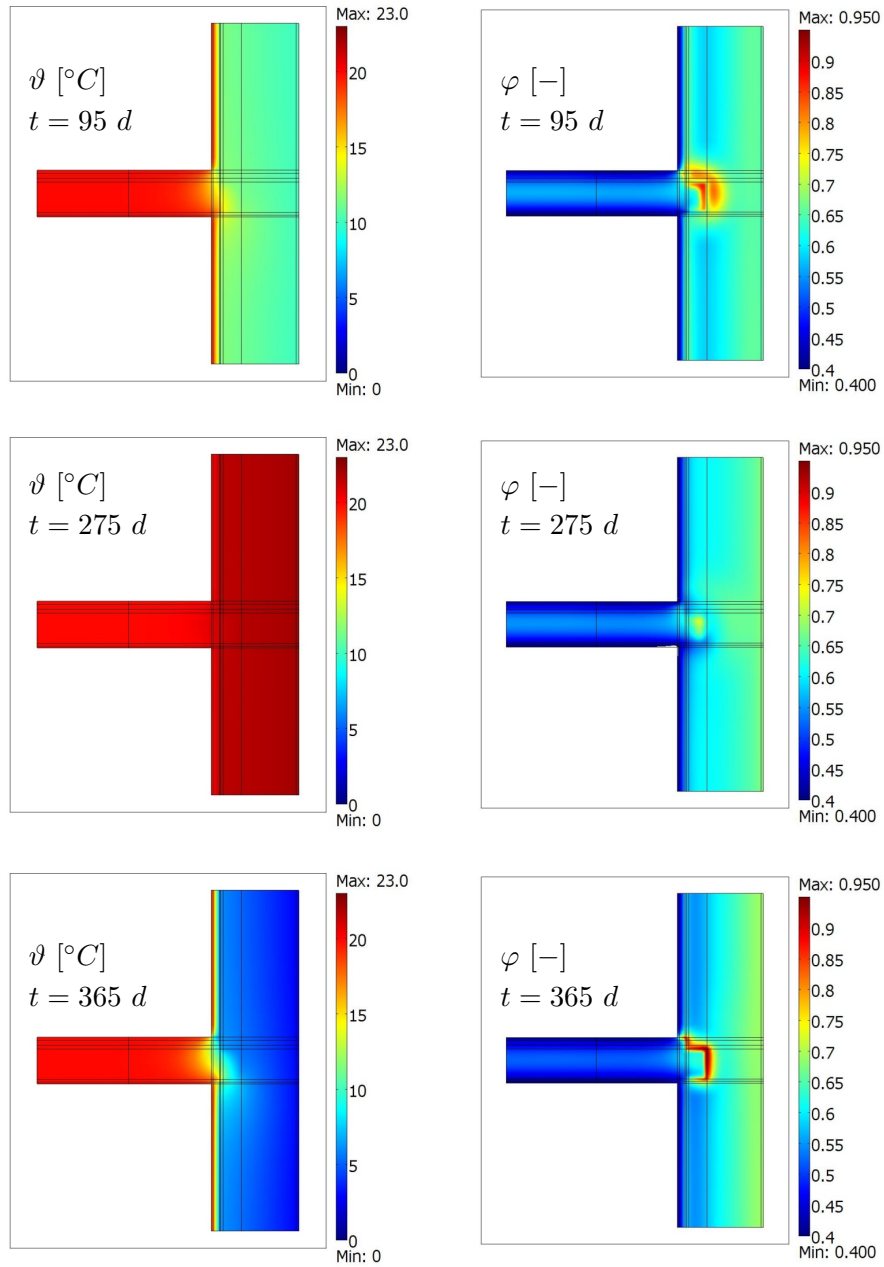
Figure 5.5: Temperature and relative humidity fields in the construction at three different times for variant d (table 5.4)
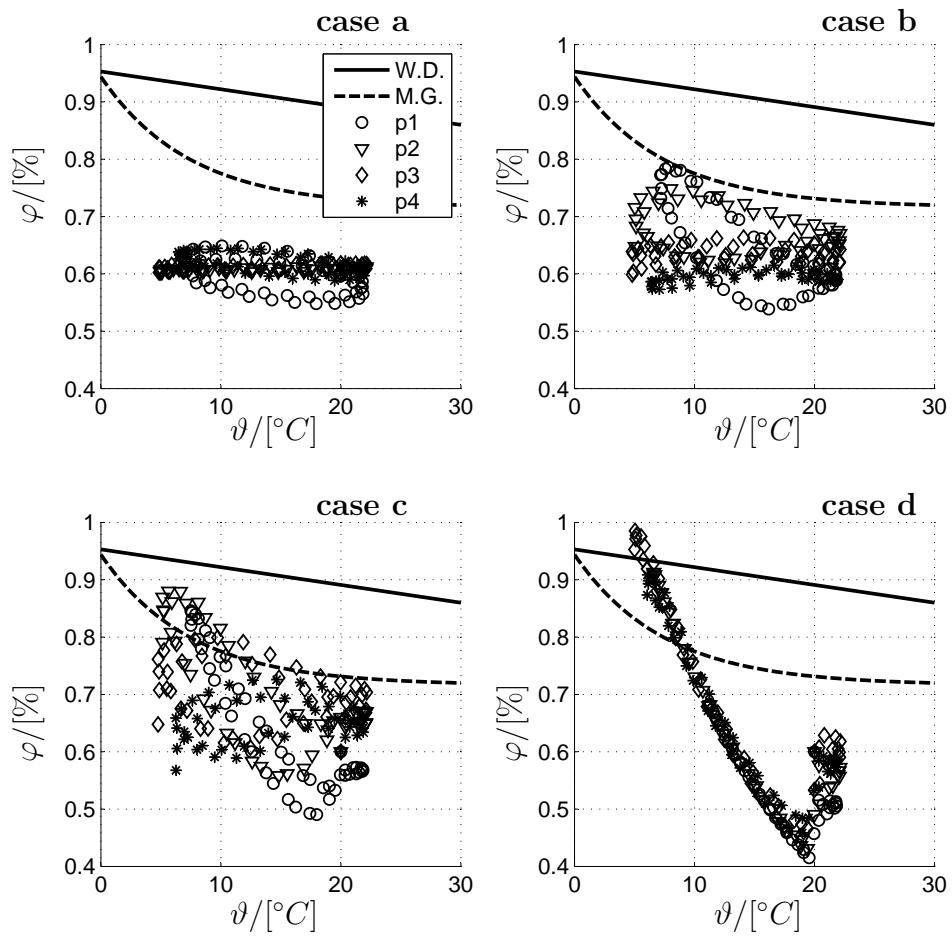
Figure 5.6: Assessment of moisture risk employing wood damage limit (W.D. [40]) and 16-days Isopleth as mold growth limit (M.G. [65]). Cases a to d reported in table 5.4. Positions 1 to 4 (p1-p4) are reported in figure 5.4

This author defined a mold growth rate parameter, called relative dose (RD), which may vary from zero to six ($0 \Rightarrow$ no mold growth; $1 \Rightarrow$ mold growth starts; $6 \Rightarrow$ heavy mold growth). The parameter RD describes the mold growth during the time as function of relative humidity and temperature and is calculated as follows:

$$RD = \frac{D(N)}{N_{ref}} \qquad (5.25)$$

where N_{ref} represents the period of time (in days) after which at reference conditions (φ_{ref}, T_{ref}) mold growth starts. The parameter $D(N)$ is calculated according to the following equations:

$$D(N) = \sum_{1}^{N} \left(D_\varphi D_T \right) \qquad (5.26)$$

$$D_\varphi = e^{C_\varphi ln\left(\frac{\varphi(t)}{\varphi_{ref}} \right)} \qquad (5.27)$$

$$D_T = e^{C_T ln\left(\frac{T(t)}{T_{ref}} \right)} \qquad (5.28)$$

The parameters C_φ and C_T are material and substrate specific and have to be determined experimentally.

This approach is advantageous since it gives information concerning the time development of mold growth. In figure 5.7 the results concerning the four different cases reported in table 5.5 are reported. The relative dose has been calculated assuming reference conditions and substrate parameters for pine sapwood reported in [36] ($\vartheta_{ref} = 20$ °C; $\varphi_{ref} = 0.9$; $C_\varphi = 13.15$; $C_T = 0.67$). Also these results indicate that mold growth risk increases in case the construction is not air tight. This is in accordance with practical experience and confirms the commonly employed criterion that air tightness has to be guaranteed for a moisture safe construction. In addition, this numerical analysis provides a quantitative criterion for hygrothermal evaluation of constructions including thin air cavities with forced convection.

5.3.2   3D versus 2D simulation

In this section the moisture risk at timber beam ends imbedded into an external wall is investigated by means of 2D and 3D numerical simulations.

We consider the floor-wall junction represented in figure 5.8. Thermal insulation is applied on the internal side of the wall. The cavities between the timber beams of the floor are filled by sand in the upper part, whereas they are empty in the lower part. The heat and moisture transfer inside the air cavities is modeled by means of increased equivalent diffusive coefficients, which includes the contribution of natural convection. Forced convection between beam and masonry is not considered since the construction is supposed to be perfectly air tight, thus this analysis focuses only on heat and moisture diffusion, according to the mathematical model presented in chapter 2. Driving rain is not included in the simulation.
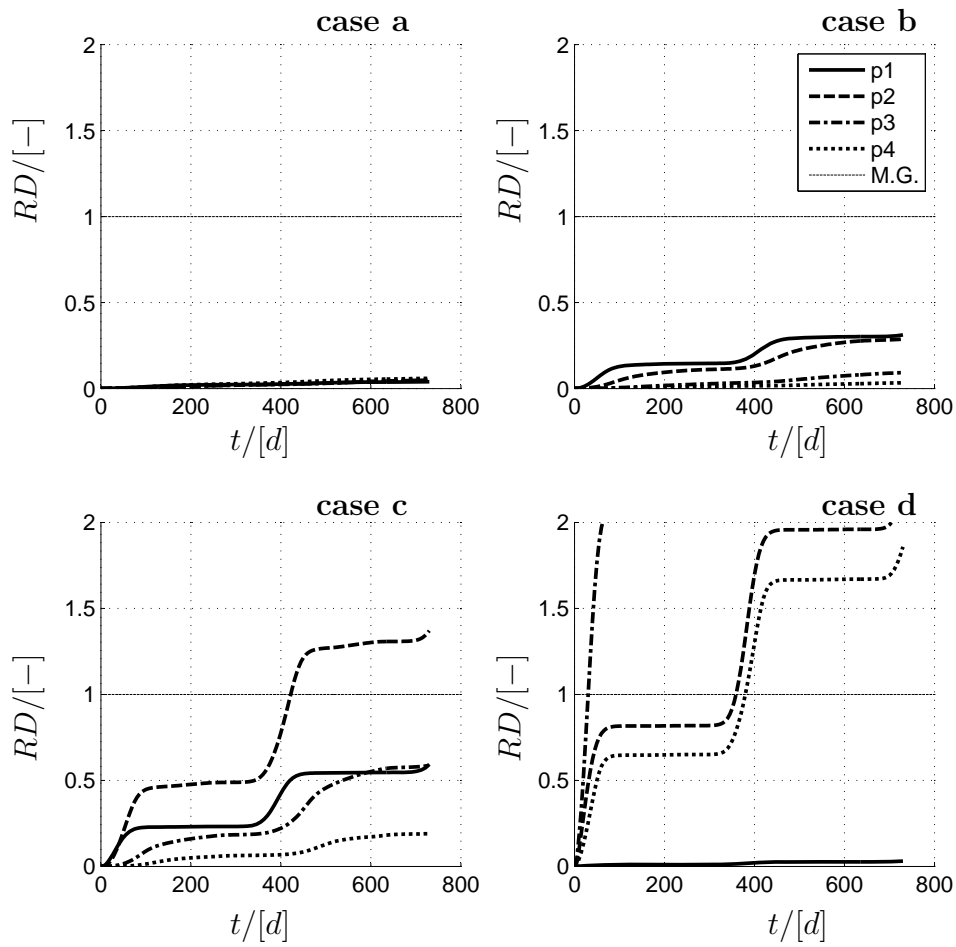
Figure 5.7: Relative dose versus time for the assessment of mold growth risk (M.G.: Mold Growth limit). Cases *a* to *d* reported in table 5.4. Positions 1 to 4 (p1-p4) are reported in figure 5.4

The simulation starts with initial condition $\varphi(t = 0) = 0.8$, with winter conditions on the external boundary and concerns a time period of ten years. More details about material properties and boundary conditions are reported in [12].

The hygrothermal analysis focuses on timber beams, since they are load bearing elements sensitive to moisture damages. In order to guarantee a moisture safe construction, the relative humidity at timber has to remain under a limit value, as explained in the previous section.

In figure 5.9 the temperature and relative humidity fields at three different times during the last simulated year are reported. From these images, it is apparent that moisture content increases under the insulation and at the beam ends during the winter, while it decreases during the summer period.

One purpose of this study is to find out if the hygrothermal behavior of constructions similar to the one taken into consideration, can be described with sufficient accuracy by means of a simple 2D-model, or if a more expensive 3D-analysis is necessary for adequate assessment of the moisture risk.

To this aim, we first consider the section A-A through the beam axis, represented in figure 5.8.

2D simulations are performed with Comsol and Delphin [26], comparing the results with those obtained by means of a 3D Comsol model.

In figure 5.10 the trends of relative humidity during time at different positions are reported. The simulations have been carried out considering five centimeters insulation thickness and an internal relative humidity value of 50%. In this case, at all positions the results by 2D simulations represent the worst case, or, said in other words, the 2D results are conservative with respect to the moisture risk.

By increasing the thickness of the insulation, the results do not change significantly (figures 5.11 and 5.13), while by increasing the internal relative humidity to 60%, the situation becomes more critical (figures 5.12 and 5.14). However, in all cases the deviation between 2D and 3D results is small.

These results show that analysis employing 2D simulation is enough accurate, at least in temperate or cold climates, for "usual" internal conditions (weekly mean value of internal relative humidity $\bar{\varphi}_i \leq 0.6$; internal temperature: $\vartheta_i \approx 20 \ °C$ to 23 $°C$), for ordinary internal insulation values (thermal conductivity: $\lambda \geq 0.03 \ \frac{W}{mK}$; thickness: $d \leq 10 \ cm$) and in absence of significant localized moisture sources. The impact of driving rain on 3D results has to be investigated in future work for further generalization of the these results.

From the technical point of view, the construction taken into consideration may be improved by filling the air cavities between the beams with some capillary active, blow-moldable material or with a vapor-tight polyurethane-foam. Moreover, it is opportune to control the internal relative humidity since this has a large impact on the moisture risk. Thus, a ventilation system is recommended.

Figure 5.8: Wall-floor junction with timber beams. The stratigraphies of the wall and of the floor are reported in figure 5.4
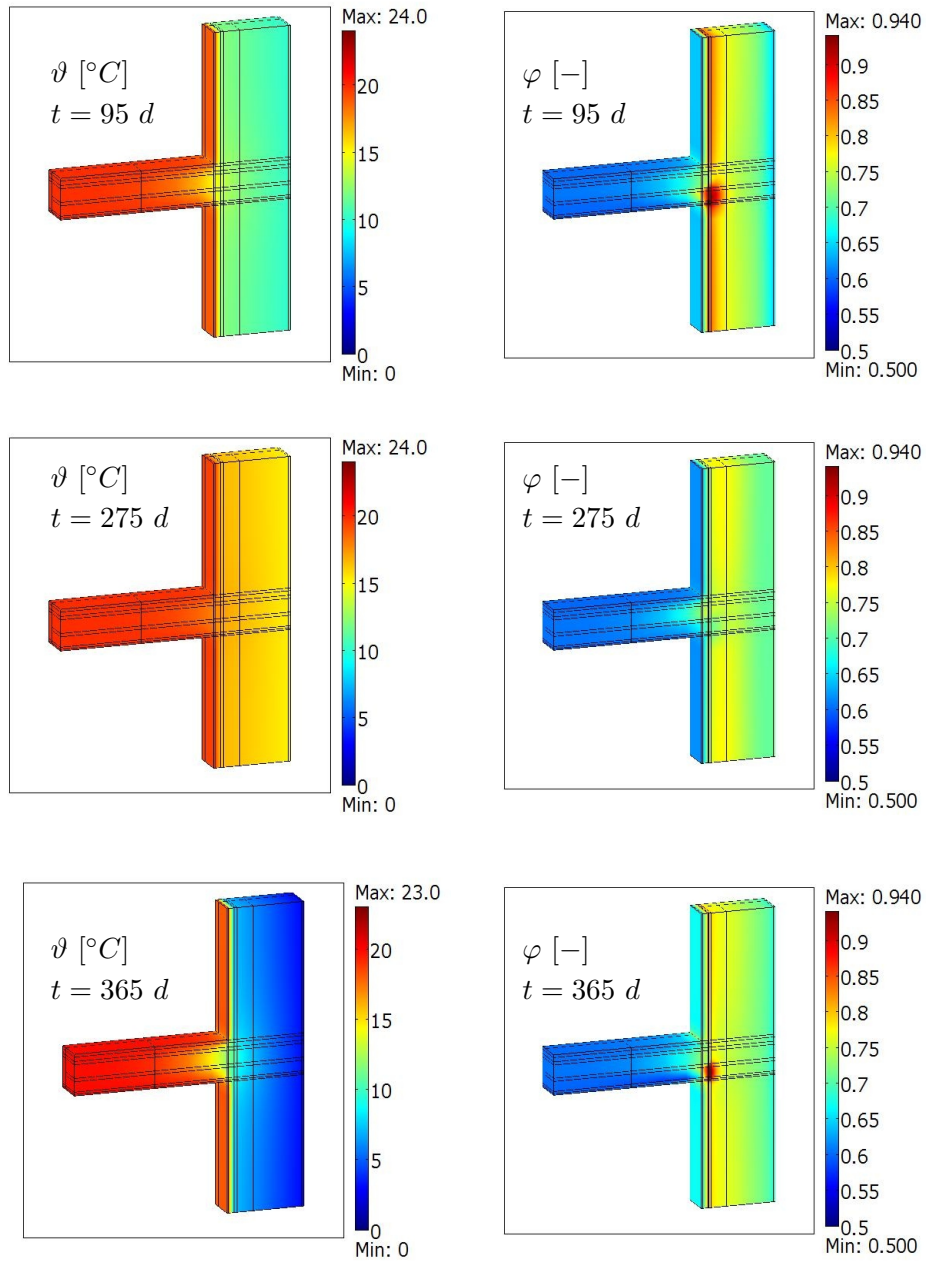
Figure 5.9: 3D temperature and relative humidity fields at three different times during the last simulation year
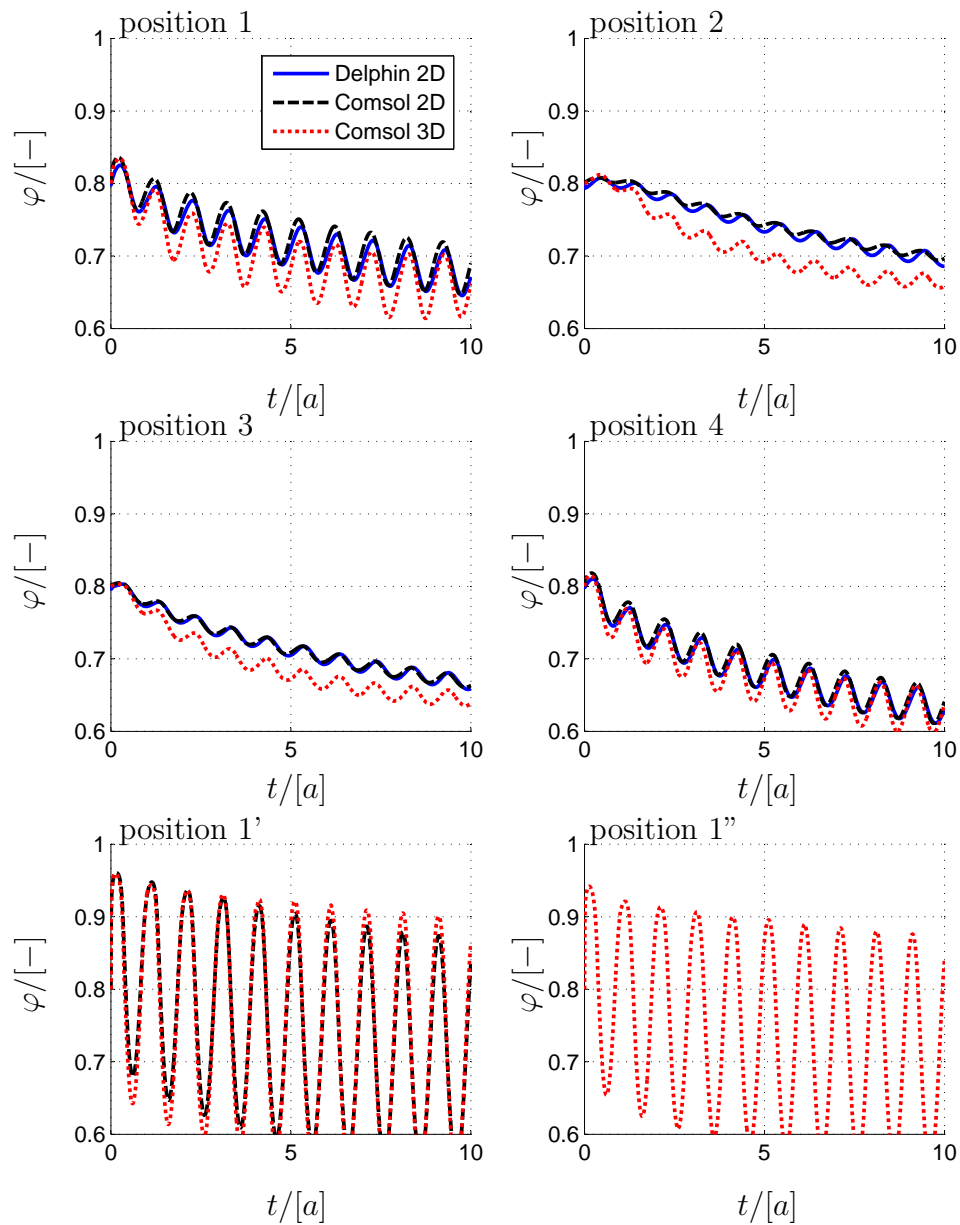
Figure 5.10: Relative humidity trends at six different positions reported in figure 5.8 (insulation thickness $d = 5\ cm$, insulation thermal conductivity $\lambda = 0.031\ [\frac{W}{mK}]$, internal relative humidity: $\varphi_i = 0.5$). Comparison between results obtained by Comsol (2D and 3D) and by Delphin (2D) [26]
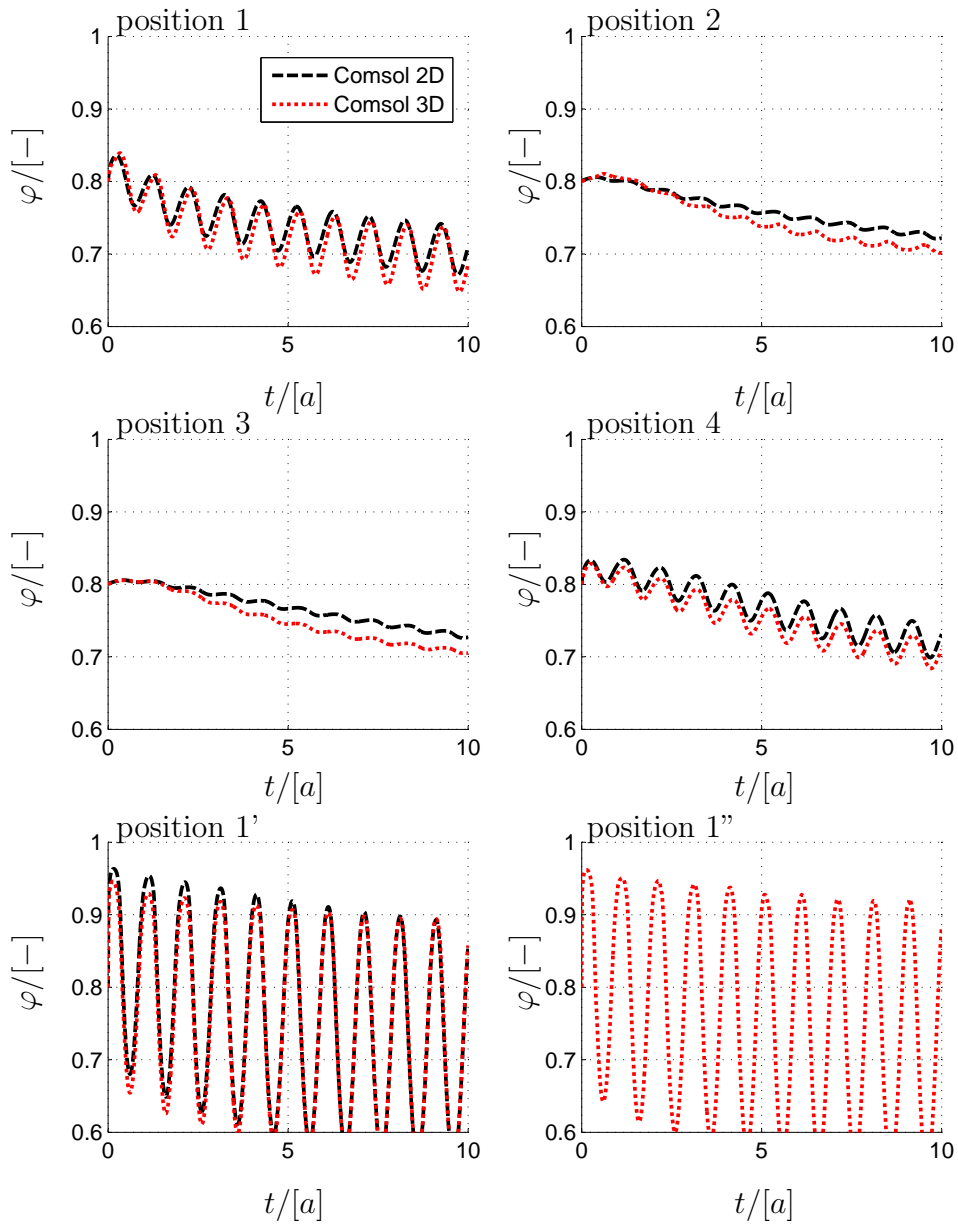
Figure 5.11: Relative humidity trends at six different positions reported in figure 5.8 (insulation thickness $d = 10\ cm$, insulation thermal conductivity $\lambda = 0.031\ [\frac{W}{mK}]$, internal relative humidity: $\varphi_i = 0.5$). Comparison between results obtained by 2D and 3D simulations (Comsol)
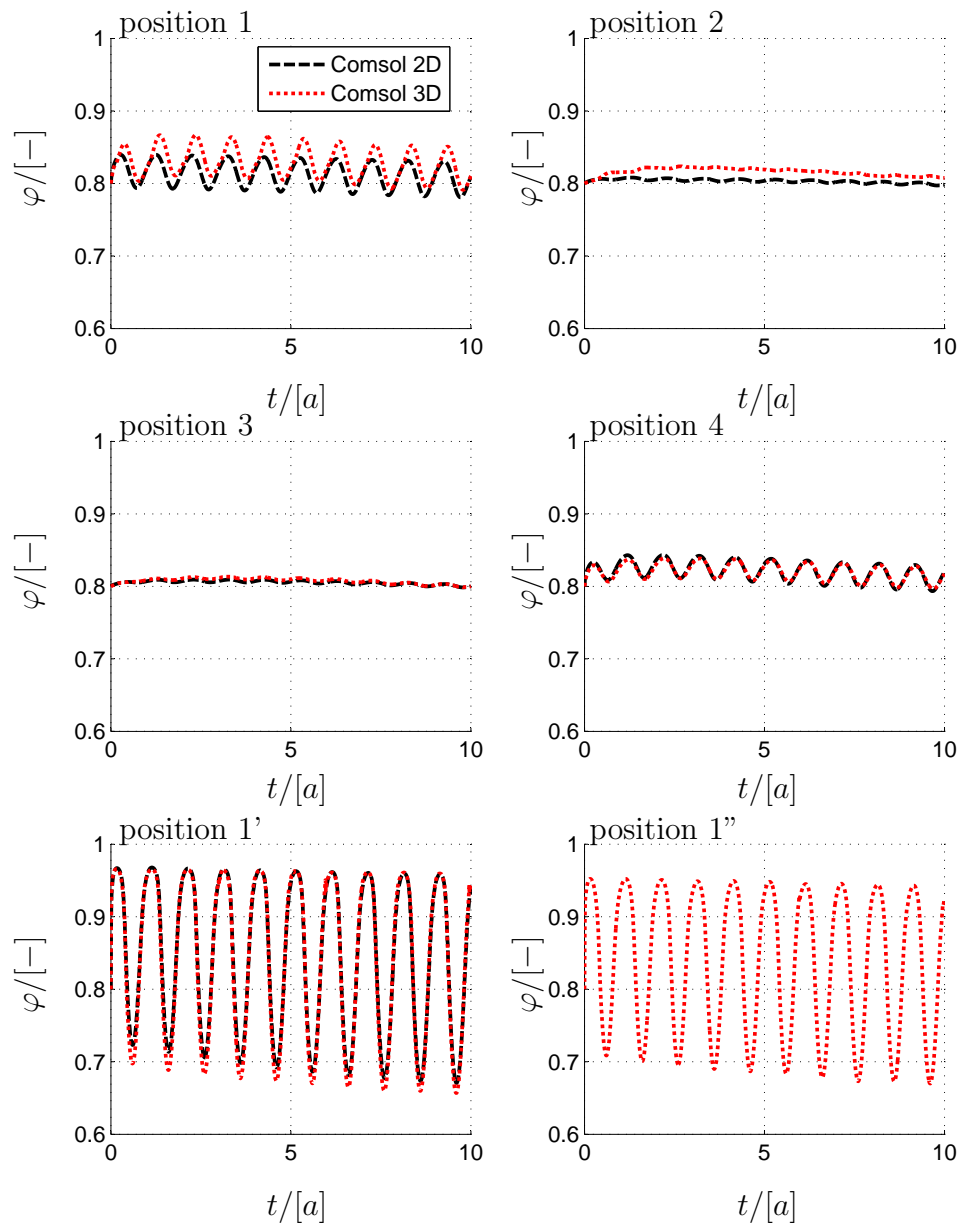
Figure 5.12: Relative humidity trends at six different positions reported in figure 5.8 (insulation thickness $d = 10\ cm$, insulation thermal conductivity $\lambda = 0.031\ [\frac{W}{mK}]$, internal relative humidity: $\varphi_i = 0.6$). Comparison between results obtained by 2D and 3D simulations (Comsol)
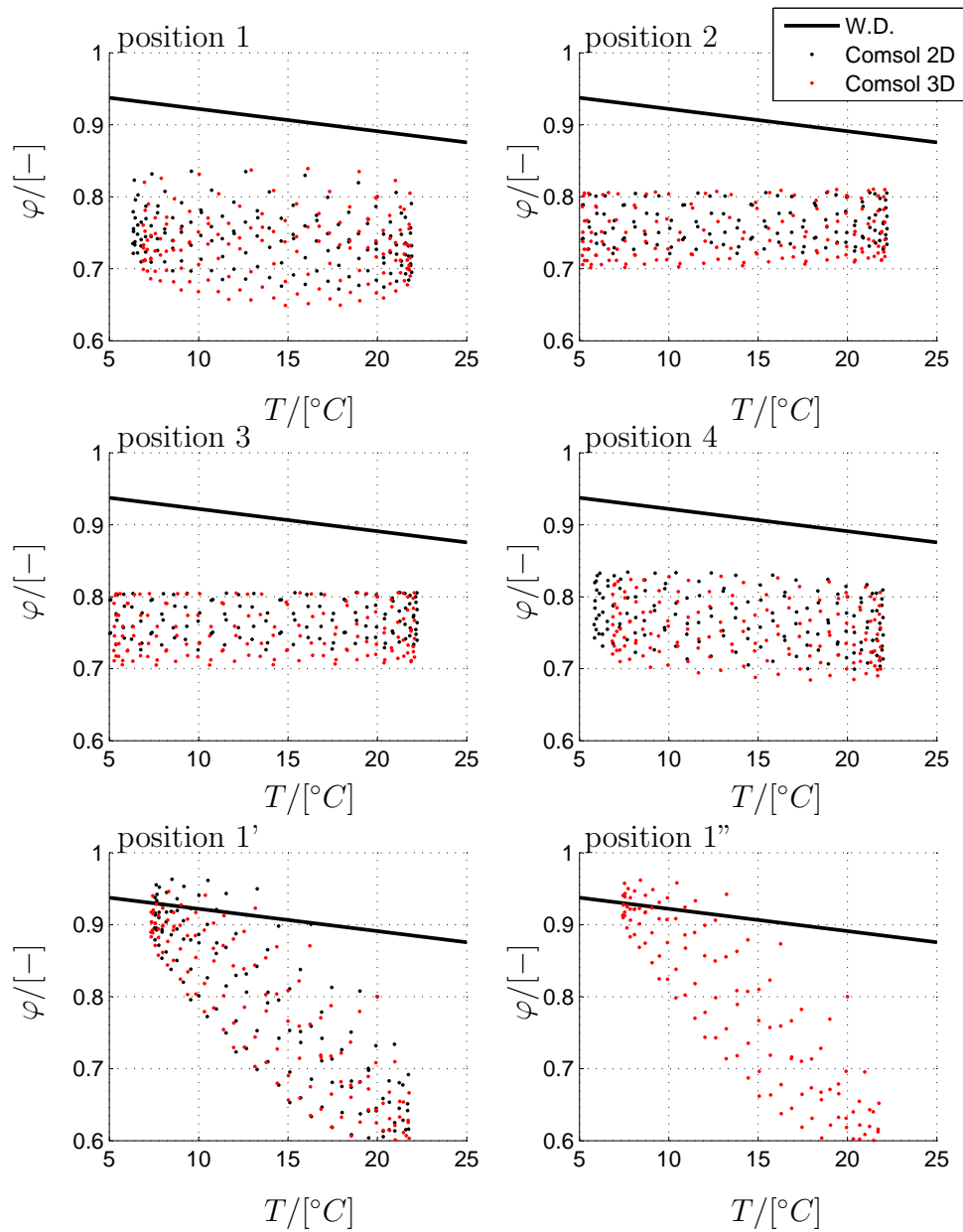
Figure 5.13: Relative humidity versus temperature at six different positions reported in figure 5.8 (insulation thickness $d = 10$ cm, insulation thermal conductivity $\lambda = 0.031$ $[\frac{W}{mK}]$, internal relative humidity: $\varphi_i = 0.5$; W.D.: limit for wood damage risk according to [40]). Comparison between results obtained by 2D and 3D simulations (Comsol)
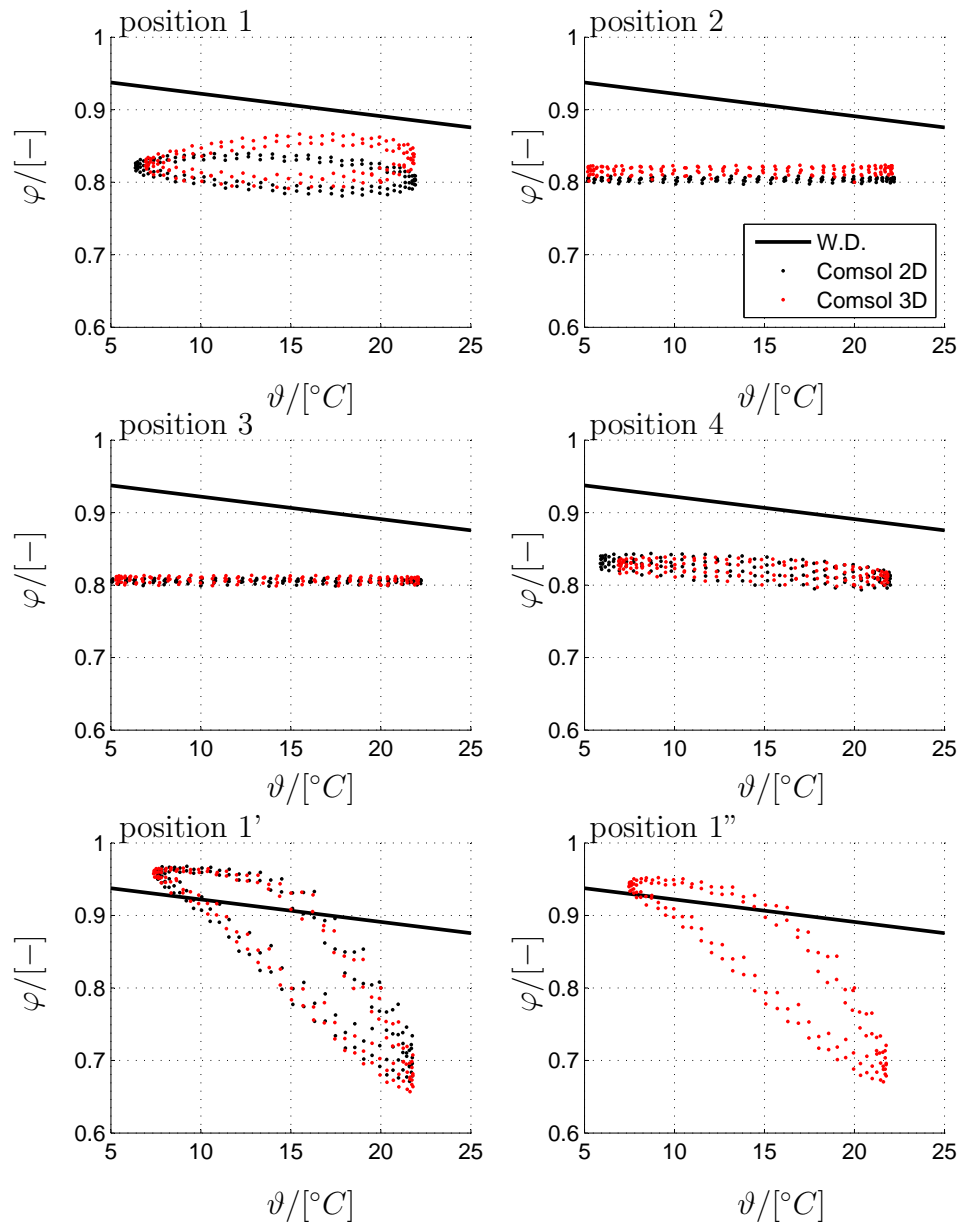
Figure 5.14: Relative humidity versus temperature at six different positions reported in figure 5.8 (insulation thickness $d = 10\ cm$, insulation thermal conductivity $\lambda = 0.031\ [\frac{W}{mK}]$, internal relative humidity: $\varphi_i = 0.6$; W.D.: limit for wood damage risk according to [40]). Comparison between results obtained by 2D and 3D simulations (Comsol)

Chapter 6

Conclusions and outlook

This work aims to extend the current knowledge of heat and moisture transfer in hygroscopic, capillary active materials for building physics applications. Innovative modeling and experimental methods are proposed at both material and component scales.

With respect to the material scale, this study presents two main findings:
First, a function for mathematical description of the liquid water diffusivity, considering the influence of both temperature and water content on this material property, is proposed. This can be considered as a semi-empirical model, since it has a physical interpretation, but also requires a calibration with measured data for determination of the model parameters.
The measured data employed for the calibration have been determined by a procedure based on heat flux measurements, which differs substantially from other methods generally applied to the same aim. Development and testing of this measuring method employing calcium silicate specimens represents the second important task of this work.
The proposed method is advantageous, considering the limited equipment required (only a guarded hot plate apparatus and a balance have been used). It differs from other commonly used methods since no direct measurement of the water content profile is performed; a further advantage is given by the fact that the temperature influence on the liquid water diffusivity can be determined. Moreover, the measured data are also useful for assessment of the diffusion resistance factor in the super-hygroscopic region.
Numerical simulation of the experiments have been performed for visualization, and for better understanding of the transient period.
Considering that the specimens employed for the test comprise two overlapped plates of equal thickness, a challenge of the new method concerns the estimation of the hygric resistance factor at the discontinuity between the upper and the lower part. Since the influence of the interface resistance is not included in this study, the presented results may underestimate the real values. The interface resistance factor can be determined, for instance, by repeating the measurements under equal conditions, but employing monolithic samples with the same thickness. By comparing the heat fluxes through monolithic and double samples the

interface resistance can be estimated. This test will be object of future research work.

Further material characterization has been performed by means of diffusion experiments (dry and wet cups for determination of the diffusion resistance factor in the hygroscopic range), adsorption and desorption experiments. The measured data are coherent with those obtained by means of the heat-plate experiment.

A further task of this study concerns the developing of models for heat and moisture transfer at the component scale.

In this frame, analysis of the moisture risk in complex building components, with a focus on numerical models for long-term simulations, is performed. A large effort is made on the interaction between humid air and porous construction materials involving different transfer mechanisms, like convection and diffusion.

A simplified numerical model for forced convection in thin air gaps (so called line-source model), capable of simulation in complex construction and with dynamic boundary conditions over long time periods (many years) has been developed with the commercial software Comsol. Comparison between this simplified model and CFD simulations demonstrates that the accuracy of the results is acceptable to the scope of the moisture risk prediction.

Evaluation criteria for internal insulation systems are implemented, employing numerical simulations and simplified analytical methods. Furthermore, complex construction details, such as timber beams embedded in external walls, are analyzed with respect to the moisture damage and the mold germination risk by means of 2D and 3D numerical simulations.

Numerical analysis shows that, under certain boundary conditions, 2D simulation can be considered as sufficiently accurate for evaluation of the moisture risk at the beam-wall junction. Future research including the effect of driving rain is required for a further generalization of the present results.

Bibliography

[1] (1999), ÖNORM EN 772-4 Methods of test for masonry units - Part 4: Determination of real and bulk density and of total and open porosity for natural stone masonry units.

[2] (2001), DIN 4108-3 Thermal protection and energy economy in buildings - Part 3 Protection against moisture subject to climate conditions - Requirements and directions for design and construction.

[3] (2001), ÖNORM EN 12664 Thermal performance of building materials and products - Determination of thermal resistance by means of guarded hot plate and heat flow meter methods -Dry and moist products of medium and low thermal resistance.

[4] (2002), ÖNORM EN ISO 12572 Hygrothermal performance of building materials and products - Determination of water vapour trasmission properties.

[5] (2013), ÖNORM EN ISO 12571 Hygrothermal performance of building materials and products - Determination of hygroscopic sorption properties.

[6] *Alduchov O.A.* and *Eskridge R.E.* (1995), Improved Magnus form approximation of saturation vapor pressure, *J. Appl. Meteor.*, **35**: pp. 601–609.

[7] *Baehr H.D.* (2005), *Thermodynamik: Grundlagen und technische Anwendungen*, Springer-Verlag.

[8] *Baehr H.D.* and *Stephan K.* (2008), *Wärme- und Stoffübertragung*, Springer-Verlag, 6. Auflage, Berlin.

[9] *Bednar T.* (2000), Beurteilung des feuchte- und wärmetechnischen Verhaltens von Bauteilen und Gebäuden, *Dissertation, Technischen Universität Wien.*

[10] *Bianchi Janetti M.*, *Ochs F.* and *Feist W.* (2013), Numerical Quality of a Model for Coupled Heat and Moisture Transport in COMSOL Multiphysics, *2nd Central European Symposium on Building Physics, Wien.*

[11] *Bianchi Janetti M.*, *Ochs F.* and *Feist W.* (2014), Assessment of the moisture risk in constructions including convection inside air cavities, *10th Nordic Symposium on Building Physics, Lund, Sweden.*

[12] *Bianchi Janetti M.*, *Ochs F.*, *Pfluger R.* and *Feist W.* (2012), Hygrothermische 3D Simulation von Bauteilen mit COMSOL Multiphysics, *BAUSIM Berlin*.

[13] *Bianchi Janetti M.*, *Pfluger R.* and *Ochs F.* (2014), Internal insulation applied to a listed school building : in situ measurements and numerical analysis, *18. Passivhaustagung, Aachen*.

[14] *Binder A.*, *Künzel H.* and *Zirkelbach D.* (2013), A new approach to measure liquid transport in capillary active interior insulation, *2nd Central European Symposium on Building Physics, Wien*.

[15] *Binder A.*, *Zirkelbach D.* and *Künzel H.* (2010), Test method to quantify wicking properties of porous insulation materials designed to prevent interstitial condensation, *AIP Conference Proceedings*, **1254**: pp. 242–247.

[16] *Celia M.*, *Bouloutas E.* and *Zarba R.* (1990), A general mass-conservative numerical solution for the unsaturated flow equation, *Water Resources Research*, **26**(7): pp. 1483–1496.

[17] *Chiba R.* and *Sugano Y.* (2011), Transient hygrothermoelastic analysis of layered plates with one-dimensional temperature and moisture variations through the thickness, *Composite Structures*, **93**(9): pp. 2260–2268.

[18] *Churchill S.W.* and *Chu H.S.* (1975), Correlating equations for laminar and turbulent free convection from a vertical plate, *International Journal of Heat and Mass Transfer*, **18**: pp. 1323–1329.

[19] *Corcione M.* (2008), Natural convection heat transfer above heated horizontal surfaces, *5th WSEAS International Conference on Heat and Mass transfer (HMT'08)*, pp. 206–211.

[20] *Cotton I.* (1978), Natural convection in enclosures, *Proceedings 6th international heat transfer conference, Toronto*, **6**: pp. 13–31.

[21] *De Freitas V.P.*, *Abrantes V.* and *Crausse P.* (1996), Moisture Migration in Building Walls - Analysis of the Interface Phenomena, *Building and Environment*, **31**(2): pp. 99–108.

[22] *Defraeye T.*, *Blocken B.* and *Carmeliet J.* (2011), Analysis of convective heat and mass transfer coefficients for convective drying of a porous flat plate by conjugate modelling, *International Journal of Heat and Mass Transfer*, **55**(1-3): pp. 112–124.

[23] *Duarte J.a.B.F.* and *Ribeiro J.W.* (1998), Generalised integral transform solutions of 3-D Luikov problems, *Transactions on Engineering Sciences, WIT Press, ISSN 1743-3533*, **20**.

[24] *Duarte J.a.B.F.*, *Ribeiro J.W.*, *Pinheiro P.R.* and *de Holenda C.A.M.* (2008), The effect of pressure in 2d Luikov drying problem, *International Conference*

on Computer Science, Information, and Systems Sciences, and Engineering, Bridgeport, **1**: pp. 1–10.

[25] *Fechner H.*, *Ruisinger U.*, *Nicolai A.* and *Grunewald J.* (2015), COND - A software for hygrothermal evaluation of building envelope systems. http://bauklimatik-dresden.de/cond/index.php.

[26] *Fechner H.*, *Ruisinger U.*, *Nicolai A.* and *Grunewald J.* (2015), Delphin. Simulation program for the calculation of coupled heat, moisture, air, pollutant, and salt transport. http://www.bauklimatik-dresden.de/delphin/index.php.

[27] *Feist W.* (1994), *Thermische Gebäudesimulation - Kritische Prüfung unterschiedlicher Modellansätze*, Verlag C.F. Müller.

[28] *Feist W.* (2005), Passivhauskomponenten und Innendämmung, *Protokollband Nr.32. Faktor 4 auch bei sensiblen Altbauten: Passivhauskomponeneten + Innendämmung. Darmstadt*, pp. 1–16.

[29] *Feist W.* (2015), Passive House Planning Package (PHPP). The energy balance and planning tool for efficient buildings and refurbishments. http://passivehouse.com/04_phpp/04_phpp.htm.

[30] *Feng C.*, *Meng Q.*, *Janssen H.* and *Feng Y.*, Effect of temperature on the sorption isotherm and vapor permeability, *2nd Central European Symposium on Building Physics, Wien*, pp. 71–76.

[31] *Gaur R.C.* and *Bansal N.K.* (1999), Periodic solution of Luikov equations for heat and mass transfer in capillary porous bodies, *International Journal of Energy Research*, pp. 875–885.

[32] *Gnoth S.*, *Jurk K.* and *Strangfeld P.* (2005), Hygrothermisches Verhalten eingebetteter Holzbalkenköpfe im innnengedämmten Außenmauerwerk. Heizungstechnisch gestützte Innendämmung bei Holzbalkendecken, *Bauphysik*, **27**: pp. 117–128.

[33] *Grunewald J.* (1997), *Diffusiver und konvektiver Stoff- und Energietransport in kapillarporösen Baustoffen*, PhD thesis, Technischen Universität Dresden.

[34] *Haupl P.* and *Fechner H.* (2003), Hygric Material Properties of Porous Building Materials, *Journal of Building Physics*, **26**(3): pp. 259–284.

[35] *Holm A.*, *Krus M.* and *Künzel H.* (2002), Approximation der Feuchtespeicherfunktion aus einfach bestimmbaren Kennwerten, *IBP-Mitteilung 406*, **29**: pp. 10–11.

[36] *Isaksson T.*, *Thelandersson S.*, *Ekstrand-tobin A.* and *Johansson P.* (2010), Critical conditions for onset of mould growth under varying climate conditions, *Building and Environment*, **45**(7): pp. 1712–1721.

[37] *James C., Simonson C.J., Talukdar P.* and *Roels S.* (2010), Numerical and experimental data set for benchmarking hygroscopic buffering models, *International Journal of Heat and Mass Transfer*, **53**(19-20): pp. 3638–3654.

[38] *Janssen H.* (2013), Simulation efficiency and accuracy of different moisture transfer potentials, *Journal of Building Performance Simulation*, **7**(5): pp. 379–389.

[39] *Janssen H., Blocken B.* and *Carmeliet J.* (2007), Conservative modelling of the moisture and heat transfer in building components under atmospheric excitation, *International Journal of Heat and Mass Transfer*, **50**(5-6): pp. 1128–1140.

[40] *Kehl D., Ruisinger U., Plagge R.* and *Grunewald J.* (2013), Wooden beam ends in masonry with interior insulation - A literature rewiew and simulation on causes and assessment of decay, *CESBP Wien*, pp. 299–304.

[41] *Krischer O.* (1963), *Die wissenschaftlichen Grundlagen der Trocknungstechnik*, Springer-Verlag, Berlin, Göttingen, Heidelberg.

[42] *Krus M.* (1995), Moisture Transport and Storage Coefficients of Porous Mineral Building Materials, *PhD, Lehrstuhl Konstruktive Bauphysik, Universität Stuttgart*.

[43] *Kulasiri D.* and *Woodhead I.* (2005), On modelling the drying of porous materials: analytical solutions to coupled partial differential equations governing heat and moisture transfer, *Mathematical Problems in Engineering*, (3): pp. 275–291.

[44] *Künzel H.* (1995), Simultaneous heat and moisture transport in building components, *Fraunhofer IRB Verlag Stuttgart (ISBN 3-8167-4103-7)*.

[45] *Liu J.* and *Cheng S.* (1991), Solutions of Luikov equations of heat and mass transfer in capillary-porous bodies, *International Journal of Heat and Mass Transfer*, **34**(7): pp. 1747–1754.

[46] *Lobo P.D.* (2002), On comparing finite difference schemas applied to a nonlinear multi-region heat and mass transfer problem, *Computational Mechanics*, **28**(1): pp. 55–62.

[47] *Luikov A.V.* (1966), *Heat and Mass Transfer in Capillary-Porous Bodies*, Pergamon Press, Oxford.

[48] *Mikhailov M.* and *Özisik M.N.* (1984), *Unified analysis and solutions of heat and mass diffusion*, Dover Publications, New York.

[49] *Nespoli L., Bianchi Janetti M.* and *Ochs F.* (2013), Comparing Different Approaches for Moisture Transfer inside Constructions with Air Gaps, *Comsol Conference Rotterdam*.

[50] *Ochs F.* (2009), Modelling Large-Scale Thermal Energy Stores, *PhD Thesis, Faculty of Energy and Process and Bio Technology, University of Stuttgart.*

[51] *Ochs F.* (2013), Combined determination of moisture and heat transport coefficients, *Forschungsbericht zum BMU-Vorhaben, Solarthermie2000plus, Institut für Thermodynamik und Wärmetechnik (ITW) Universität Stuttgart, 2013.*

[52] *Pandey R., Srivastava S.K.* and *Mikhailov M.D.* (1999), Solutions of Luikov equations of heat and masstransfer in capillary porous bodies through matrixcalculus: a new approach, *International Journal of Heat and Mass Transfer*, **42**(14): pp. 2649–2660.

[53] *Pandey R.N.* and *Pandey S.* (2000), Complete and satisfactory solutions of Luikov equations of heat and moisture transport in a spherical capillary porous body, *International Communications in Heat and Mass Transfer*, **27**(7): pp. 975–984.

[54] *Pel L.* and *Brocken H.* (1996), Determiination of moisture diffusivity in porous media using moisture concentration profiles, *Int. J. Heat Mass Transfer.*, **39**(6).

[55] *Peper S.r., Bangert A., Rupps W.* and *Bastian Z.* (2013), Messungen zur Andichtung von Holzbalkenköpfen und Luftdichtheit von OSB-Platten, *8. Internationales BUILDAIR-Symposium, Hannover, Germany.*

[56] *Pfluger R.* (2005), Lösungen für den Feuchteschutz, *Protokollband Nr.32. Faktor 4 auch bei sensiblen Altbauten: Passivhauskomponeneten + Innendämmung. Darmstadt*, pp. 49–83.

[57] *Philip J.* and *de Vries D.* (1957), Moisture movement in porous materials under temperature gradients, *Transactions, Amer. Geophysical Union*, **38**: pp. 222–232.

[58] *Qin M., Belarbi R.* and *Aït-mokhtar A.* (2006), Transfer Function Method to Calculate Simultaneous Heat and Moisture Transfer in Porous Building Materials, *Annex 41 MOIST-ENG, Working meeting, April 3-5, Kyoto, Japan.*

[59] *Quirouette R.* (2004), *Air Pressure and the Building Envelope*, Canada Mortgage and Housing Corporation.

[60] *Ramires M.L.V., Nieto de Castro C.A., Nagasaka Y., Nagashima A., Assael M.J.* and *Wakeham W.A.* (1995), Standard reference data for the thermal conductivity of water, *J. Phys. Chem. Ref. Data 24, 1377.*

[61] *Roels S., Carmelit J., Hens H., Adan O., Brocken H., Cerny R., Pavlik Z., Hall C., Kumaran K., Pel L.* and *Plagge R.* (2004), Interlaboratory Comparison of Hygric Properties of Porous Building Materials, *Journal of Thermal Envelope and Building Science.*

[62] *Samantray P.K., Karthikeyan P.* and *Reddy K.* (2006), Estimating effective thermal conductivity of two-phase materials, *International Journal of Heat and Mass Transfer*, **49**(21-22): pp. 4209–4219.

[63] *Scheffler G.A.* (2008), *Validation of hygrothermal material modelling under consideration of the hysteresis of moisture storage*, PhD thesis, Technischen Universität Dresden.

[64] *Schirmer R.* (1938), Die Diffusionswiderstandszahl von Wasserdampf-Luftgemischen und die Verdampfungsgeschwindigkeit, *VDI Beiheft Verfahrenstechnik*, **6**: pp. 170–177.

[65] *Sedlbauer K.* (2001), *Prediction of mould fungus formation on the surface of and inside building components*, PhD thesis, Frauenhofer Institute for Building Physics.

[66] *Skeel R.D.* and *Berzins M.* (1990), A method for the spatial discretization of parabolic equations in one space variable, *SIAM Journal on Scientific and Statistical Computing*, **11**: pp. 1–32.

[67] *Troi A.* and *Bastian Z.* (2014), *Energy Efficiency Solutions for Historic Buildings - A Handbook*, Birkhäuser Verlag.

[68] *Tsilingiris P.T.* (2008), Thermophysical and transport properties of humid air at temperature range between 0 and 100 ° C, *Energy Conversion and Management*, **49**: pp. 1098–1110.

[69] *Valentini B., Theiner Y., Aschaber M., Lehar H.* and *Hofstetter G.* (2013), Single-phase and multi-phase modeling of concrete structures, *Engineering Structures*, **47**: pp. 25–34.

[70] *Van Belleghem M.* (2013), *Modelling Coupled Heat and Moisture Transfer Between Air and Porous Materials for Building Applications*, PhD thesis, Universiteit Gent, Faculteit Ingenieurswetenschappen en Architectuur.

[71] *Van Belleghem M., Steeman H.j., Steeman M., Janssens A.* and *De Paepe M.* (2010), Sensitivity analysis of CFD coupled non-isothermal heat and moisture modelling, *Building and Environment*, **45**(11): pp. 2485–2496.

[72] *Van Belleghem M., Steeman M., Willockx a., Janssens a.* and *De Paepe M.* (2011), Benchmark experiments for moisture transfer modelling in air and porous materials, *Building and Environment*, **46**(4): pp. 884–898.

[73] *Van Schijndel A.* (2007), *Integrated heat air and moisture modeling and simulation*, PhD thesis, University of Technology Eindhoven.

[74] *Wang J., Carson J.K., North M.F.* and *Cleland D.J.* (2006), A new approach to modelling the effective thermal conductivity of heterogeneous materials, *International Journal of Heat and Mass Transfer*, **49**(17-18): pp. 3075–3083.

[75] *Whitaker S.* (1977), Simultaneous heat mass and momentum transfer in porous media: a theory of drying, *Advances in Heat Transfer*, pp. 119–203.

[76] *Wojcik R.* (2013), Anti damp preservation of internally insulated brick walls, *2nd Central European Symposium on Building Physics, Wien.*

[77] *Yovanovich M.M.* and *Jafarpur K.* (1993), Bounds on Laminar Natural Convection from Isothermal Disks and Finite Plates of Arbitrary Shape for all Orientations and Prandtl Numbers, *ASME Winter Annual Meeting, HTD-, New Orleans, Louisiana, Nov.28-Dec.3*, **Vol.264**: p. 93.